České vysoké učení technické v Praze
Fakulta jaderná a fyzikálně inženýrská

Doctoral thesis

Application of Microscopy Methods for Characterization of Silicon Nanostructures

Prague, 2022 Ing. Matěj Hývl

Bibliografický záznam

Autor	Ing. Matěj Hývl České vysoké učení technické v Praze Fakulta jaderná a fyzikálně inženýrská Katedra fyzikální elektroniky
Název práce	Aplikace mikroskopických metod pro charakterizaci křemíkových nanostruktur
Studijní program	Aplikace přírodních věd
Studijní obor	Fyzikální inženýrství
Školitel	RNDr. Antonín Fejfar, CSc. Fyzikální ústav Akademie věd ČR v.v.i. Na Slovance 1999/2 182 21 Praha 8
Školitel specialista	doc. Ing. Ivan Richter, Dr. České vysoké učení technické v Praze Fakulta jaderná a fyzikálně inženýrská Katedra fyzikální elektroniky V Holešovičkách 2 180 00 Praha 8
Akademický rok	2021-2022
počet stran	TBD
Klíčová slova	Mikroskopie atomárních sil, fotovoltaika, C-AFM tomografie

Bibliographic Entry

Author	Ing. Matěj Hývl Czech Technical University in Prague Faculty of Nuclear Sciences and Physical Engineering Department of Physical Electronics
Title of Dissertation	Application of Microscopy Methods for Characterization of Silicon Nanostructures
Degree Programme	Applications of Natural Sciences
Field of Study	Physical Engineering
Supervisor	RNDr. Antonín Fejfar, CSc. Institute of Physics Czech Academy of Sciences Na Slovance 1999/2 182 21 Praha 8
Supervisor specialist	doc. Ing. Ivan Richter, Dr. Department of Physical Electronics Faculty of Nuclear Sciences and Physical Engineering Czech Technical University in Prague V Holešovičkách 2 180 00 Praha 8
Academic Year	2021-2022
Number of Pages	TBD
Keywords	Atomic Force Microscopy, photovoltaics, C-AFM Tomography

Declaration

I hereby declare I have written this dissertation independently and quoted all the sources of information used in accordance with methodological instructions on ethical principles for writing an academic thesis. Moreover, I state that this thesis has neither been submitted nor accepted for any other degree.

In Prague, 2022

....
Ing. Matěj Hývl

Abstrakt

Sluneční energie je nejdostupnější zdroj energie na Zemi, který dokáže s přehledem pokrýt veškerou elektrickou spotřebu lidstva nyní i do budoucna. Proto řada vědců pracuje již od devatenáctého století na vývoji slunečních článků určených k jejímu využití. Pokrok v oblasti nanostrukturovaných slunečních článků, ke kterému došlo v posledních desítkách let, s sebou rovněž přinesl potřebu rozvíjet techniky, které dovedou články charakterizovat na potřebné nanometrové škále. Mezi takové techniky patří právě skenovací sondová mikroskopie (SPM), která je pro charakterizaci řady vlastností slunečních článků velmi vhodná. Tato práce pojednává o proud-detekující mikroskopii atomárních sil, rozsáhlé, ale relativně mladé skupině technik SPM, které využívají vodivý hrot k měření lokálních elektrických vlastností. Ačkoli jsou výsledky těchto technik velmi slibné, neexistuje dosud univerzálně uznávaný teoretický model, který by popisoval řadu klíčových principů, na kterých jsou založené. Proto při interpetaci jejich výsledků často dochází k chybám, některá měření je také velmi obtížné zopakovat i v rámci jedné laboratoře. Cílem této práce je předložit výsledky experimentů zkoumajících povahu elektrického kontaktu mezi hrotem a vzorkem během měření, jeho odpor i změny tohoto odporu způsobené vlivem topografie vzorku. Chceme rovněž nabídnout několik rad, jak se při aplikaci proud-detekujícího AFM na solární články vyhnout těmto i jiným vrozeným vadám těchto technik. V neposlední řadě práce demonstruje použití dvou nových měřicích technik, Skalpelového C-AFM a C-AFM tomografie, na křemíkových slunečních článcích. V rámci jejich popisu předkládáme potřebné informace pro nastavení mikroskopu, seznam problémů, na které je dobré se během měření soustředit i konkrétní ukázku interpretace naměřených dat, která byla nedávno publikována v prestižním vědeckém časopise.

Abstract

Solar energy is the most accessible source of energy on Earth, far more then capable to cover the whole demand of the humankind in presence and in future. To harvest this immense source of power, solar cells are being developed since the 19th century by scientists all over the world. With the rise of nanostructured solar cells came the need for nano-characterisation of photovoltaic properties and the best candidate to fill this need is, in many cases, scanning probe microscopy (SPM). This thesis specifically concentrates on the current-detecting atomic force microscopy. This rather large group of relatively young SPM techniques using conductive tip to map local electrical properties is extremely promising in nanostructured solar cells research. However, to this day there is no universally accepted theoretical model of its basic working principles. Therefore, the interpretations of the results obtained by these techniques are often questionable. In some cases, measurements are difficult to repeat even with the same setup. In this work, we present our findings and thoughts regarding the tip-sample contact resistance and its changes caused by sample topography as well as practical demonstration on how to out-smart these and other inherently present shortcomings of current-detecting AFM in regard to solar-cell characterization. We also offer a detailed description of the application of two new techniques, Scalpel C-AFM and C-AFM Tomography, on the silicon solar cell sample, starting from the set-up of the measurement with practical list of do's and don'ts' all the way to the interpretation of a particular result, recently published in a prestigious scientific journal.

I would like to dedicate this dissertation to my family, Míša and Václav, in hope it will be at least a small satisfaction for them for all those hours I couldn't be with them while working on it.

Acknowledgements

This work has been long in making, and I would like to thank everyone who helped me get there, eventually. First and foremost, Antonín Fejfar, for taking me under his wing and showing me a way into the world of atomic force microscopy and science in general. I also want to thank my two closest colleagues and, for all practical purposes, supervisors-specialists, Aleks Vetuško for teaching me more than I could learn about AFM and Martin Ledinský for everything else, from consultations and advice to always making sure I had some interesting samples to play with on the microscope and conferences to show my results at. All of the research carried out at FZU was supported by the CzechNanoLab Research Infrastructure. I would also like to thank to our international collaborators for all the work done outside of the institute. Namely to Markus Kratzer and Christian Teichert (for the generous access to their lab at the Montanuniversität in Leoben with an excellent home-built KPFM setup), Pere Roca i Cabarocas and Martin Foldyna (for many samples of Si radial junction nanorods as well as for the opportunity to spent several weeks at LPICM laboratories at Ecole Polytechnique in Paris-Saclay with their RESISCOPE AFM) and Gizem Nogay and her groups at EPFL and CSEM for supplying me with selective-contact samples and an immense help on my latest paper. My thanks also belong to doc. Ing. Ivan Richter, Dr., who always did everything in his power to help me with the formal side of my studies, and to Bc. Radka Mika Havlíková, who might actually deserve bigger credit for me reaching this point of my studies than I do. I am also extremely grateful to the rest of my colleagues, Martin Müller, Martin Hladík, Tomáš Mates, Zdeňka Hájková, Aleš Vlk, Pavla Bauerová, Jiří Červenka and Martin Šilhavík, for fruitful (and sometimes less so) discussions and all the help along the way. Last but not least, I would like to express my undying gratitude to my friends, namely Jiří Slabý, Václav Procházka, Jakub Klečka, Jan Mrkos and others, for constantly asking me for the last seven and a half years whether my thesis is done, and to my parents for (almost) not doing so.

Well, it is now.

List of Figures

1.1 *Basic parameters describing the solar cell efficiency* 4

1.2 *Brief schematics of the radial junction nanorod growth* 6

1.3 *Radial junction solar cells under SEM* 7

1.4 *TOPCon Solar Cell* 8

1.5 *Schematics of the current-detecting AFM setup* 12

2.1 *Tip-sample contact* 20

2.2 *Impact of the sample geometry on C-AFM* 22

2.3 *Model of tip-sample contact influenced by sample geometry* 24

2.4 *Resistance behaviour during force ramp on Ge* 25

2.5 *Force-Resistance Measurement* 26

2.6 *Qualitative current mapping on Si NW RJs* 30

2.7 *Model circuit of C-AFM on Si NW RJs* 32

2.8 *Photoconductive AFM on Si NW RJs* 34

2.9 *Measuring the inner junction quality* 36

2.10 *Correlation of C-AFM and SEM* 37

2.11 *Inner architecture of the minimodule* 39

2.12 *RESISCOPE C-AFM maps of current on bare P1 scribe* 40

2.13 *RESISCOPE C-AFM maps of P1 scribe before the top contact deposition* . 41

3.1 *Standart C-AFM on selective contacts* 48

3.2 *Switching between (a) low-force and (c) high-force C-AFM regimes.* 49

3.3 *Scalpel C-AFM - effect of the annealing temperature* 49

3.4 *HRTEM and Raman - sample crystallinity* 50

3.5 *Scalpel C-AFM - role of the oxide layer* 52

3.6 *C-AFM Tomography of the selective contact* 53

3.7 *Scalpel C-AFM slices for tomography* 53

4.1 *Scalpel C-AFM - Switching between sliding and ploughing regime* 61

4.2 *Scalpel C-AFM - removal rate, current signal change* 62

4.3 *Scalpel C-AFM - Typical diagonal feature after* 64

4.4 *Scalpel C-AFM - re-deposition of teh material* 64

4.5 *Scalpel C-AFM - example of gradual decrease of the scan size* 65

4.6 *Example of C-AFM Tomography* 66

List of Acronyms

a-Si	amorphous silicon
AFM	atomic force microscopy
AZO	aluminium zinc oxide
C-AFM	conductive atomic force microscopy
c-Si	crystalline silicon
CIGS	copper indium gallium selenide solar cells
EBIC	electron-beam induced current
EFM	electric force microscopy
EQE	external quantum efficiency
FTO	fluorine-tin oxide
HRTEM	high-resolution transmission electron microscopy
IR	infrared
ITO	indium-tin oxide
KPFM	Kelvin probe force microscopy
mono-Si	mono-crystalline silicon
NSOM	near-field scanning optical microscopy
pC-AFM	photoconductive atomic force microscopy
PEVCD	plasma-enhanced chemical vapour deposition
poly-Si	poly-crystalline silicon
RJ	radial junctions
SCM	scanning capacitance microscopy
SEM	scanning electron microscopy
SHJ	Silicon hetero-junction
Si NW	silicon nanowire
SiC_x	silicon carbide
SiO_x	silicon oxide
SPM	scanning probe microscopy
SSRM	scanning spreading resistance microscopy

STM	scanning tunnelling microscopy
TCO	transparent conductive oxide
TOPCon	Tunnel Oxide Passivated Contact
VLS	vapor-liquid-solid

Contents

Bibliographic Entry iii

Abstract ix

Acknowledgements xiii

List of Figures xv

List of Acronyms xvii

1 Introduction 1

1.1 Brief Introduction to Solar Cells 3

1.2 Thin-film Solar Cells 5

1.2.1 Silicon Nanowire-based Radial Junctions 6

1.2.2 High Thermal Budget c-Si Solar Cells with Oxide and poly-Si Contact 7

1.3 Characterisation of Nanostructured Solar Cells 9

1.3.1 Atomic Force Microscopy for Solar Cell Characterisation 10

1.3.2 Current-Detecting Atomic Force Microscopy 11

2 Current-detecting Techniques for Solar Cell Research - a Closer Look 17

AFM Probes for Current Detection 18

2.1 Shortcomings of the Current-detecting Techniques 19

2.1.1 Tip-Sample Contact Resistance 20

2.1.2 Sample Current Generation 32

2.2 Connecting Microscopical Properties to Macroscopic Parameters 33

2.3 Further Applications of AFM on Solar Module Architecture Level 38

3 C-AFM Tomography Case Study 43

3.1 Introduction 44

3.2 Experimental Section 46

3.3 Results and Discussion 48

3.4 Conclusions 55

4 C-AFM Tomography - Lessons Learned 57

4.1 Setpoint vs Contact Force 58

4.1.1 Spring constant inconsistences 58

4.1.2 Setpoint drift 59

4.2 Material removal rate 60

4.3 Single-pass vs Two-pass configuration 61

4.4 What's important to do before the scalpel C-AFM measurement: 63

5 Conclusions and Outlook **67**

List of relevant publications 69

Bibliography **73**

Chapter 1

Introduction

Ever since the press conference held in 1954 in Bell Laboratories announcing the creation of the new type of silicon solar cell with permanent p-n junction, science has been pushing the limits of the new-found technology with incredible speed. Besides fulfilling nowadays non-disputable need of humankind for non-depletable and ecologically responsible energy source, photovoltaic energy offers limitless possibilities of creating a decentralized, mobile and flexible power grid, given the existence of the satisfactory energy-storage solution. In fact, full embracement of the photovoltaic energy could bring and support big changes to the social order [1], given the relatively low price for the solar panel production, installation and operation [2].

Over the years, photovoltaic devices grew in many directions from the original silicon p-n junction solar cell. Countless scientists, engineers and entrepreneurs have invested a great deal of time and resources into developing solar panels based on both organic and inorganic materials, with bulk, thin film, and nanostructured geometry, with or without concentrators and so on. Every year there is a new competitor in the race for the best solar cell and every year many concepts, companies and ideas drop out of the competition, unable to keep the pace with the global research. While mono-crystalline silicon (mono-Si) and poly-crystalline silicon (poly-Si) solar cells dominate the commercial market these days, other technologies are proving their worth in special applications or wait for their opportunity to turn their potential into success.

The ever-growing efficiency of the solar cells based on various materials and their combinations is enabled by the systematic effort for complex in-depth characterisations of not only the active zone of the solar cell, but also all other aspects of the fully constructed

solar panel. This characterisation utilizing countless scientific methods is undertaken in laboratories all over the world, ranging from complex analysis of the mechanical stress in installed solar panel arrays to meticulous description of the quantum behaviour of photons and electrons in photovoltaic devices.

To assist this effort, I have set the following goals for my dissertation thesis:

- *To demonstrate the viability of existing scanning probe microscopy (SPM) techniques for solar cells characterization*
- *To increase traceability, repeatability and reproducibility of electrical SPM techniques*
- *To develop a new solar cell characterization methods based on SPM techniques*

1.1 Brief Introduction to Solar Cells

Solar cell is, simply put, a photodiode that generates electric current when it is exposed to the photon stream, a sunlight. Whatever the materials used in the solar cell, they have to fulfil two simple functions: Generate the electron-hole pair upon illumination and subsequently separate and collect both of the charge carriers. In the theoretical example of primitive silicon solar cell, electron-hole pairs are generated in the PN junction, separated by the its inner electric field and collected via electrical contacts on opposite sides of the junction. Whatever the materials and geometry used in the specific solar cell, we distinguish several key parameters that help us to compare the quality of the said solar cell. In general, the conversion efficiency is the most practical parameter describing the solar cell quality – it is defined as the ratio between the energy received from the sun ($\mathbf{P}_{in}$) and the energy generated by solar cell or so-called **peak power** $\mathbf{P}_{max}$. Peak power of a solar cell depends on many factors and it can be expressed by several equally important parameters: **short circuit current** $\mathbf{I}_{SC}$, **open circuit voltage** $\mathbf{V}_{OC}$ and the **fill factor FF**:

$$\eta = \frac{P_{max}}{P_{in}} = \frac{V_{OC} I_{SC} FF}{P_{in}} \tag{1.1}$$

Figure 1.1 can help us gain a clearer picture of what these parameters mean. It depicts an I/V characteristics of the circuit involving an ideal solar cell under illumination (i.e. when generating electric current) and a resistivity **R**. From this picture, we can derive that I_{SC} describes a current flowing through the circuit, when the electrodes of the solar cell are short circuited, i.e. the voltage is 0. Open circuit voltage is the maximum voltage solar cell can deliver. At this voltage, no current is flowing through the circuit. Peak power is the maximum power obtainable from the solar cell and fill factor is the ratio of the maximum power from the solar cell and the product of I_{SC} and V_{OC} [3]. In the Figure 1.1, black dashed line represents the power output of the solar cell at the given voltage. P_{max} is achieved when the solar cell is operated at so called maximum power point ($_{\sim}I_{MPP}$, V_{MPP}).

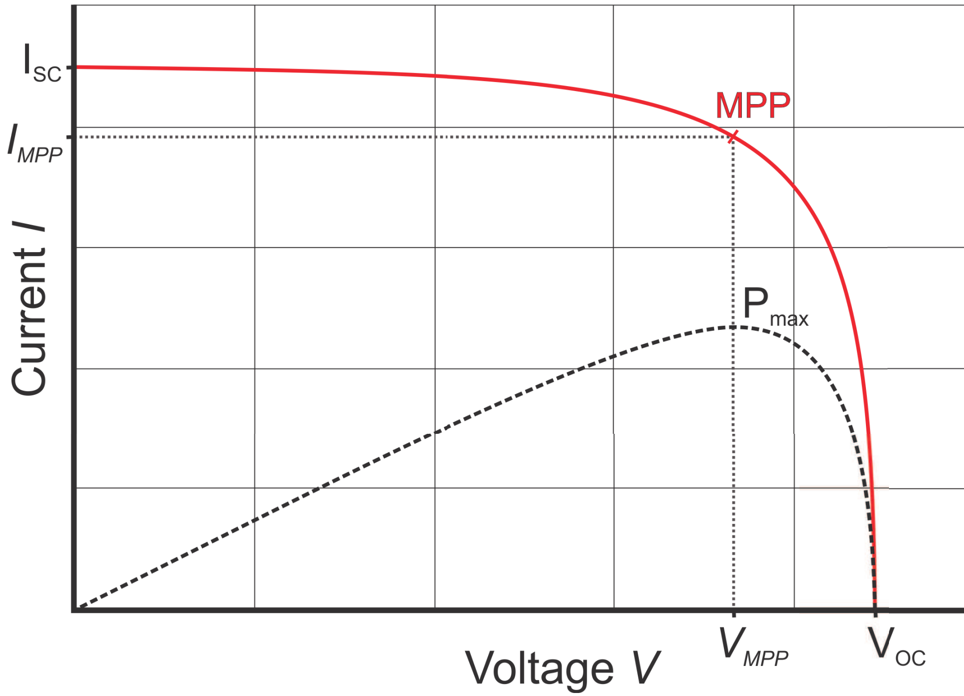

Figure 1.1: *Basic parameters describing the solar cell efficiency.*

For further characterization of the solar cell, external quantum efficiency (EQE) can also be usefull. It depends on the solar cell ability to capture the incident photons and generate electron-hole pairs from them (and is therefore, among others, wavelength-dependent). It also reflects the ability to extract and collect these pairs from the point of generation.

1.2 Thin-film Solar Cells

As previously mentioned, crystalline silicon (c-Si) solar cells dominate the solar energy generation markets. In the past, the biggest limiting factor in prices of such devices was the cost (monetary and energetic alike) associated with the production of c-Si wafers. This stimulated a massive effort to replace these then-expensive materials with cheaper and easier-to-use alternatives, thus creating the idea on thin-film solar cell. In thin-film solar cells, photogeneration takes place in the thin layer of material deposited on the substrate [4]. In case of silicon, decreasing the thickness of the solar cell unfortunately leads to the loss of the optical absorption. This translates directly into lower achievable efficiency, when compared to the c-Si "bulk" solar cells. To offset this inevitable deficiency, many strategies were established – utilizing low-cost production technologies, cheap substrates or nanostructured layers designated to introduce and maximize so-called light-trapping. Another option is to switch to completely different material from silicon. Although we mostly deal with Si-based technology, other non-silicon thin film solar cells are actually very promising. Among other materials, cadmium telluride (CdTe) [5], copper indium gallium selenide solar cells (CIGS)[6], [7], III-V semiconductors [8], [9] or organic-halide perovskites [10] are showing ever-increasing efficiency records while keeping the advantages of the thin-film arrangement.

Regardless the current dominant position of the Si-wafer cells on the market, some of the thin-film solar cell properties make them irreplaceable in certain specific applications, such as transparent solar cells (as a non-obtrusive layer usable for windows [11], [12]), flexible photovoltaics (military or space use [13], [14]) or so-called smart applications (Internet of things, smart textile etc. [15], [16]). Thin films are also being employed as a supporting technology for many state-of-the-art solar cells, be it as an absorber of an other-wise unutilised part of the solar spectra in tandem solar cells or an additional utility layer, e.g. for passivation of the bulk Si wafer as we will discuss later.

In the rest of this subchapter, we will introduce two different samples based on thin-film technologies. The first one is a prominent case of advanced nanostructuring of the thin-film silicon solar cell: Radial junctions (RJ) Si Solar cells based on silicon nanowires (Si NWs) offer interesting strategy of increasing optical absorption by orienting the thin film junction parallelly to the illumination on the randomly grown scaffolding on Si NWs.

Second example is a state-of-the-art Si-wafer-based solar cell building upon the Tunnel Oxide Passivated Contact (TOPCon) technology. This multi-layered solar cell

contains thin-film technology in the form of chemically grown silicon oxide (SiO_x) layer used for wafer passivation – passivating doped wafers is crucial for increasing V_{OC} of the resulting solar cell and parameters, defects and properties of this SiO_x layer can drastically affect its final efficiency.

1.2.1 Silicon Nanowire-based Radial Junctions

As a model sample in order to prove the viability of current-detecting techniques for solar cell characterization we chose the silicon radial junction solar cells based on silicon nanowires (Si NW RJs). Although the complexity of the sample causes occasional problems, it also possesses unique properties that allow for interesting result interpretation. Their topographical arrangement makes it possible to contact a single RJ nanorod at a time and to measure the local current or current-voltage characteristics.

Radial junction solar cells are based on Si NWs created by so called vapor-liquid-solid (VLS) growth process assisted by plasma-enhanced chemical vapour deposition (PEVCD). To seed the Si NWs, post-transition metal (Sn, In, Pb) nanoparticles are used as catalysts. Technical details of this process has been described elsewhere [17], [18] and are not crucial for our findings. Here, we will limit ourselves to brief description of the NW growth and inner structure of the resulting RJ nanorod.

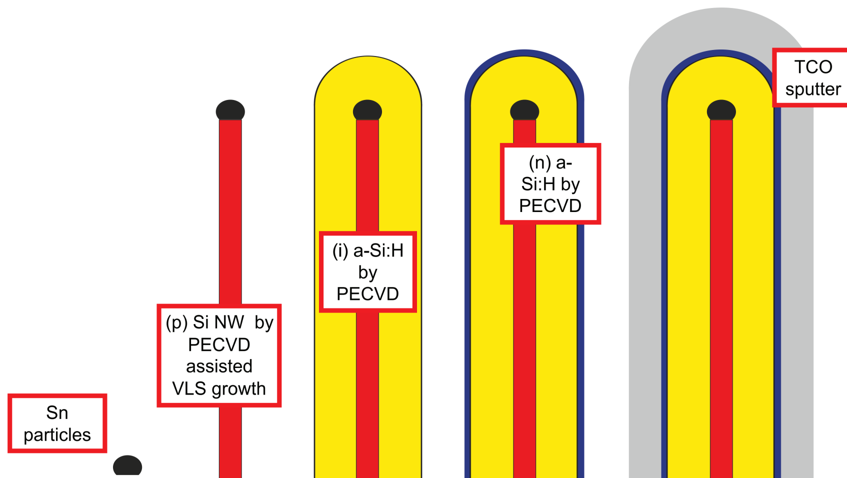

Figure 1.2: *Brief schematics of the radial junction nanorod growth.*

Figure 1.2 depicts individual steps necessary for the RJ nanorod creation. In case of our samples, the metal used for NW catalysis is tin (Sn). Using the plasma assisted VLS growth process, Si NW is created on the conductive substrate (e.g. aluminium zinc oxide (AZO)). This NW serves as a first part of the final junction. In Figure 1.2,

NW is p-doped, thus representing the P layer of the junction. Subsequently, amorphous undoped intrinsic layer is grown, a technological step common for the thin-film amorphous silicon (a-Si) solar cells. Intrinsic layer acts as a drift zone to improve carrier collection, offsetting the decreased charge-carrier mobilities in a-Si. PIN junction is finished by depositing a thinner n-doped silicon layer. In order to ensure proper carrier collection, nanorods are covered by thick layer of transparent conductive oxide (TCO), serving as one final electrode. Depending on the intended applications, other geometries are possible with either (or both) electrodes being transparent. Finished RJ solar cell (barring only the TCO electrode, that was missing for all our conductive atomic force microscopy (C-AFM) measurements) comprising of millions of unorganized nanorods, measured by the scanning electron microscopy (SEM), is shown in the Figure 1.3.

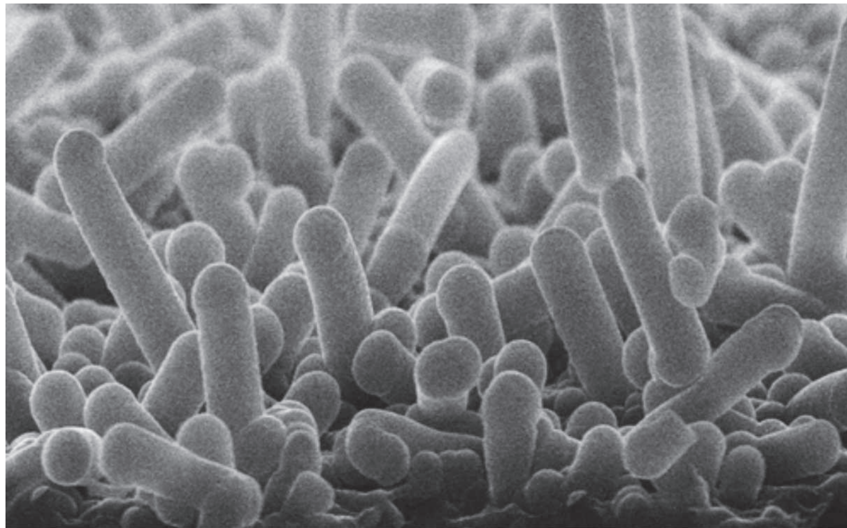

Figure 1.3: *Unfinished (still missing the top TCO electrode) RJ solar cells depicted by SEM.*

Further details regarding the growth and macroscopic photovoltaic properties of Si NW-based RJ solar cells of various kinds can be found in the comprehensive doctoral thesis of my colleague Martin Müller [18].

1.2.2 High Thermal Budget c-Si Solar Cells with Oxide and poly-Si Contact

The main limitation of the current industrial solar cells constitutes of the metal/absorber interface on the rear-contact, that often causes excessive losses of charge carriers caused by their recombination on the interface defects. While some technologies strive to reduce the metal contact area by various contact patterning, another option is to

implement so-called passivating contact instead. In this case, a layer stack system is placed between the c-Si wafer and the metal electrode. This stack fulfills two roles: it suppresses the charge-carrier recombination by passivating the defect states at the c-Si surface while also selectively blocking one type of the charge carriers.

While there are several approaches that fit the assignment, our interest lies in the so-called TOPCon solar cell. This technology uses high thermal budged process, that will be described in detail in Chapter 3. To give a rough idea, following description and illustration are taken from [19]:

The TOPCon structure consists of a chemically or photo-chemically grown ultra-thin - 1.2 to 1.6 nm - SiO_x buffer layer together with an approximately 20-nm-thick in-situ doped layer of a-Si. After deposition of the doped a-Si layer by PEVCD, the contact is annealed at temperatures in the range of 800 to 900°C and subsequently re-hydrogenated with atomic hydrogen generated by remote plasma in the temperature range of 400-450°C where atomic hydrogen can readily diffuse into c-Si. Combining this contact structure with a standard boron-diffused homojunction (homojunction = a junction fabricated by doping different elements into the same material, in this case c-Si) *at the front side, as illustrated in Figure 1.4, a world-record efficiency of* 25, 8% *for n-type both-sides-contacted c-Si solar cell was established.*

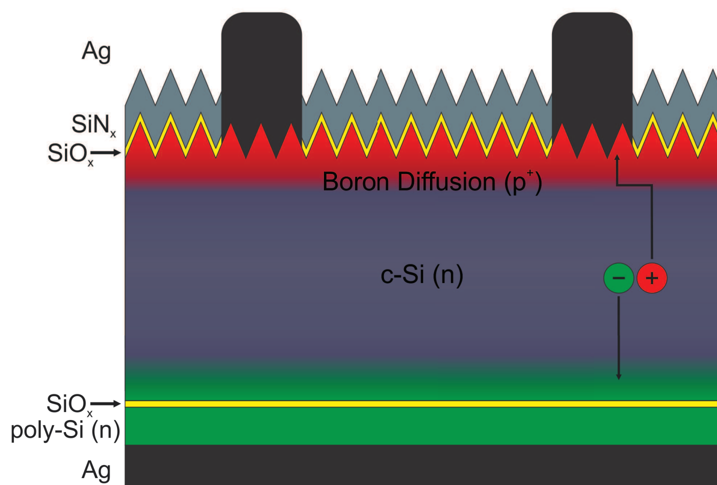

Figure 1.4: *Schematic cross-sectional view of the cells with a tunnel oxide passivating electron contact at the rear and a boron-diffused homojunction at the front.*

1.3 Characterisation of Nanostructured Solar Cells

Standard run-of-the-mill solar cell characterisation usually involves finding the macroscopic qualities and values - what is the over-all efficiency of the formed solar cell? What is its open circuit voltage or short-circuit current? What is its fill factor? It can also concern specific values related to the performance – what is the resistance of a certain individual component? With the rise of the new nanostructured solar cells [20]–[23], however, this information represents only averaged properties over huge amount of nanoscopic photovoltaic devices. While this still provides very useful information about the cell array, it cannot be used to study the properties of individual solar cells. For this, one would have to apply techniques with much finer resolution.

When characterizing solar cell on the nanoscale, i.e. on the scale of the quantum photo-effect itself, we often run into a problem with relating the measured characteristics to the macroscopic properties. How does the current detected on top of the solar cell or the surface potential of the material relate to its efficiency? Although there were some ventures undertaken in this direction [24]–[29], the universal relation between the two domains, microscopic and macroscopic properties, is still missing, as we will discuss later. While it might seem attractive to relate locally detected current to the short circuit current of the solar cell or somehow look for the connection between the surface potential and open circuit voltage of the sample, in most of the applications we limit ourselves to talking about local resistivities, dopant concentrations etc.

Among microscopic methods used to characterize solar cells and materials, SPM and namely Atomic force microscopy (AFM) stands out for its flexibility and uniquely wide range of possible applications. This relatively young [30] family of characterisation techniques is based on nanometer-sharp probe scanning over the sample in extremely close vicinity above the measured sample. Measurement itself is facilitated by the atomic-force interaction between the probe tip and the sample (hence the name of the technique). Depending on the used equipment and the ingenuity of the experimenter, this setup allows to map not only sample topography, but a vast range of other properties, on the scale limited only by the physical dimensions of the probing tip. Not only that, but it can do all of that without posing any major conditions on the sample properties, which differentiate it from the older Scanning tunnelling microscopy (STM) for example (which requires the measured sample to be conductive).

1.3.1 Atomic Force Microscopy for Solar Cell Characterisation

Applications of the AFM in the solar cells research start with the simplest of the AFM techniques – ***topography measurement*** [31]–[35]. Topography of the nanostructured solar cell in itself can reveal certain information about the solar cell inner workings. Active layer of the solar cell can consist of the material like CIGS or organic-halide perovskite, and it might be worth investigation the crystalline nature of such an active layer. Size of the crystalline grains, the film uniformity and thickness – all of these parameters will influence the solar cell over-all performance. Apart from that, AFM is also irreplaceable in manufacturing process of the nanostructured solar cells, offering a valuable feedback on dimensions of the crucial nanoscopic features for example.

More advanced AFM modes offer more detailed characterization of the solar cell. In the following chapters, we will delve deeply into the current-detecting AFM, but there are other applications of ever-growing number of the scanning probe microscopy techniques in the field of photovoltaics. We will start our incomplete list of the electrical AFM techniques applicable in solar-cell research with the non-current-detecting techniques in no particular order. Much more comprehensive and exhaustive lists have been compiled in the past by other authors [36], [37] and therefore we do not feel the need to try for an all-inclusive list. We will rather focus on techniques that author have personal experience with or find them interesting.

Electric force microscopy (EFM)

EFM is a good starting point when talking about electrical AFM. It is enabled by two-pass tapping mode: in the first pass through the line the microscope measures sample topography, then it scans the same line again in so-called second pass while keeping constant distance from the surface. During the second pass, microscope detects slight changes in the tip oscillation frequency caused by the localized surface charges on the sample. As such, it has been used on the wide spectra of solar-cell related materials in order to map the charge transport or distribution [38].

Kelvin probe force microscopy (KPFM)

KPFM allows user to compare the work function of the sample with the known work-function of the tip, effectively measuring the surface potential of the material with a resolution only slightly worst then the standard AFM – tens or hundreds of nanometres. It is by all means very similar to EFM and while many variations exist, the most common

version uses two-pass technique as well. In the second pass, changes in the cantilever oscillations are caused by the local surface potential differences. It has been widely used for the solar cell research [39]–[43]. Difficulties with performing and especially interpreting this technique could fill the whole thesis of itself.

Scanning capacitance microscopy (SCM)

SCM is another AFM-based technique applicable to solar cell research. During a measurement in contact mode with the grounded metallic tip, SCM measures a capacitance variation (C) caused by a voltage modulation (V) and obtains dC/dV [44]. Since changes in the capacitance, detected via the capacitance sensor consisting of oscillator, resonator and detector, are directly connected to local charge carrier concentration, this technique is utilized in nanoelectronics and solar cell research to map the dopant concentration etc [45]–[50].

1.3.2 Current-Detecting Atomic Force Microscopy

While EFM and SCM open wide possibilities for solar cell characterisation, a lion's share of the electrical AFM characterisation results is generated by **current-detecting techniques**. Similar to STM, key to this family of techniques is detecting the current flowing between the tip and the sample while modulating other parameters like tip-sample bias, measurement contact force, sample thickness etc. Current-based measurements are enabled by using conductive tips and very sensitive current amplifiers. While the expanding family of current-detecting techniques utilize a variety of different approaches, they all have their roots in a technique devised in 1993 [51] to measure the thickness of the thin silicon oxide layers via mapping the voltage bias necessary to detect constant current while scanning over a thin SiO_x sample. As the name suggest, the common feature of these techniques is detecting current with the scanning probe microscope, to whichever end the AFM operator finds fit at the moment. Mounting a conductive probe to the AFM equipped with a dedicated current pre-amplifier and electrically contacting the sample allows us to close an electric circuit every time the tip contacts the sample during the measurement cycle (nowadays this also includes semi-contact methods like PeakForce TUNA [52] etc. on top of the standard contact mode measurement dominant in the past).

With this modification of the classical AFM setup, depicted in Figure 1.5, one can detect currents flowing through such circuit with the precision up to picoampers (given

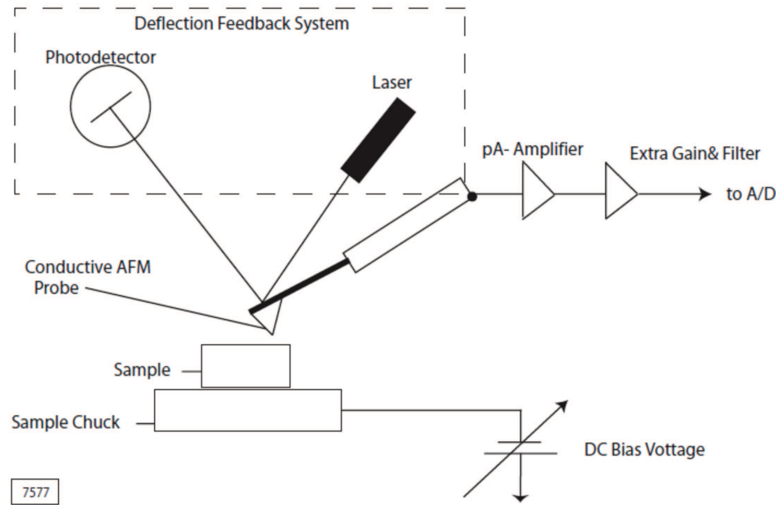

Figure 1.5: *Schematics of the current-detecting AFM setup, taken from official Bruker ICON manual.*

the sufficient technical equipment). Differing from technique to technique, current can be generated by the illumination [53], [54], surface charge displacement [55] or AC or DC voltage applied to the tip or the sample. Detected current signal is then less or more accurately converted into desired quantity, such as local thickness, dopant profile, local resistivity or local conductivity. In the following text, we will describe some of the relevant current-detecting techniques, including perhaps the most relevant of them, the C-AFM. While we will only briefly introduce most of the techniques here, we will further elaborate on some of them in the following chapters. We will also briefly touch on the AFM probes suitable for specific relevant applications and further elaborate on the shortcomings of the current detection with AFM. We will also practically demonstrate how these shortcomings can be overcome or at least mitigated in order to use the standard low-force C-AFM in the solar cell research.

Tunneling AFM

Tunnelling AFM is a direct ancestor of any other current-detecting technique. While STM only allows to measure conductive samples by adjusting the tip-sample distance to maintain constant tunnelling current (or vica versa), Tunnelling AFM can characterize less conductive samples in room-condition while mostly keeping the rigorous theory background largely unavailable to other current-detecting techniques. Unlike STM, current and position of the tip are monitored by separate systems. Supported by the excessive modelling of the mechanical and electrical contact between the tip and the sample [56]

and the possible tunnelling mechanisms, this technique strives to accurately measure the local thickness of isolating oxide thin films between the tip and a conductive electrode by performing and analysing local IV spectra. We are mostly mentioning this technique for its historical impact on the development of the electrical SPM as a whole, since its applications in the solar cell field are very limited. Since most of the theoretical models used for Tunneling AFM are limited to a very thin layers and otherwise very controlled environment, it is difficult to comfortably fulfill these conditions for the other current-detecting AFM techniques.

I-V Spectroscopy

Next step from the tunnelling AFM, the tip is not scanned in this case and remains (theoretically) positioned in one spot while the sample's response to applied bias in form of electric current is detected. While the instrumentation does not significantly differ from the previously described technique, the main difference is in its applications – measured samples are usually less defined than thin oxide layers and the detected current therefore cannot be described as "tunnelling". I-V spectroscopy shares many shortcomings with C-AFM (minus all problems coming from the dynamically moving tip) but is also widely used to characterize properties of solar cells and photovoltaic materials.

Scanning Conductive AFM (C-AFM)

C-AFM is in many ways a typical scanning current-detecting technique. During the measurement, voltage bias is applied between the tip and the sample and the resulting current flowing through the tip is detected. C-AFM is traditionally performed in contact mode, allowing for more stable electrical contact and longer time for current integration. Lately the semi-contact C-AFM have been enabled by high-speed controllers and possibility of high-precision coordination of the contact and current-detection time in force-modulation modes. From detected current one can not only try to determine the local sample conductivity, as the name suggests, but it is also possible (and sometimes more correct) to study charge carrier transport [57]–[59], shunts and leakage currents [60], [61] or even transport properties of the grain boundaries [62]. In contrast to scanning spreading resistance microscopy (SSRM)(see below), this technique will be sometimes referred to as low-force C-AFM, due to the relatively low contact forces applied during the measurement. In this work, we will demonstrate several direct applications of C-AFM on solar cells and photovoltaic materials and nanostructures.

Photoconductive AFM

Identical with standard C-AFM in almost every way, Photoconductive atomic force microscopy (pC-AFM) utilizes the ability of certain samples (like solar cells) to generate currents under illumination. The biggest difference for this technique is therefore the origin of the detected current – in its purest theoretical form no voltage bias is applied between the tip and the sample during the scan, charge carriers are only generated via the incident light. Based on the light qualities, we can study different properties of the measured sample [25], [54], [63], [64]. Depending on the experiment setup, sample can be illuminated globally [54] or locally using the hollow near-field scanning optical microscopy (NSOM) [25] probe for example. For photovoltaic applications, solar simulator is sometimes used as a light source. Other possibilities include different wavelengths of the source to study spectral response of the material [64] or simple white-light source for less sophisticated experiments. Red laser, usually used in the AFM photodiodes and optical levers, has to be considered when interpreting the results of this technique. To this end, microscope heads with near-IR laser are sometimes preferred for the pC-AFM on the silicon samples, as well as nose-type cantilevers, that allow more precise positioning of the light source in relation to the measured spot.

Scanning Spreading Resistance Microscopy (SSRM)

SSRM is historically one of the most successful and respected current-detecting techniques. It has been devised and further developed by De Wolf in IMEC in 1998 [65], [66] and has been relatively widely used since to map the dopant profiles in solar-cell cross-sections [39], [67] as well as other applications [68]. While the geometry of the experiment is practically identical to standard C-AFM, much higher contact forces are applied, making the tip-sample contact very stable and significantly reducing the tip-sample resistance. While this puts extra demands on the lab equipment, it allows for reliable and repeatable detection of local currents. With the before-mentioned reduction of the tip-sample contact, this technique allows for arguably accurate mapping of the local spreading resistance of the measured sample. This measured resistance is often coupled with the calibration on the dopant-concentration steps sample to quantitatively asses the dopant concentration in the nanostructured cross-sections of solar cells or nanoelectronics devices.

With quick development and success of the AFM in solar cell characterisation came also large increase in number of AFM operators. However, the fast pace of the photovoltaic research does not always allow to gain sufficient experience with the more-complex

techniques such as electrical AFM. Moreover, the ever-present pressure for the unique results can lead to an over-ambitious interpretation of the data. Combination of these two factors creates explosive conditions with high risk of, mostly unintended, misunderstanding or misinterpreting of the AFM data. This is caused mostly by ignoring or missing the common and less common artefacts or simply wrong understanding of the used techniques. To this day, many studies compiling the list of the former were published, describing the artefacts caused by the sample and tip geometry and their interaction as well as some occurring specifically during the electrical AFM experiments [69], [70]. To address the latter, we would like to dedicate a second chapter in this thesis to thoroughly assess the current-detecting techniques used in the solar-cell research with the special focus on C-AFM and its variations.

As was previously mentioned, the biggest advantage of the AFM is its flexibility, not only in number of samples that can be assessed with this technique, but also in its applications. Small change in the experiment setup or equipment or, indeed, just the data processing can lead to a completely new set of results, to the creation of new technique. This, on one hand, leads to a certain chaos in the field of the new AFM techniques, where similar experimental setups are developed and named in parallel by different groups, making the general assessment of the field rather difficult. On the other hand, it allows researchers to tweak the technique to fit their specific needs. For example, in our group, we have previously worked on developing a pC-AFM [54], correlative atomic force microscopy [17], [71], [72] and lately we have adapted the Scalpel C-AFM and C-AFM Tomography techniques for the solar-cell characterisation [73]. The next chapter will closely discuss the intricacies and shortcomings of current-detecting AFM in solar cell research together with many examples of successful applications of said techniques. Last two chapters of this thesis will be dedicated to presenting a case study of the current-pathing in the selective contacts for high-efficiency silicon solar cells using these advanced current-detecting methods and providing a short practical to-do list for performing a C-AFM Tomography measurement.

Chapter 2

Current-detecting Techniques for Solar Cell Research - a Closer Look

In this chapter, we will delve into the intricacies of current-detecting AFM and demonstrate its applicability on many levels of solar cell research. To do this, we will present mostly published or presented results on the example of Si RJ solar cells, ranging from the examination of the inner structure of the individual radial junctions to the working of the finished mini-module. In order to increase the accessibility of these complicated techniques to the larger audience of the AFM operators, we will start the chapter with the list of AFM tips appropriate for certain applications and talk in depth about the possible hurdles on a way to correctly understand and interpret results, mentioning several artifacts and deeper-lying shortcomings of the current-detecting AFM.

AFM Probes for Current Detection

As mentioned above, current-detecting techniques are enabled by, among others, conductive tips. It is here where the decision and experience of the AFM operator comes in play for the first time, choosing the right tip for the application. As it is with the normal AFM, manufacturers offer a vast variety of conductive tips with different advantages and disadvantages. We will offer an extremely limited range of very different tips that we used in our research for different purposes in order to demonstrate the advantages and disadvantages of these probes for specific applications.

The most common conductive probes are **silicon tips coated with Pt/Ir or Pt/Cr alloy** such as **MULTI75E** from Budget Sensors. These tips offer cheap and accessible baseline for all electrical measurements. Since they are the basic equipment in every laboratory that deals with current-detecting AFM techniques, we will compare other tips properties to them.

A simplest step-up from tips with metallic coating is the non-metallic conductive coating, such as TiN layer or polycrystalline diamond. These special coatings offer more stable alternative to, frankly, often whimsical metallic layer, and decreased wear of the tip shape as well. The only down-side is the tip-curvature increase and also a higher prize. For some of the measurements we used **DD-ACTA** conductive tips with polycrystalline conductive diamond coating to achieve stable and wear-resistant electrical contact. If the application requires highly conductive tip, full-metal tip can be an option. Full platinum or platinum-iridium alloy tips from Rocky Mountains Nanotechnology offer not only low tip resistance, but also eliminate the risk of coating wearing off completely. We have utilized this type of tip with success when measuring silicon radial junction nanorods, typically not very highly conductive and structurally very demanding sample. Specifically, the **RMN25Pt300-B** probes have performed exceptionally well in PF-TUNA measurements.

The crème de la crème when it comes to the conductive probes are the full-diamond highly boron-doped tips. These probes are notoriously difficult to manufacture [74], but irreplaceable in certain applications such as SSRM or scalpel C-AFM. High wear-resistance of the diamond allows for extremely high contact forces, making these probes the only conductive tips convenient for material-removal experiments. In our case **SSRM-DIA** probes manufactured in IMEC were employed with great results.

2.1 Shortcomings of the Current-detecting Techniques

Regardless of the wide spectrum of techniques utilizing the current detection, it is necessary to remember the fundamental limitations of this measurement setup. While certain specific variations have been used (with varying degree of success) to achieve quantitative results, the holy grail of the current-detecting AFM – repeatable, reliable, and quantitative measurement of the local sample resistivity applicable to the large variety of samples – is yet to be achieved. This problem can be credited to the high complexity of the current-detecting AFM system and a certain lack of exact experimental and theoretical studies alike, mostly due to how still relatively young the current-detecting AFM is. While many laboratories and groups are trying to battle this lack of experience and theoretical models, specific mesoscopic nature of AFM current measurements makes it very challenging and time demanding.

Ambient measuring conditions and wide range of tips and measurable samples are usually regarded as a big advantage for AFM, but it also complicates our ability to theoretically describe and model the exact situation of the current-detecting setup. Even without the necessity to include large variations in tip (conductive-coated silicon, various metals and doped diamonds to name just a few) and sample properties (metals, semiconductors, oxides etc.), the potentially complete theoretical model of the current-detecting circuit would also have to include aspects of macroscopic current transport (for sample itself, body of the tip, microscope parts. . .) as well as quantum current models for the tip-sample contact that concerns very limited number of atoms (when considering the electrical contact to be only few nm squared [74], [75]) as well as the dynamic nature of the AFM measurement with electrical and mechanical contact changing many times per second. This instability of the electrical contact is caused by a plethora of effects, including the geometry of the tip and the sample, ambient conditions [76]–[78], forces induced by the voltage bias [79] etc. The theoretical model of our system must therefore be highly complex. Modelling of certain aspects of this complicated system was attempted in the past by various groups [80]–[82], but there is still no universally-recognized answer. While we hope the over-arching exhausting model of current-detecting AFM will be eventually achieved and will enable the current-detecting AFM to fully deliver on the expectations in the nano-electronics and photovoltaics field, it is necessary to understand the current limitations of these techniques and apply them carefully only in those cases where certain conclusions can be safely drawn.

2.1.1 Tip-Sample Contact Resistance

During the measurement, we detect current flowing through a circuit that consists of the microscope, the probe tip, cantilever and chip, sample and all the interfaces between them. Influence of the microscope is usually considered only for measurements where all other involved resistances are very low. Disregarding the inner resistances in the microscope itself, the situation is still far from ideal, as is demonstrated in Figure 2.1 [83]:

Aside from spreading resistance of the sample ($\mathbf{R}_{SR}$) we can see that the measurement is dependent on the resistance of the tip ($\mathbf{R}_{tip}$) that changes with the tip material and shape. Not included in the picture is the resistance of the sample table and electrical contact between the table and the sample that is usually considered ohmic. Most problematic part of the measurement circuit is, however, the electrical contact between the tip and the sample.

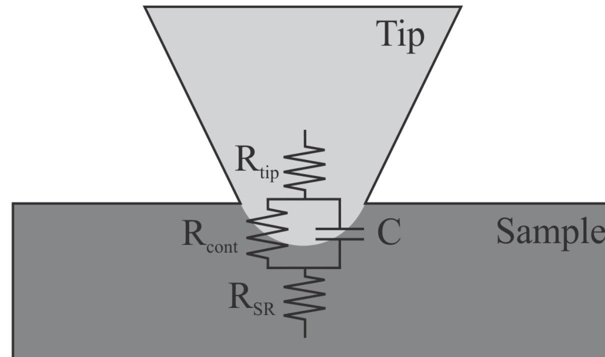

Figure 2.1: *Parasitic resistances present during the contact between the tip and a sample, as taken from O'Harey [83]*

Keystone to all of the current-detecting techniques is the tip-sample contact modelled in Figure 2.1 with resistance $\mathbf{R}_{cont}$ and stray capacitance **C**. In the following paragraphs, we will wilfully ignore the capacitance aspect of the contact and R_{cont} will be the main focus, since all the studies presented in this thesis are mostly focused on resistivity of the samples, not their capacitance. Besides, analysing at least some of the elements influencing the exact value of the R_{cont} is a significant task. It is affected not only by the area of the mechanical contact (various tip and sample shapes can influence and dynamically change the contact area), but also the formation of the electrical contact (that is notably different from the mechanical one), present atmosphere and humidity, water layer and its chemical composition, normal force between the tip and the sample etc. We also have to realize that during the current-detecting measurements, current flowing through

the nano-sized tip-sample contact can reach relatively high current-densities, causing the Joule heating – this can, in turn, effect the tip or sample geometry, melt metallic coating on the tip etc. All of these effects and many more have to be taken into consideration when you interpret the detected current. While there is relatively large number of studies of the environmental effects on the current detection [76], [78] (with unsurprising conclusion that the optimal results can be achieved in protective atmosphere such as nitrogen one or, even better, in vacuum), we would like to focus on closer understanding of the sample geometry, tip-sample electrical contact and its evolution with changing normal contact force between the probe and the sample.

Influence of the Sample Geometry

The first effect we will discuss is the influence of the sample and tip geometry. This effect is both very simple to understand and very common in C-AFM measurements. To understand how sample topography as well as the tip shape can change both mechanical contact and the tip-sample contact force (while constant setpoint deflection is maintained), one does not have to delve into quantum mechanics, simple geometrical idea will suffice. In the ideal case of measuring perfectly flat sample with perfectly round tip, mechanical (and presumably also electrical) contact would remain the same throughout the scan.

However, most of the samples and tips are far from this ideal state. This is especially the case for nanostructured samples that solar cells often are - when dimensions of sample features and the tip are comparable ($<$ hundreds of nanometres), their interaction can cause sudden and major changes in the contact size. This is especially important for current-detecting AFM methods, since the detected current is expected to be directly dependent on the size of the electrical contact. Previously introduced sample of Si NW-based RJ solar cell is a perfect candidate to demonstrate this effect – Figure 2.3a schematically shows the situation of C-AFM measurement on the array of nanorods.

During the scan, the tip is continuously switching between the positions A and B – in position A, detected current comes solely from a singular contacted nanorod. When moving from one nanorod to another, the tip is briefly contacting both neighbouring nanorods, detecting effectively a sum of the current signals from both (position B). This will cause a sudden increase in detected current that can be, by an inexperienced operator, interpreted as more conductive border between the two features, especially when you switch the nanorods for crystalline grains for example. Similar effects can be observed on sloped surfaces where the angle of the slope comes close to the tip apex angle.

IMPACT OF THE SAMPLE GEOMETRY ON C-AFM

Goal of the experiment: Demonstrate some of the possible artefacts occurring during the C-AFM measurements on the nanostructured samples that can be credited to the geometry of the sample.

In the low-force regime of the C-AFM, many things play a role in establishing a tip-sample contact. Geometry of the sample is an easy influence to spot, yet it is often overlooked when authors interpret their results. This is especially the case for so-called grain boundaries measurements, where increased current signal between grains is more often than not a geometrical effect rather than a phenomenon connected to electrical properties of said boundaries. In our case, we demonstrate this artefact on the Si RJ nanorods, nanostructured sample with dimensions comparable to those of the utilized tip.

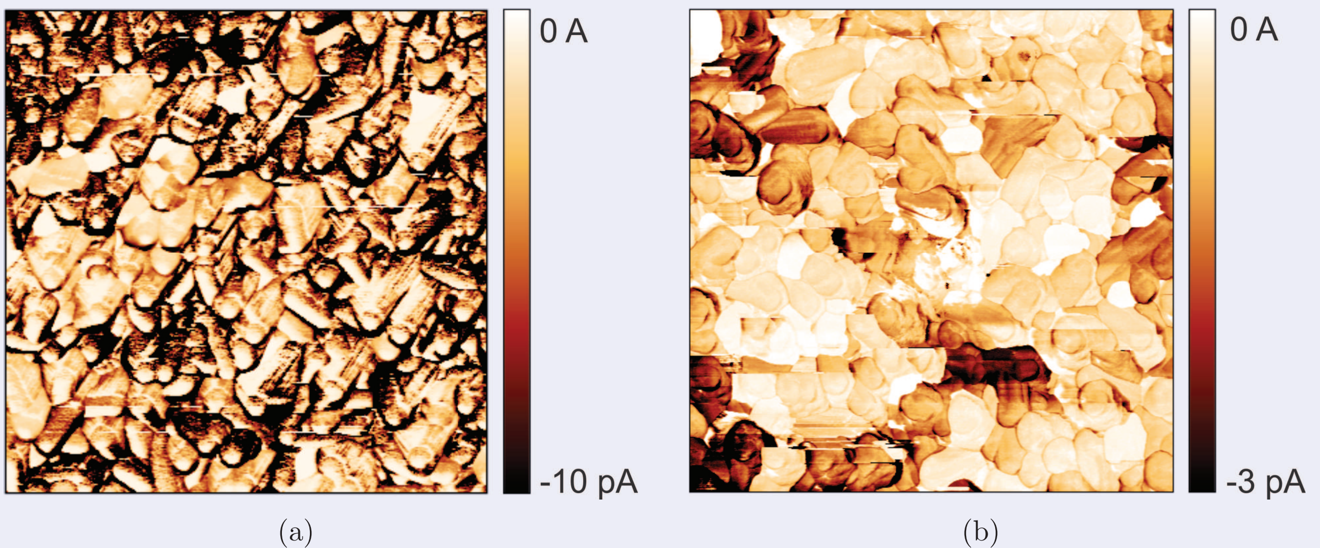

Figure 2.2: *Low-force C-AFM with (a) conductive-coated AFM tip, (b) full-metal tip and higher contact force applied.*

In Figure 2.2 we can directly compare conductive measurements with two kinds of setups – the left one, performed in PeakForce TUNA with metal-coated silicon tip and applied contact force of 10 nN (Figure 2.2a), exhibits much stronger current signals around the edges of the nanorod tips and on some oriented slopes of the nanorods. This increased current signal has no direct origin in the sample properties, it is merely a geometric artefact caused by the sudden increase of the contact size on sloped surfaces (like the nanorod edges and angled sides) and when contacting two or more nanorods at the same time. To confirm this, we can compare the results to the different measurement on the similar kind of sample – this time performed with full-platinum RMN25Pt tip that allows for higher contact forces, since there is no fear of loosing the metal coating due to the high contact forces (Figure 2.2b). As previously discussed, this diminishes the tip-sample contact resistance to a degree. Therefore, in this scan, most of the geometry-artifacts are eliminated apart of the slight increase of the current on the borders between the individual nanorods, that can be ascribed to contacting both neighboring nanorods at the same time for a brief period of time. However, as apparent from certain sudden

changes in the current signal, the higher contact force is causing a permanent damage to the sample, breaking some of the nanorods during the measurement. Seemingly counter-intuitive lower average current signal achieved with the full-platinum tip is caused by the lack of external illumination for the second scan. It is also worth noting that current-signal similar to the one observed in Figure 2.2a could be caused by the inhomogeneous wear of the tip metallic coating.

Conclusions: When measuring with relatively low contact forces (that can be mandated by the metal-coated tip for example), one has to be aware of possible geometry-induced artefacts as demonstrated in Figure 2.2a caused by sudden changes in tip-sample mechanical and electrical contact. These artefacts can be mitigated by switching tips or increasing the setpoint, if one or the other option is available.

Presented on SPM Workshop Lednice 2019

Measuring on the inclined sample may cause another complication in connection to the tip-sample contact. Since optical lever detects the deflection of the cantilever only in one direction - parallel to the z-axis of the microscope - decomposition of forces caused by the slope can lead to changes of the contact force between the sample and the tip – such is a case depicted in Figure 2.3b. In the case of our example, normal load **N**, directly influenced by the feedback-controlled cantilever deflection, translates into different contact force **F** on the top of the nanorod and $\mathbf{F}_S$ for the sloped side of the nanorod. In this case, $\mathbf{F}_S > \mathbf{F}$ and can be decomposed into two forces, $\mathbf{F}_1$ and $\mathbf{F}_2$, where $\mathbf{F}_1$ is balanced with **N** . As we will discuss below, this can be crucial to determine the R_{cont} value.

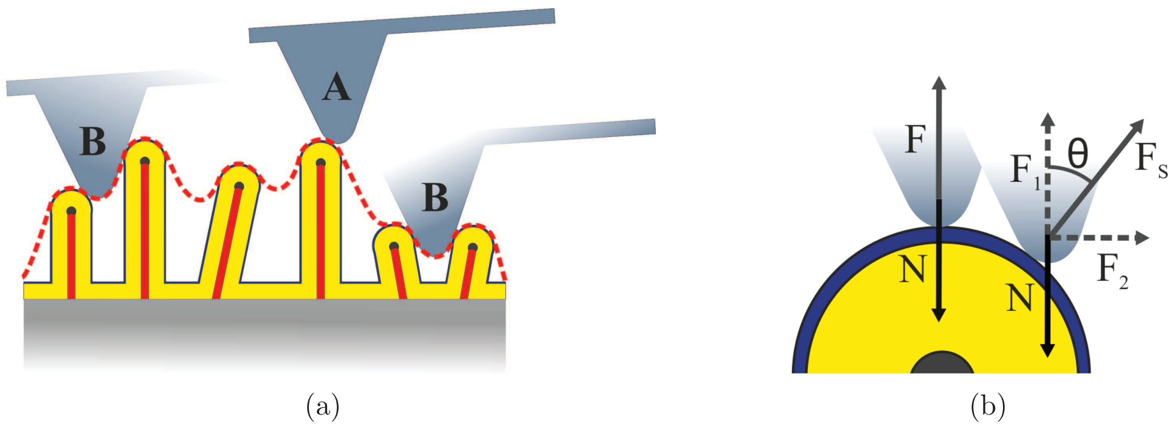

Figure 2.3: *Schematic demonstration of increased (a) mechanical contact area and (b) contact force caused by the sample geometry. Subfigure (b) inspired by [84]*

Mechanical vs Electrical Contact

The question of mechanical contact modelling for AFM applications is difficult enough, with researchers sometimes utilizing simple Hertz mechanical model [85], [86] - elastic contact between a plane and a sphere representing the AFM tip - others choose to go beyond it by adding additional forces and material deformations in order to assess the contact more accurately [44], [87]–[89]. To complicate the issue even more, it has been experimentally proven that the electrical contact is not identical with the mechanical one. While the mechanical contact represents the upper limit for the electrical contact area, the electrical one is often smaller and sometimes even significantly so. After all, it is logical to expect charge carriers to look for the simple path with lowest resistance through the complicated tip-sample junction. Notably, this effect can be very well demonstrated with full diamond probes, that are most of the time relatively blunt (tens - hundreds of nanometres) but can facilitate even sub-nanometric electrical resolution [75]. Apparently, the size of the electrical contact is not only influenced by the local atomical roughness of the sample, but also the magnitude of the tip sample contact force.

Force-Current Curves

In order to assess the influence of the contact force on the tip-sample resistance or rather the detected current, one can utilize the tool of force-current curves, i.e. ramp the tip z-position with constant tip-sample bias while measuring changes in the detected current. While the method of SSRM, utilizing extremely high contact forces, has been known to produce better quantitative results then standard low-force C-AFM, the grey area between the two approaches has been seldom explored. However, *Schulze et. al.* reported in 2013 a peculiar shape of the detected current signal curve in the p-doped Ge upon the gradual increase of the contact force, as can be seen on Figure 2.4. In their research, authors explain this sudden drop in R_{cont} by changing the material phase of the Ge to β-Sn phase that allows for the ohmic-contact formation between the tip and the sample. They further extend this theory to Si as well. While this interpretation of the result is not completely accepted in the community, it is indisputable that R_{cont} drops significantly when the contact force is increased in the range between 0-500 nN. In our experiments on golden substrate we observed identical behaviour of the current curve on the fully metallic sample. Apart from the possible phase-transition, changes in the tip-sample mechanical contact (tip is immersed deeper into the material, achieving larger contact area) as well as possible pressure-induced reconstruction of the tip and sample micro-roughness could possibly at least partially explain a significant increase of the detected current.

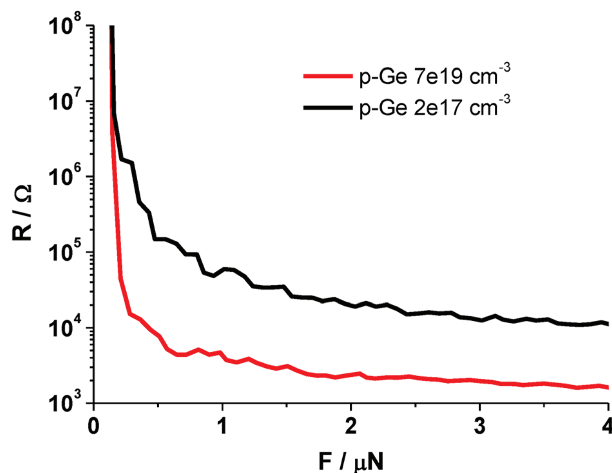

Figure 2.4: *Spreading resistance of two differently doped Ge samples during a force ramp calculated from the detected current, taken from [90]*

FORCE-CURRENT RAMPING

Goal of the experiment: With the end goal of expanding our understanding of tip-sample contact resistivity R_C behaviour with changing contact force, we aimed to explore the detected current dependence during the force ramp.

We designed and created a special sample – three golden rectangles created using gold sputtering in series with three different resistors, making three measurement areas with well-defined resistivities – 100 kΩ, 1 MΩ and 10 MΩ. We assume the gold resistivity to be insignificant in comparison with the resistors. After several experiments, we decided to use the 10MΩ one for our force-current ramping.

Using the highly boron-doped diamond tips, we established mechanical contact with minimal contact force and ramped the force up to 550 nN and back. Given the constant small negative bias between the sample and the tip, we expect all the detected negative current changes to be a direct result of the force ramping (and subsequent tip-sample contact resistance changes caused by the force increase). Given the constant voltage bias, we recalculated detected current to resistivity.

Result of the ramp is depicted in Figure 2.5:

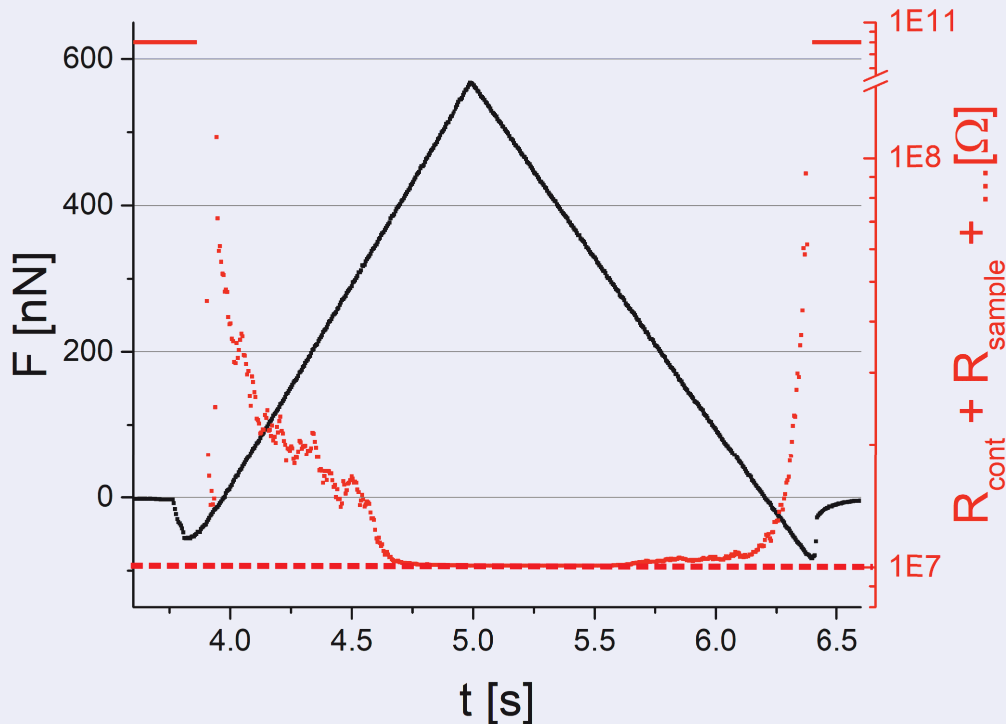

Figure 2.5: *Resistance calculated from the current signal detected during the force ramp with constant negative bias applied*

With increasing contact force, the absolute value of current grows, showing the drop in the resistivity. At around 400 nN the resistivity settles at $10^7\Omega$, the expected sample value. This marks the switch

between what we call low-force and high-force regimes, when the tip-sample resistivity becomes negligible in comparison to the sample. Resistance at the zero force is limited by the current amplifier noise level, that corresponds to $R=8\cdot10^{10}\Omega$. As is apparent from the group of chaotic current points in the section of the minimal contact force, the contact at the low-force regime can be very volatile and unpredictable. It is important to note that the specific point of the "switch" is always different and experiment-specific. These findings are consistent with results achieved by other groups in the similar kind of experiments.

Featured drop of the tip-sample resistivity is expected, but not fully explained in the literature. The role of the increasing mechanical contact is probably undeniable. On the other hand, several other effects have been mentioned before.

Conclusions: Without the need to explain the exact mechanisms behind the R_C drop, we can report that the R_C can be suppressed with increasing contact force. Depending on the sample resistivity, the threshold contact force is usually around several hundreds of nN, going to µN in case of rather conductive samples. While the R_C seems to be dropping relatively fast with increasing contact force, such forces are probably damaging to most of the samples and tips alike, further highlighting the limited use of the high-force C-AFM.

Presented on SPM Workshop Lednice 2019

How to Outwit the Tip-Sample Contact Resistance?

The above presented graphs of force-current curves hint a possible solution to our problem. In their struggle with the tip-sample resistance several authors reported that this nuisance is reduced with increasing tip-sample contact force. With decreased R_{cont}, role of the sample and the tip resistance becomes more prominent, leading to the desired result – attentive reader easily recognizes the description of SSRM we mentioned above. However, increase of the contact force comes with a high prize – contact forces required to achieve such a significant drop in tip-sample contact resistance do (with the exception of the hardest materials) deform tip and often even damage the measured sample, taking away a different defining characteristic of AFM – non-destructivity of the measurement. Nonetheless, the data obtained by such measurement is certainly worth the hassle. Certain samples, like cross-sections of silicon wafers and such, can withstand necessary forces with none or limited loss of structural integrity. When highly durable tips (doped diamond for example) are used, it is possible to measure changes in sample conductivities and after calibration, this method can be used to directly measure changing Si wafer resistivity with the doping levels [39], [67]. Such experiments have been performed and remain, to authors knowledge, the sole application of current-detecting AFM technique to gain direct quantitative data regarding local sample resistivity. However, SSRM and similar high-force techniques are a privilege of hard and sturdy samples and simply impossible to apply universally: large contact forces during any AFM measurement on our Si NW RJs could easily lead to the so-called shaving of the nanorods – AFM tip would simply detach the wires from the substrate, creating a small clearing in the NW forest.

While any quantitative results from low-force C-AFM may seem almost impossible to obtain at this state, there are still possible useful applications of this technique. Everything becomes slightly easier when we make a strong assumption that the tip-sample contact resistance remains constant (albeit practically unknown) during the measurement. Then, even though we still cannot separate the current drop caused by the sample resistance and the tip-sample resistance (although there has been a valiant effort made in this regard [91]), we can at least observe the changes of the over-all current in time and presume the origin of these changes to be connected with certain sample properties for example. Regardless how strong this assumption may seem, it has been successfully used in the past to obtain interesting results. For example, one can assume the tip-sample resistance to be constant on the very flat sample of the Si oxide and credit the changes of the detected current to oxide thickness, effectively using the current-detecting AFM to measure the surface-oxide thickness. When the most obvious artefacts are eliminated

and sufficient care is taken to keep the contact force within some reasonable range, it is possible to obtain qualitative maps of detected-current differences and accredit them, with a reasonable certainty, to the sample rather than to the changes in R_{cont}. However, these qualitative changes should not be simply described to the sample conductivity, for example, as that is more often than not an over¬simplification to the point of an error.

QUALITATIVE MAPPING OF THE Si NW RJs WITH LOW-FORCE C-AFM

Goal of the experiment: While low-force C-AFM cannot, as we discussed, offer a reliable quantitative results, it can still be used to generate maps of qualitative distribution of electrical properties of the sample. In this experiment, we use it to visualize current distribution over large number of individual Si NW RJs in order to analyze the connection between the RJs electrical geometrical properties.

C-AFM maps on RJ solar cells show inhomogeneous distribution of measured current among the nanorods as can be seen in Figure 2.6. To avoid local oxidation of the sample, negative voltage of -5V was applied during the measurement, therefore the measured currents are also negative. From Figure 2.6a we can see that while measured current changes from nanorod to nanorod, it remains constant for individual RJ nanorods. We therefore assume that the settings of the measurement provide for stable tip-sample contact throughout the scan as well and the qualitative differences come directly from the properties of the measured RJs.

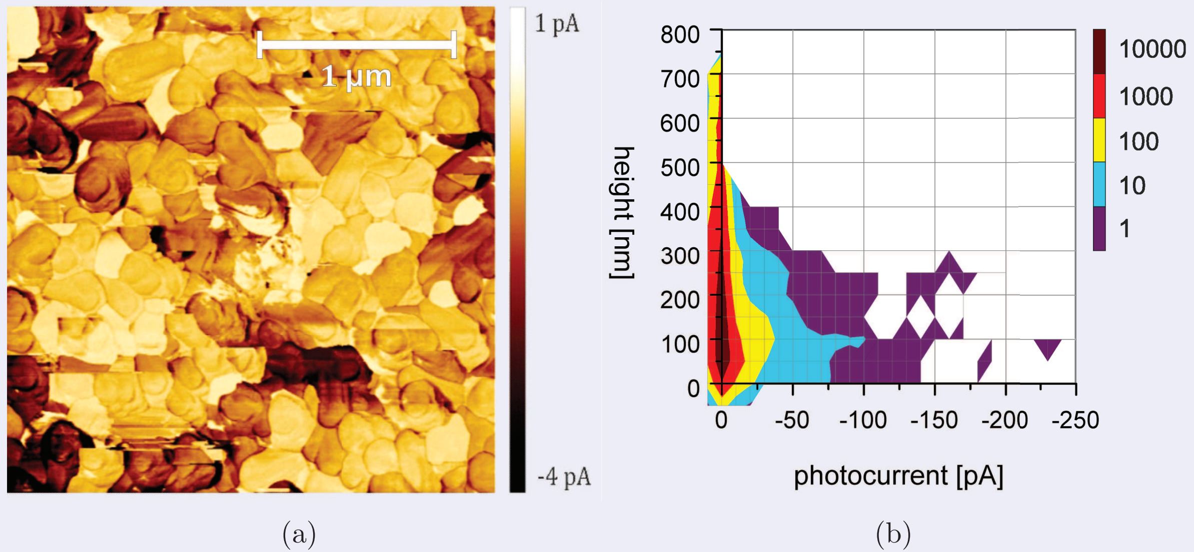

(a) (b)

Figure 2.6: *(a) C-AFM signal of Si NW RJ; (b) bi-variant histogram of the presented C-AFM scan*

We studied the relation between the nanorod measured height and the value of the corresponding current. To show this dependence, we constructed a bi-variant histogram with topographical height and measured photocurrents on axis y and x respectively (Figure 2.6b). Results indicate that while the tallest nanorods (> 1 µm) show the smallest current signals, current measured on the shortest ones varies from 0 to -10 pA.

We suggest that the measured current signal is a result of several effects. First effect to asses is the quality of the junction, here measured in the reverse direction - when we bias the PN (or PIN) junction, the current flowing through it strongly depends on its orientation. When the p-doped

region is connected to the positive voltage terminal, in so called forward direction, the current exhibits exponential increase with increasing bias. When we connect the p-doped region to the negative terminal, the junction is contacted in the reverse direction. In this case, the current flowing through is extremely low, until a threshold voltage bias is reached. We call this a breakdown. After breakdown, the current flowing through the junction increases rapidly. Current flowing through the junction in reverse direction as well as the breakdown point are determined by the properties of individual layers constituting the PIN junction, such as their thickness or dopant concentration. In the following text, we will describe these properties with an umbrella term of junction quality. Second effect is the inherent resistivity of the core c-Si NW. Since the conductivity of the NWs is orders of magnitude higher then that of the amorphous layers completing the PIN junction, their resistivity should play important role in the charge carrier transport as well.

Since we are applying negative bias on the sample holder, that is conductively connected to the bottom electrode of the sample and therefore to the p-doped Si NWs in the RJ core, our sample is measured in reversed direction.

Presented histogram shows large range of detected currents on short RJs (<500 nm). This indicates that their junction quality is probably very diverse. That is not surprising, given the random nature of the NW scaffolding used to create RJs. On the other hand, as the nanorods get longer and longer, resistivity of the core NW takes over, making the current measured on their ends extremely low.

Conclusion: Using the low-force C-AFM we were able to map differences in the detected current over hundreds of Si NW RJs. With construction of the height-photocurrent 2D histogram we were able to demonstrate a connection between the RJs geometrical and electrical properties.

Presented at ACEEES forum 2017, published in JJAP 2015 [17]

2.1.2 Sample Current Generation

Previously discussed aspects of the current-detecting AFM are true for every kind of sample. However, everything gets even more complicated when we bring solar cells into the picture, since the relatively simple model circuit presented in Figure 2.1 has to be modified to reflect the presence of the photodiode. Results of this modification is depicted on Figure 2.7.

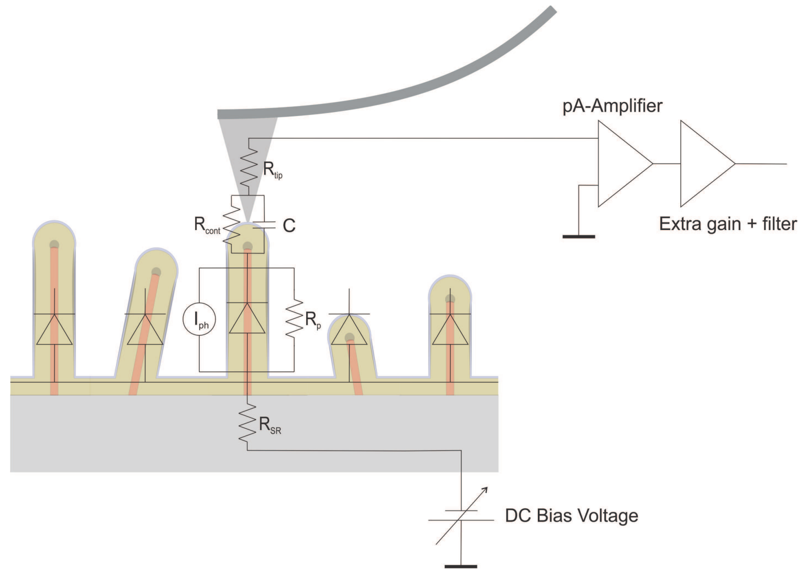

Figure 2.7: *Modified scheme of the C-AFM setup for the case of measurement on PIN RJs.*

We can see that the addition of solar cell sample further complicates the situation. The sample itself is generating current during measurement adding to the current induced by the voltage bias applied externally. Therefore, the detected current cannot be interpreted simply on the basis of the Ohm's law. Additionally, depending on the bias polarity and diode orientation, measured photovoltaic device is either characterized in the forward or reversed direction. It is necessary to pay close attention to this fact, as the detected current signal strongly depends on it. Absolute current value detected is not symmetrical for symmetrical voltage bias.

From the properties of the photodiodes clearly follows that measured current values will largely differ for solar cell in darkness and under illumination. The role of the illumination in C-AFM experiments was widely discussed in the literature and has to be considered every time when we try to interpret the detected current in direct relation to the macroscopical properties such as short-circuit current.

2.2 Connecting Microscopical Properties to Macroscopic Parameters

While properly calibrated SSRM allows a knowledgeable user to almost directly obtain distribution of dopants for example, successfully measuring the current signal with low-force C-AFM is only half of the battle. Indeed, looking for possible connection between the measured current signal and any relevant macroscopic property of the solar cell is probably the more difficult part of the whole characterisation process. While the attempts have been periodically made in the past [25], [26], [29], [53], all of them included very demanding assumptions on the samples and the technique alike. Most of these attempts included photoconductivity mapping, as solar cell properties are fundamentally linked to the reaction of the material to external illumination. Effort has been made to introduce scanning probe microscopy version of electroluminescence measurement [92], since there is a direct connection between the solar cell electroluminescence signal and its EQE [93], [94]. Many authors attempted to combine AFM-based techniques with other characterisation methods in order to map open-circuit voltage, short-circuit current or local efficiency [25], [40], [95].

Using the diamond Vickers-type indentation tip to create a triangular set of square marks that may act as an origin of a reference system on the sample surface, we were able to correlate standard C-AFM, KPFM or SEM to look for the connection between the C-AFM detected current and other sample properties.

Specific cases apart, direct interpretation of low-force current-detecting AFM, as well as other electrical AFM methods, is significantly hindered by the R_{cont} unpredictability. While the effort in this direction will most likely never cease, it might prove extremely difficult to correlate local properties detected on the solar cell surface by AFM to the macroscopically observed behaviour originating in the material volume. Nevertheless, the possible applications of AFM in solar cell research is not limited to this task.

PHOTOCONDUCTIVE C-AFM

Goal of the experiment: Presenting the significance of the external illumination on collected current signal. When dealing with solar cells, one has to always note all the sources of external illumination and keep in mind that they will influence the result of C-AFM measurement.

As for all photo-sensitive materials, we must take into consideration the parasitic illumination of the laser diode used as an optical lever and its influence on current signal of RJ nanorods. Unless stated otherwise, in all our measurement we use red guiding laser with the wavelength of 650 - 695 nm. In case of silicon samples, this is a serious issue that cannot be dismissed [54]. Since we deal with the solar cells, i.e. materials that are, by definition, reacting on external illumination by generating electrical charge carriers, there is a significant difference between dark current and photo-current measured during C-AFM. To illustrate the Si NW RJs reaction to external illumination as well as to AFM laser diode, we present Figure 2.8.

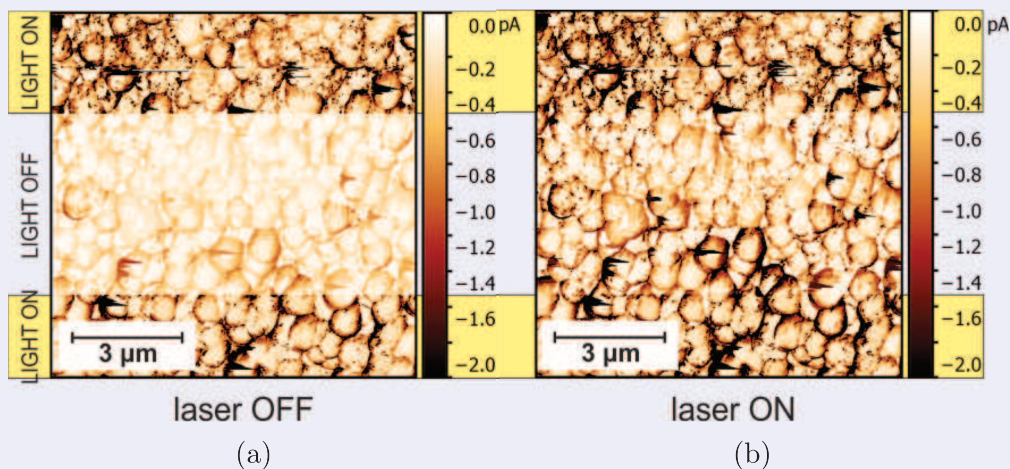

Figure 2.8: *Reaction of the C-AFM signal to external illumination. Pictures taken (a) without the guiding red laser and (b) with it.*

In this experiment, we have switched the external white illumination off and on to observe the current drop expected for RJs. Using the dark lift mode, a two-pass technique where we turn off the guiding laser for the second pass, tracking the measured line only based on the topography profile obtained during the first pass, we were able to obtain a map uninfluenced by the guiding laser radiation (Figure 2.8a). To compare, we have also recorded the current map with the red laser on (Figure 2.8b).

From these pictures, we can see that not only is the current detected on the illuminated sample in Figure 2.8b generally higher (-1 pA compared with -0,77 pA achieved without laser), the drop after the illumination is turned off is also lower with the laser turned on (0,42 pA with the laser vs. 0,55 pA without it). This shows that the guiding laser is responsible for non-negligible portion of detected

current signal and it must be always taken into consideration when one is discussing quantitative results.

Conclusion: Si NW RJs are sensitive to external illumination, including the red guiding laser of the microscope. This influence is difficult to eliminate and requires utilizing so-called dark TUNA mode, two-pass measurement that allows to turn the laser off during the scan. Implementation of this technique is, however, very impractical for higher work flows. In this logic most of the C-AFM results presented in the literature should be interpreted as photoconductive AFM, unless the guiding laser is either off or operates on the other-then-usual wavelength, such as near infrared (IR).

MEASURING THE INNER JUNCTION QUALITY

Goal of the experiment: To be able to connect the general quality of detected current to a relevant attribute of the characterized solar cell, we strive to further investigate the origin of the current signal on top of RJs

Using the diamond Vickers-type tip, we indented the sample, crushing several thousands of nanorods and destroying their inner structure. Subsequently obtained C-AFM map can be seen in Figure 2.9. Experiment was conducted on the PIN nanorod sample with negative bias applied to the sample (i.e. reverse diode conditions, see Figure 1.2). As we can see from the current signal in Figure 2.9a, all the RJ nanorods influenced during the indentation process show higher currents compared to the rest of the sample. This might suggest that the indentation of the nanorods destroyed the PIN junctions alltogether.

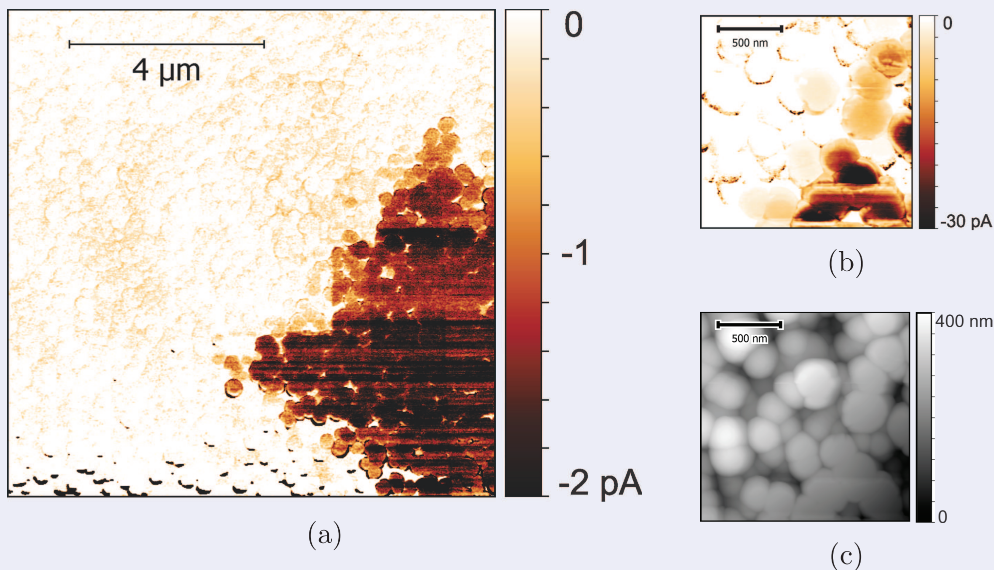

Figure 2.9: *C-AFM measurements performed in the vicinity of the indentation mark (a, b) and the corresponding AFM topography detail (c).*

Figure 2.9b and Figure 2.9c show a current and topography signal of a smaller area to further demonstrate the fact that all the nanorods with higher current signals are topographically damaged. This proves not only how significant is the quality of the inner RJ for resulting C-AFM signal of the nanorod, but also the fact that local shunts caused by individual nanorod failure do not influence the properties of the neighbouring RJ nanorods, as we can see from extremely sharp borders of the area with elevated C-AFM signal.

Conclusion: Our conductive measurements on RJ nanorods prove that C-AFM can be a useful tool to assess the quality of a solar cell, namely PIN or NIP junction inside it, as we can clearly differentiate between the complete functional RJ and a crushed one. Additionally, demonstrated independence of the electrical properties of the neighbouring individual RJs is crucial for constructing a well-functioning solar cell from our nanorod arrays.

CORRELATING THE C-AFM AND SEM STUDY OF THE Si NW RJs

Goal of the experiment: In order to examine the possible correlation between the Si NW RJs length and their current signal, we employ a correlative microscopy – a tool that allows us to directly compare the same spot on the sample with different microscopical techniques.

While the previous experiment demonstrated clearly that the highest nanorods exhibit lowest current, this result is far from a proof that the length of the RJ nanorod correlates with its electrical properties. While the high nanorod has to be long, this does not hold the truth in the other direction since the nanorods grow in a random angle from the surface and can therefore be variously inclined – this could also explain the fact that points with low topographical height demonstrate such a wide range of detected currents. In order to asses the real length of the RJ nanorods it is necessary to visualize them with SEM from different angles. Using the diamond Vickers-type tip, we created a series of marks of the sample that allowed us to repeatably locate the identical spot on the sample with SEM (Figure 2.10a), topography AFM measurement (Figure 2.10b) and C-AFM (Figure 2.10c).

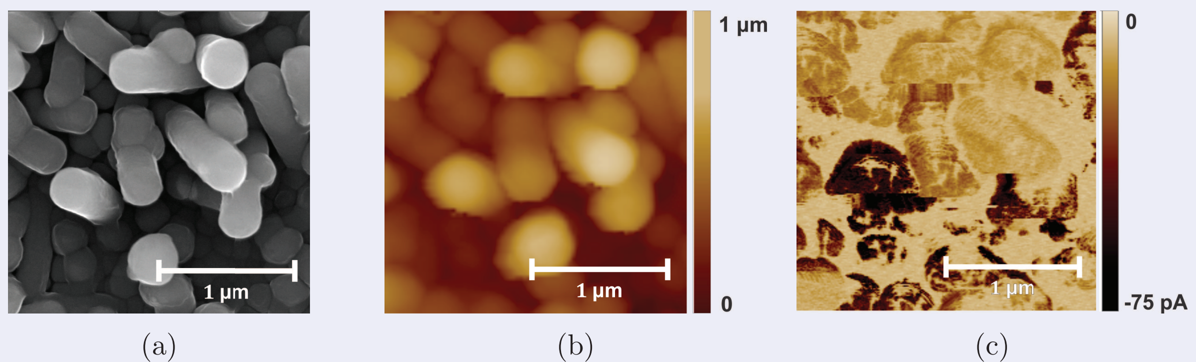

(a) (b) (c)

Figure 2.10: *Correlative microscopy on individual nanowires depicted with (a) SEM, (b) high-resolution AFM and (c) C-AFM*

Upon locating the three differently conductive nanorods with SEM we observed them under several angles, confirming the following information: Nanorod on the right is the longest one (cca 1 µm), while also exhibiting the lowest current signal. Middle nanorod is the shortest one (<500 nm), but its current signal is only slightly higher than for the first one. Finally, the left nanorod is the most perpendicular to the surface, exhibiting the length of circa 700 nm and also the highest current signal.

Conclusion: This direct comparison between the C-AFM and SEM techniques, enabled by the process of correlative microscopy, further proves our observation that there is more than one source of the non-uniformity in the RJ nanorods array, since the measured length of three studied nanorods does not follow the pattern of their respective detected currents. It also demonstrate how powerful the correlative microscopy can be, further elevating the possibilities of each technique.

Presented on Microscopy 2016, Lednice, CSMS and SPM Workshop Lednice 2017

2.3 Further Applications of AFM on Solar Module Architecture Level

While measuring qualities known from the macroscopic characterization techniques may be attractive application of electrical and current-detecting AFM specifically, it is not the only one. Assessment of the active layer of a solar cell is only a part of the long process of perfecting a solar-cell. In fact, complexity of standard C-AFM interpretation calls for an inventive approach in C-AFM applications in solar-cell related research. This search has given rise to a large number of applications, from mapping the charge-carriers generation [96] and their transport across the multi-layered structure of a modern solar cell [58], [97], [98] to the shunt detection in the process of solar-cell module construction. We will close this chapter with an experiment conducted on RESISCOPE equipped microscope in PICM lab at Ecole Polytechnique in Paris.

APPLICATION OF C-AFM ON SOLAR MODULE INVESTIGATION

Goal of the experiment: On top of determining electronical properties of individual radial junctions, C-AFM can be further applicable for characterization of fully constructed solar cells. In the following experiment, we will demonstrate the applicability of standart low-force C-AFM during the solar module construction.

In contrast to all previous C-AFM measurements, folowing experiments were performed on Agilent 5600 microscope equipped with logarithmic pre-amplifier RESISCOPE. Logarithmic pre-amplifier allows for detection of high range of currents spanning over several orders of magnitude. Often used for SSRM, this specific amplifier's software allows for "direct measurement" of the sample resistivity, using Ohm's law to directly convert detected current to sample resistance. As we discussed previously, this approach is hard to justify for any measurement performed in the low-force mode. That being said, the ability to simultaneously detect high range of currents is very useful when assessing materials or structures with highly differently conductive parts (like a solar cell).

In our case, 5x5 cm^2 solar-cell module with active layer of PIN RJs was created using laser scribing and utilizing indium-tin oxide (ITO) and fluorine-tin oxide (FTO) as top and bottom electrode respectively. Unfortunately, the final efficiency of resulting mini-module was lower than expected from previous characterization of individual layers and experimental small-area solar cells. In order to analyze the current flow through the complicated multi-layered structure of a solar-cell module we decided to utilize C-AFM, hoping that it would not only be able to determine the problematic layer or technological step, but using the unique nanometrical resolution it would also be able to directly pinpoint the problem.

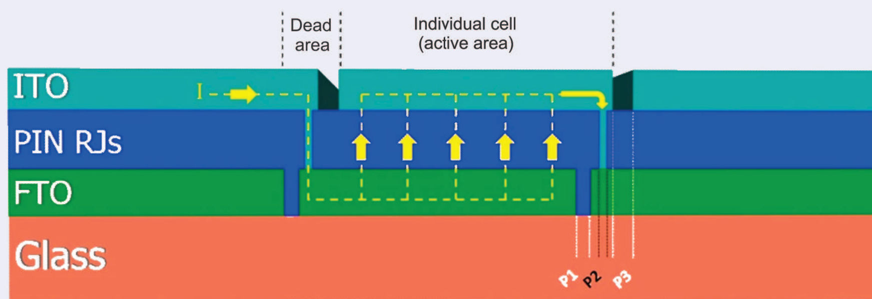

Figure 2.11: *Schematics showing the geometry of laser-scribed mini-modules. The yellow dashed line illustrates the electrical current path through the interconnected cells. Taken from [99].*

Our Si NW RJs solar cell construction starts with bottom electrode made from FTO of nominal thickness of 600 nm on the soda-lime glass substrate. Subsequently, a layer of Si NWs is grown by VLS technique using tin nanoparticles extracted from the FTO layer with hydrogen plasma at 200°C and topped with hydrogenated microcrystalline silicon oxide layer. Top electrode is realized by

sputtering ITO on top of the formed RJs, creating non-homogeneous layer of material with thickness of up to 100 nm. In order to create an above-mentioned mini-module, layers were divided into sections using laser-scribing, that was supposed to effectively electrically separate individual solar cells from each other. More details on the sample and its preparation can be found in the literature [99].

As we previously mentioned, the performance of the resulting mini-module was not as high as expected, leaving the laser scribes as a main suspect, since it was the only added technological step compared to the simple solar cell. In order to investigate the ability of the laser scribe to electrically isolate the neighbouring solar cells, we performed two large-area scans on both sides of the scribe on the sample missing the top electrode, that usually performs the role of a conductive connection between the two solar cells.

First experiment was performed only on the FTO layer divided with a laser scribe. Electrical contact was on the right side of the scribe only. From C-AFM scan we can see a significant drop between the two sides of the scribe as well as highly decreased detected current (down to the detectable limit of the machine) in the area of the scribe itself. In case of the perfect scribe, we would expect the same undetectable current on the other side of the scribe, but in reality, the scribe does not run all the way to the sample's edge. Ablation of the material was also done in pulses, so there might be some conductive bridges present along the whole length of the 5 cm sample. Important thing is, the technology of creating scribes in FTO is satisfactory for our purposes.

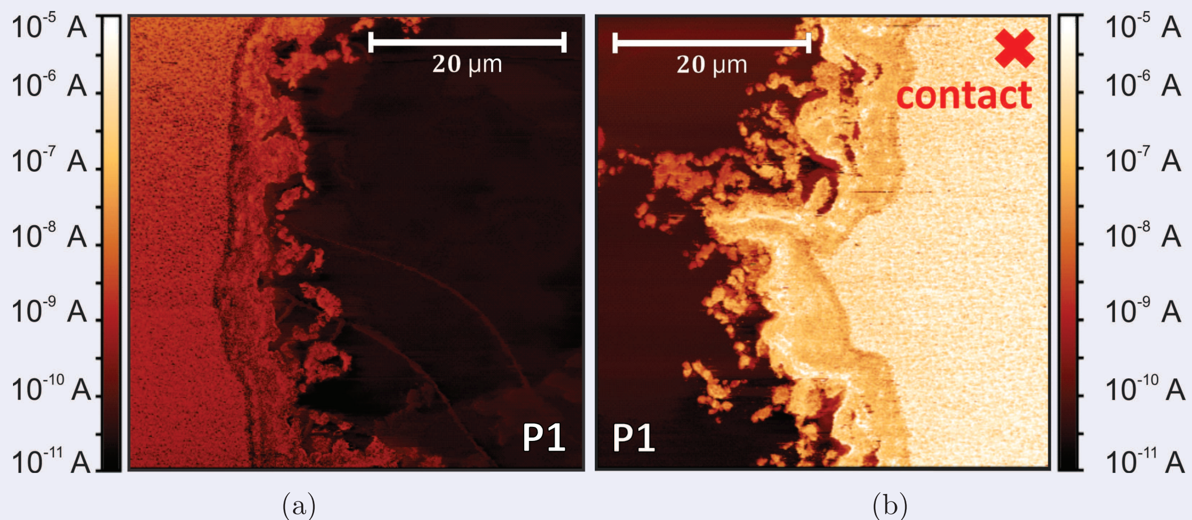

Figure 2.12: *RESISCOPE C-AFM maps of current on P1 scribe before silicon NW growth.*

In the next step, we perform similar experiment on the area with fully grown Si NW RJs. While NWs should only grow on the FTO layers on both sides of the scribe, both amorphous silicon during PEVCD and microcrystalline oxide layer are deposited on the scribe in the FTO as well. From C-AFM we can immediately see that the biggest change between clean FTO and RJs is the fact, that the nature of resistivity of the scribe and solar cell has practically switched – current detected on

the solar cell is several orders of magnitude lower while current detected in the scribe itself has risen by similar margin, therefore RJs show less current then the scribe and while it is tricky to compare absolute values between two different measurements, this qualitative switch between the scribe and its surroundings is indisputable. This is indeed very troubling, since this drop in resistivity of the scribe means that this area can act effectively as a shunt between the bottom and the top electrode. High currents detected in the scribe also suggest that the silicon layer here is no longer amorphous – either caused by the temperatures during PEVCD or microcrystalline SiO_x deposition, silicon in scribes (at least partially) crystallized, creating conductive bridge between the bottom and the eventual top electrode, that would be deposited over the sample in the last step. Further investigations with other microscopic methods revealed a residual presence of the tin from insufficiently removed FTO layer, adding another hindrance to suggested mini-module architecture.

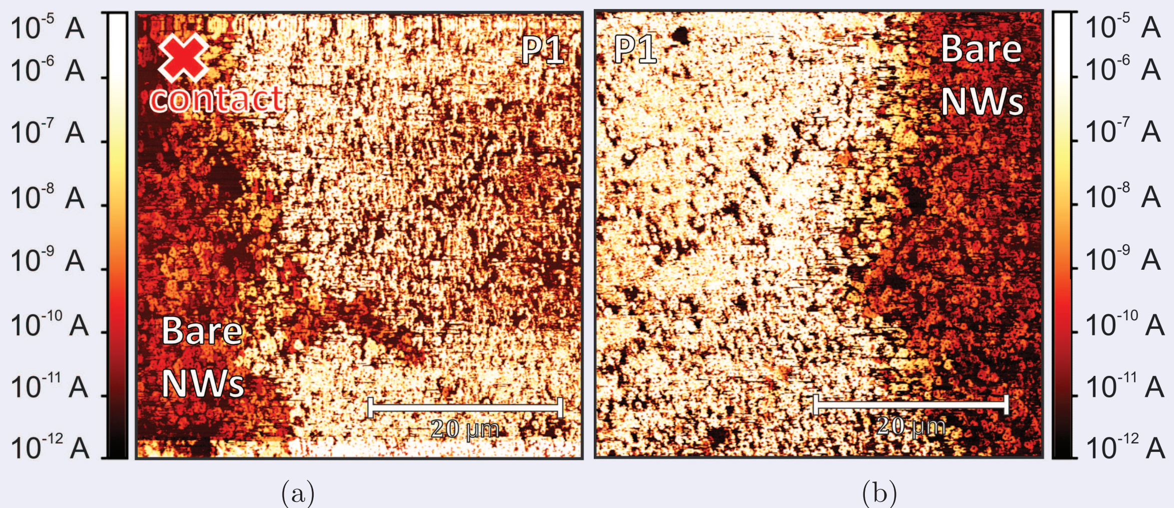

Figure 2.13: *RESISCOPE C-AFM maps of current on P1 scribe before the top contact deposition.*

Conclusion: Without making any conclusions from absolute values of detected current, we were able to demonstrate the applicability of the standard C-AFM for characterization of the complete solar cells. While we were not fully able to pin-point the specific problematic area, we used measured results as arguments to identify a P1 scribe after Si NWs growth as a problematic feature in the Si NW RJs mini-module construction.

Chapter 3

C-AFM Tomography Case Study

In previous chapters, we have discussed thoroughly limitations of the C-AFM stemming from the low-force measurement regime it utilizes. When talking about increasing the force to the point of reducing the R_{cont}, we have, so far, solely mentioned SSRM and its applications. However, this is not the only version of high-force C-AFM that exists. Lately, many authors started diverting their attention towards this direction of C-AFM, finding possible applications of so-called **scalpel C-AFM** and **C-AFM tomography** in the solar cell research and outside of it. Instead of further analysis of ins and outs of these techniques, we decided to include an extended version of paper written by the author of this thesis and published at the beginning of year 2021, proving the currency and relevance of this topic to the scientific community.

Some of the following text and figures have been used in the paper published by ACS Applied Material and Interfaces. Reprinted with permission from **Nanoscale Study of the Hole-Selective Passivating Contacts with High Thermal Budget Using C-AFM Tomography**, Matěj Hývl, Gizem Nogay, Philipp Loper, Franz-Josef Haug, Quentin Jeangros, Antonín Fejfar, Christophe Ballif, and Martin Ledinský, *ACS Applied Materials & Interfaces 2021 13 (8), 9994-10000*, DOI: 10.1021/acsami.0c21282. Copyright 2021 American Chemical Society.

3.1 Introduction

One of the traditional limitations in nowadays dominant p-type c-Si homojunction silicon solar cell technology is related to rear-contact, that combines a heavily doped region and a direct interface between the semiconductor and the metal. The former gives rise to excessive Auger recombination and bandgap narrowing, the latter to interface recombination [100]. These detrimental effects can be mitigated either by reducing the area of the metal contact and the highly doped region underneath [101], or by introducing a so-called passivating contact. This type of contact typically consists of a layer stack, where one layer effectively passivates the surface of the Si wafer and another layer acts as a selective contact for one type of the charge-carriers. One of the most prominent examples is the Silicon hetero-junction (SHJ) solar cells in which the surface passivation is provided by intrinsic hydrogenated amorphous silicon (a-Si:H(i)) deposited with PEVCD, and carrier selectivity is ensured by an in-situ doped a Si:H layer on top. Another important example is based on a thin interfacial layer of SiO_x capped with highly doped poly-Si layer, called either a poly-Si on oxide (POLO) [102] or tunnel oxide passivating contact (TOPCon) [103].

Oxide-based passivating contacts have gained great attention in recent years due to their high efficiency potential and their temperature stability which provides good compatibility with already existing industrial solar cell production lines. Today most of the important solar cell companies are putting great effort to integrate this kind of passivating contact to their pilot lines. However, majority of this work is devoted to n-type contacts whose integration is restricted to the rear side and to n-type wafers [104]–[106]. In contrast, we investigate p-type passivating contacts with a high potential for easy integration with p-type wafers, more commonly used in cell manufacturing. We use a layer stack based on an interfacial layer of SiO_x and a boron-doped layer of silicon-rich silicon-carbide (SiC_x(p)) deposited by PEVCD in amorphous phase. This layer stack, annealed at temperatures above 750°C (to promote dopant in-diffusion and partial crystallization of the doped layer), yields a high doping efficiency of the boron dopants in the layer and a lower contact resistivity. Integrated at the rear side of p-type solar cells, this type of passivating contact resulted in promising efficiencies above 22% [107]–[109].

To further increase the applicability of these contacts, it is necessary to deepen the understanding of the charge-carrier transport mechanism through the layer stack and its changes during annealing. While the thermal treatment is beneficial for doping, it was observed that annealing at temperatures above 900°C leads to the deterioration of the

implied open circuit voltage (iV_{OC}) and the fill factor (FF), suggesting a loss of surface passivation. This loss is attributed to a local SiO_x deterioration (or break-up) which can even result in a complete disappearance of the interfacial SiO_x layer [107]. The role of the local SiO_x deterioration in the charge-carrier transport is still not fully understood. There are several models describing the charge-carrier transport in poly-Si emitter devices [110]. Among these, the oxide tunneling model and oxide breakup model are the most prominent [97], [111]. Recently more elaborate investigation with temperature dependent current-voltage [97], [112] and transmission line [113] measurements suggest that the actual transport through the interfacial SiO_x is probably a combination of these models and it depends on the used oxide density and thickness. While the interface SiO_x layer was closely studied in the past, reports on the charge-carrier transport mechanism through the rest of the passivating stack are scarce [24], [114], [115].

Besides the before-mentioned scalpel C-AFM [116], [117], we perform a series of high-resolution transmission electron microscopy (HRTEM) and micro Raman measurements to investigate the relation between the annealing temperature and the electrical properties of the contact and we disentangle the roles that the interfacial SiO_x and the highly doped selective SiC_x(p) layers play in the charge-carrier transport. We use the novel technique of C-AFM tomography to study and visualize the charge-carrier transport paths through a p-type passivating contact structure. We demonstrate the presence of the preferential transport channels formed by chains of crystalline grains in partially crystallized SiC_x(p) and limit the importance of the interfacial SiO_x pin-holes.

3.2 Experimental Section

The hole-selective contacts investigated here were prepared on 200-µm-thick chemically polished 4-inch p-type float zone <100> c-Si wafers with a resistivity of 2 Ωcm. Wafers underwent standard wet-chemical cleaning. For all but one sample, a 1.2 nm thin SiO_x was formed by wet-chemical oxidation using 69 wt% diluted HNO_3 solution at 80°C [118], [119]. For a reference, a thicker thermal SiO_x (> 5nm) formed in tube furnace was used in one of the samples.

Subsequently, PEVCD operated at 40.86 MHz using silane (SiH_4), hydrogen (H_2), trimethyl boron (TMB) and methane (CH_4) as process gases was utilized to deposit 30-nm-thick a-SiC_x(p) on one or both sides of the oxidized wafer. The substrate temperature was 200°C and the power density was 0.06 W/cm^2. To mitigate a chemical reaction of the C from the deposited SiC_x(p) layer with the SiO_x, an additional intrinsic a-Si(i) buffer layer was introduced between the interfacial SiO_x and the selective SiC_x(p) layer. This layer also makes the contact stack more resilient to annealing at 900°C [107]. The samples were then annealed in an inert gas atmosphere in the temperature range of 800 to 925°C unless mentioned otherwise. The heating ramp was kept as 10°C/min, directly followed by a cooling ramp of 2°C/min, i.e., without any dwell time at the peak temperature. This was followed by a hydrogenation step to passivate electronic defects at the chemical SiO_x/c-Si wafer. To this end, a layer of SiN_x was deposited by PECVD, hot plate annealed at 450°C in ambient atmosphere to release hydrogen into the contact structure, and subsequently stripped away in 5% diluted HF.

The passivating contact structures were then characterized by several microscopical methods; HRTEM was performed on focused ion beam-prepared lamellae in a Cs-corrected FEI Titan Themis microscope operated at 200 kV. Raman spectroscopy was carried out with a Ranishaw InVia REXLEX, using a 325 nm UV laser to restrict the collection volume to 10 nm below the surface. We used 10 mW excitation power on the sample surface and a collection time of 1000 s. Bruker ICON atomic force microscope was utilized for AFM, C-AFM and its variations.

In our quest for reproducible and interpretable results, we have moved from standard low-force C-AFM towards more controllable high-force SSRM-like measurements. As the high tip-sample force applied during the measurement often leads to the removal of the sample material, we have decided to use this effect to our advantage for controlled removal of the sample surface. This way we have effectively stumbled upon the technique

previously described in the literature as Scalpel C-AFM [116], [120]. This adaptation of SSRM was first demonstrated on materials for conductive bridging memories (CBRAM) applications [75], [116], [121]. All after-mentioned scalpel C-AFM experiments consist of a single material-removing scan, representing the conductive map 1.5-2 nm below the sample surface. Furthermore, a series of high-force material removing Scalpel C-AFM scans can be performed in the same location to accumulate information on the resistivity throughout the volume of the sample by acquiring the current signal and removing a layer of the material simultaneously with each scan [98], [122]. We refer to this experiment as C-AFM tomography [123].

For 3D C-AFM tomography reconstruction presented in this work, six consecutive Scalpel C-AFM scans were performed with identical settings on the same region. After the tomography experiment, a standard AFM topography measurement showed that 15 nm of material were removed, indicating an average material removal rate of 2.5 nm per Scalpel C-AFM scan. While 6 Scalpel C-AFM measurements were performed with a continuous movement of the tip (first line of the next scan was also the last of the previous one), only 4 were used in the final analysis of the results, since most of the bottom-to-top measurements showed greatly reduced average detected current, most probably due to the asymmetrical tip contamination or uneven material removal rate. Partially to compensate for the loss of data and to sufficiently visualize the results in 3D representation, "buffer" layers generated by averaging neighbouring real-data layers were added using Gwyddion [124] arithmetic tool. To compensate for the incremental increase of the overall current caused by the thinning of the SiC_x layer, we applied dynamic scale based on relative values to individual slices. It is also important to note that the linear pre-amplifier used for current detection has a limited range and cuts the current signal when it reaches a certain threshold – this means that most of the current signal resolution is lost for the highly saturated measurements. Scans were reconstructed into 3D representation of the removed material via Drishti open-source software.

High tip-sample force and electric stability required during C-AFM tomography demands for conductive and durable tips. All our experiments were performed with full-diamond SSRM DIA IMEC tips, previously used for SSRM [74] and C-AFM tomography [116]. All the scans presented in individual figures were taken with the same tip under the same conditions during the same experimental session and are therefore directly comparable. All the samples were contacted via the bottom silicon wafer. All the current maps were taken with negative bias on the sample and all the presented values are therefore negative. When referring to 'higher' or 'lower' currents, authors are describing absolute values.

3.3 Results and Discussion

Figure 3.1 shows the standard topography (Figure 3.1a) and C-AFM results of the passivating contact deposited on one-side of the Si wafer in as deposited state (Figure 3.1b), annealed at 800°C (Figure 3.1c) and 850°C (Figure 3.1d). C-AFM image reveals current features with size comparable to topographical features apparent in all three current maps. While the pictures remain qualitatively similar, the over-all average detected current is increasing with the annealing temperature. Similar results were previously described by several groups as manifestation of buffer oxide layer breakages/pinholes [114], [115], [125] induced by the buffer-layer annealing-induced deterioration. On the other hand, Morisset et al. performed C-AFM experiments on samples missing an oxide buffer layer with similar results, speculating that the origin of these conductive spots is connected to surface states [24], [126].

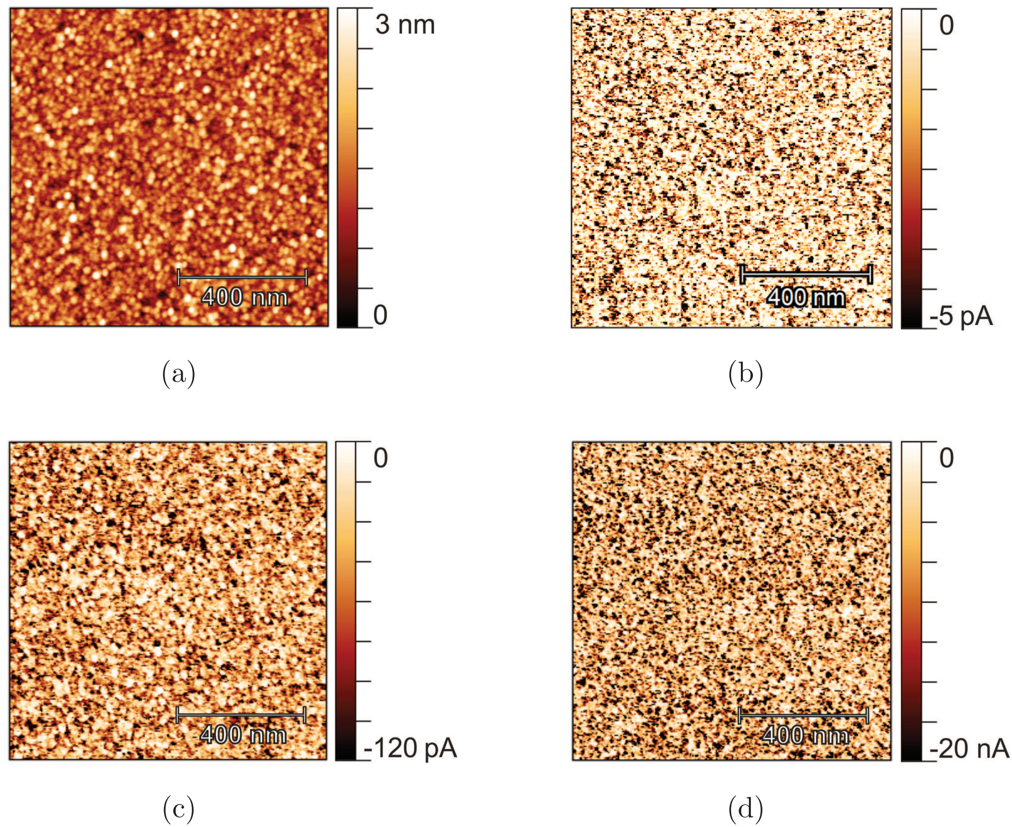

Figure 3.1: *Demonstration of (a) topography measurement and the current signal detected on top of the selective contact in (b) as deposited state and after annealing at (c) 800°C or (d) 850°C. Note especially the changes in the current scale.*

To test whether the detected current signal is connected to the surface of the material or its inner structure, we decided to employ Scalpel C-AFM. As previously mentioned, this new variation of C-AFM enables us to remove a top-most layer of the material

while simultaneously recording a current signal. In our case, the current signal changes significantly already after the removal of the first layer of material from the surface. Transition in the detected current signal between the standard C-AFM and Scalpel C-AFM is captured in (Figure 3.2). A change of quality between the C-AFM (Figure 3.2a) and Scalpel C-AFM (Figure 3.2c) is demonstrated with partially removing scan switching between the two regimes of scanning.

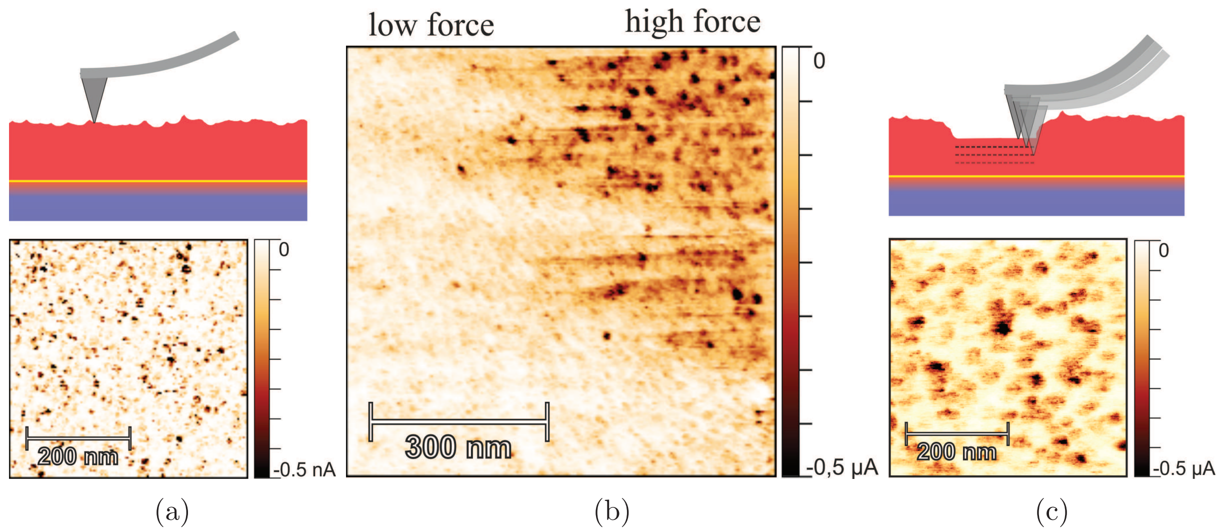

Figure 3.2: *Switching between (a) low-force and (c) high-force C-AFM regimes.*

With this knowledge, we employed scalpel C-AFM to locally analyse the contact-resistivity drop after the high-temperature annealing, known from the selective contact device measurements (Figure 3.3). For these measurements negative sample bias of -1V was applied on the contact structure in as-deposited state (Figure 3.3a) as well as after annealing at 800°C (Figure 3.3b) and 925°C (Figure 3.3c).

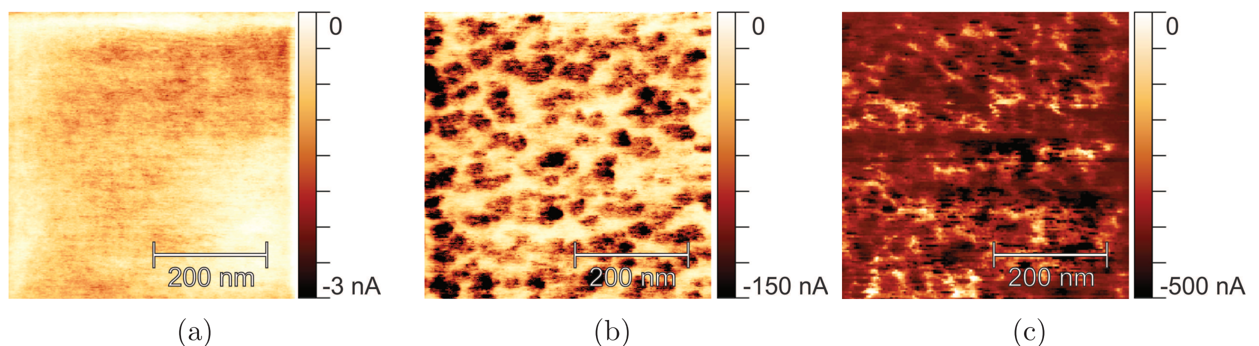

Figure 3.3: *Scalpel C-AFM scans taken on passivating contact structure in as-deposited state (a) and annealed at 800°C (b) and 925°C (c). Scalpel C-AFM scans were taken with negative sample bias of -1V, showing higher detected current as darker spots. Measurements are presented with different current scales to emphasize the changes in the density of high-current areas.*

Sample in as-deposited state showed a homogeneous low current signal across the whole scan, high-current areas started to appear after the annealing at 800°C. The density of these high-current areas increased with the annealing temperature up to the sample annealed at 925°C that showed high currents across the whole scan. This rise in density of high-current areas correlates with a reduction of the contact resistivity reported for elevated annealing temperatures [97], [108]. Thanks to the specific scalpel C-AFM set-up, higher detected current can be directly related to locally decreased "contact" resistivity and therefore to the local increase of the charge-carrier transport.

To link this charge-carrier transport behaviour to the structural changes in the layer stack caused by annealing, we analysed samples with interfacial SiO_x and intrinsic Si buffer layer with HRTEM after annealing at relatively low (800°C, Figure 3.4a) and high temperature (925°, Figure 3.4b). The interfacial SiO_x layer was well pronounced and homogeneous in Figure 3.4a, but annealing at higher temperatures caused a distortion and even local disruptions (marked with arrow in Figure 3.4b). Regarding the sample crystallinity, local Fourier transforms of the micrographs (insets in Figure 3.4a, Figure 3.4b) demonstrated that the a-Si(i) buffer layer crystallized in both cases whereas the crystallinity of the selective SiC_x(p) showed a strong dependence on the annealing temperature. At 800°C, it was still mostly amorphous, whereas after annealing at 925°C it exhibited well pronounced crystalline domains of several nm in size.

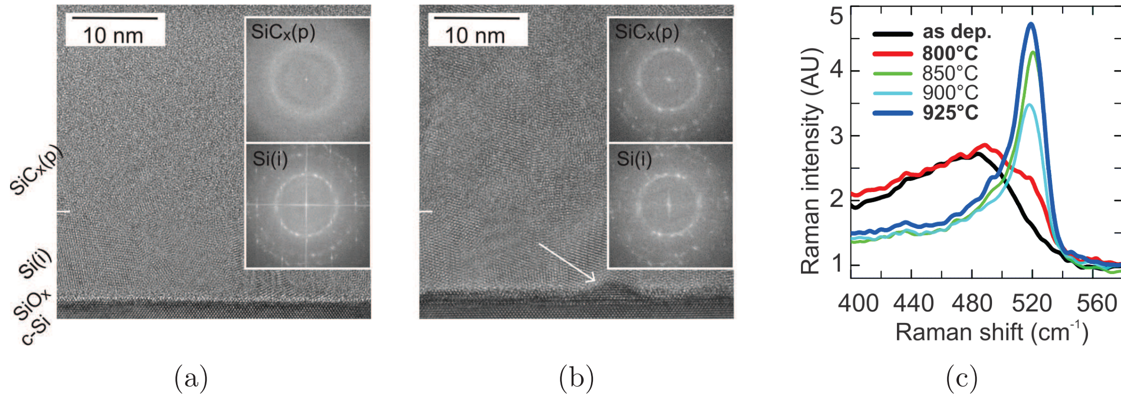

Figure 3.4: *HRTEM micrographs of sample annealed at 800°C (a) and 925 °C (b) together with Fourier transforms computed from it at the position of both the inter–layer bottom and the* SiC_x*(p)—top. Scale bar is the same for (a) and (b). Raman spectra in subfigure (c) show the crystallinity evolution of the samples over the larger scale of annealing temperatures*

To further study the crystallinity changes during annealing, we performed surface-sensitive Raman spectroscopy with 325 nm UV laser on the as-deposited layer and on layers annealed at temperatures up to 925°C (Figure 3.4c). A broad peak at 480 cm^{-1} confirmed the amorphous nature of the as deposited SiC_x(p) (black line). For the sample

annealed at 800°C, the amorphous peak was also prominent, but a small rise around 520 cm^{-1} indicated the existence of nanocrystals in the amorphous matrix. After annealing at temperatures of 850°C and above, the crystalline peak at 520 cm^{-1} became very prominent. However, there was still a slight asymmetry with a shoulder towards lower wavenumbers indicating the persevering presence of an amorphous matrix [127], [128]. These results matched well with the HRTEM micrographs.

Next, we used a scalpel C-AFM to disentangle the influence of the annealing-induced sample crystallinity changes and the interfacial SiO_x distortion on the local charge-current transport. To this end, a sample without interfacial SiO_x (representing a direct Si wafer – Si(i) interface) was compared to a sample with a regular interfacial SiO_x (1.2 nm) and a sample with thermal SiO_x, since increased oxide thickness should translate to lower degree of layer degradation [129]. All samples received the same PEVCD SiC_x(p) layer and they were subsequently annealed at 800 °C, leading to the same crystallinity levels in SiC_x(p) layer. We performed Scalpel C-AFM at sample bias of -1V (Figure 3.5) for the samples with 0 nm (Figure 3.5a), 1.2 nm (Figure 3.5b) and >5 nm-thick (Figure 3.5c) interfacial SiO_x. The density of the high-current areas remained constant between the samples without and with interfacial SiO_x. It was also comparable (albeit less apparent due to the lower overall current intensity) for the sample with thermal SiO_x, even though this layer should be less vulnerable to degradation upon annealing [129]. From these results we can discuss whether the local charge-carrier transport increase is connected to the crystallinity of the SiC_x(p) or the structural degradation of the interfacial SiO_x (pin-holes).

The role of the interfacial SiO_x layer in the charge-carrier transport in selective contacts was widely studied in the past [103], [110], [130], [131], even with use of microscopic methods such as electron-beam induced current (EBIC) [115], [132], [133] or C-AFM [125], [126], [134]. Our experiments (Figure 3.5a and Figure 3.5b) showed that high-current areas in SiC_x(p) were present even in sample with direct c-Si(p) wafer – Si(i) inter-layer interface. Moreover, our HRTEM investigations and results by other research groups [111], [114] suggest that the expected pin-hole density in interfacial SiO_x would be much lower than the density of the high-current areas in Figure 3.5a to Figure 3.5c. These results make any direct connection between the interfacial SiO_x layer pin-holes and detected areas showing increased charge-carrier transport impossible.

Additional observation can be made about the role of the interfacial SiO_x. While the density of the high-current areas did not change for the various interfacial layers, the average overall current did decrease for the thick thermal SiO_x (Figure 3.5c). This can

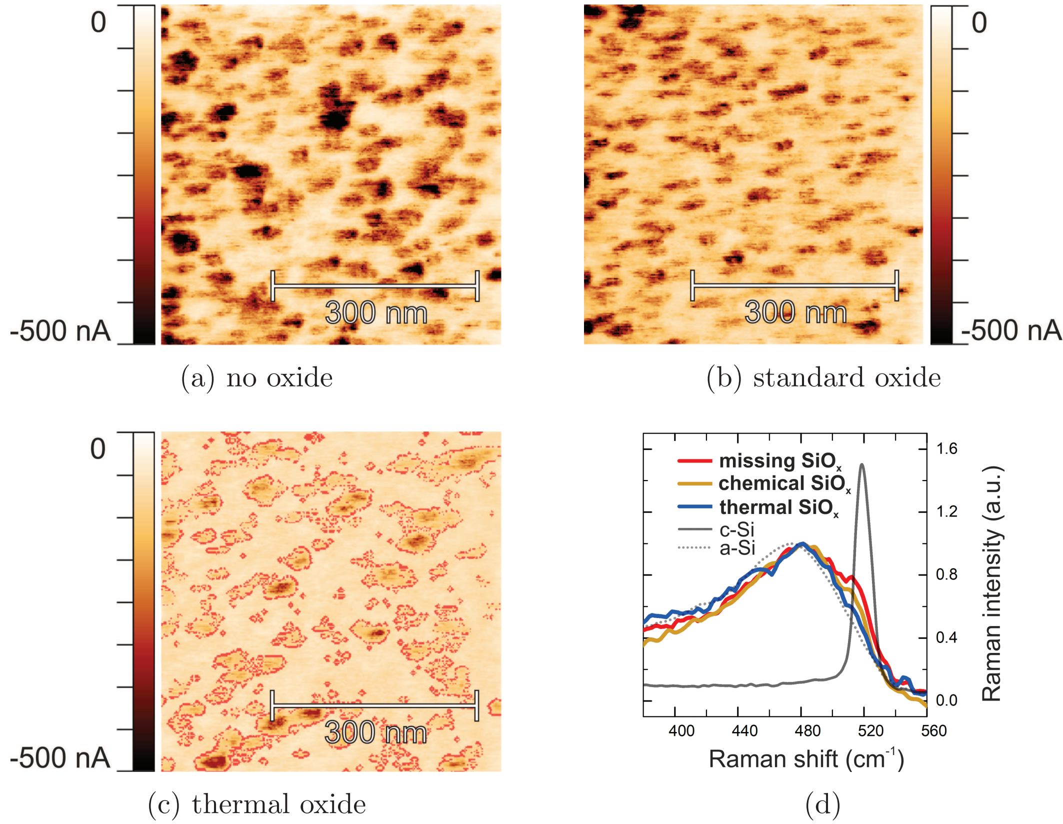

Figure 3.5: *Series of scalpel C-AFM current maps demonstrating the change of the average current going from sample without a SiO_x layer (a), standard 1,2 nm chemical SiO_x buffer layer (b). and a thick (> 5 nm) thermal buffer SiO_x layer (c). Due to the decrease on the over-all average current, high-current areas in subfigure (c) were accented using a red-colored mask. Raman spectroscopy measurements (d) show the crystallinity of all the layers.*

be explained as follows; the magnitude of the average detected current (averaged over the high- and low-current areas) does not only depend on the density of the high-current areas, but is also influenced by thickness and stochiometric structure of the SiO_x layer, presence of the pin-holes etc. In case of the missing interfacial oxide, high-current areas density is the only factor limiting the transport through the selective contact.

While the nature of the interfacial SiO_x differed between the samples presented in Figure 3.5a to Figure 3.5c, their crystallinity measured on the sample surface by Raman spectroscopy (Figure 3.5d) was, as expected, very similar and in accordance with the sample annealed at 800°C presented in Figure 3.4c. The slight drops in the amplitude of the small crystalline peak corresponded with the marginal changes in the densities of the high-current areas apparent between Figure 3.5a-Figure 3.5c. Given the results represented in Figure 3.3 and Figure 3.5 a connection between a locally increased charge-carrier transport and the crystalline domains embedded into an amorphous matrix of low-current "background" can be hypothesized.

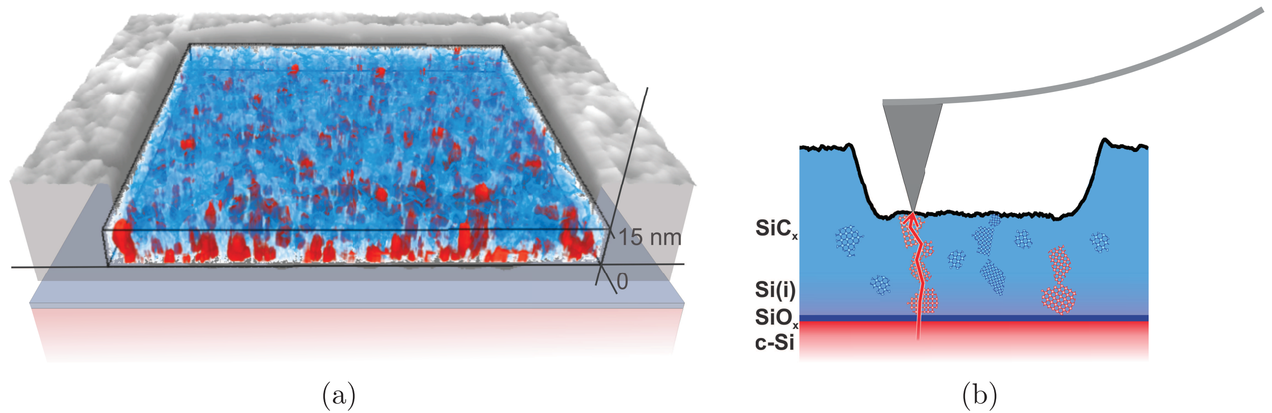

Figure 3.6: *C-AFM tomography visualization of the high-current charge carrier transport channels (red) going through the blue high-resistance amorphous SiC_x matrix (a). Schematic model of the crystalline-grain chain acting as a transport channel for charge carriers upon being contacted by a conductive AFM tip (b).*

To further study the connection between the charge-carrier transport through the SiC_x(p) layer and its crystallinity, we performed C-AFM tomography on the sample annealed at 800°C (Figure 3.6). Our goal was to investigate an evolution of the high-current areas throughout the selective layer. Individual "slices" of the final 3D model are shown in Figure 3.7 going from the surface of the sample (obtained with low-force C-AFM) to almost fully saturated scan 15 nm deep below the surface that was omitted from the final reconstruction for the sake of clarity.

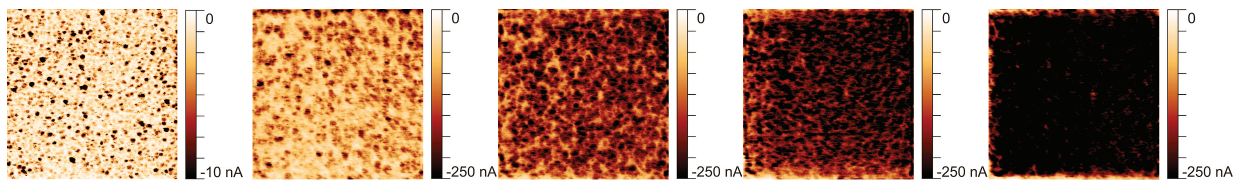

Figure 3.7: *Evolution of the Scalpel C-AFM serving as building blocks for C-AFM Tomography.*

In the tomographic reconstruction of the removed volume, red colour marks the high-current areas whereas blue colour represents the less conductive background characterized by low detected current. Our result revealed vertical conductive channels running from the bottom of the partially crystalized SiC_x(p) up to its surface. Some of these channels propagated through the whole SiC_x(p), some did not reach the sample surface. It is worth reminding that, given the nature of AFM, the apparent size of the channels could be strongly influenced by the physical dimensions of the relatively large diamond-coated conductive tip and the magnitude of the contact force [117].

Considering the inner microcrystalline structure of the SiC_x(p) shown in Figure 3.4

and the relation between the high-current areas and the sample crystallinity, the channels can be interpreted as mostly vertical chains of crystalline grains or grain clusters conductively connected to the bottom Si wafer, rather than continuous conductive volumes present in the matrix, as is schematically visualized in Figure 3.6b. Crystalline grains formed during annealing create, either by direct contact or by percolation, conductive chains that, on the condition that they are in conductive contact with the Si wafer, serve as charge-carrier transport channels through the surrounding amorphous matrix. The density of these transport channels depends on the SiC_x(p) crystallinity. In our case of B-doped SiC_x(p) layer, annealing the contact structure at higher temperature leads to a larger number of the grain clusters able to reach both sides of the contact. To further understand the detailed models of the transport mechanism via percolation through partially crystallized layer we can apply models developed in the past for other systems [135].

3.4 Conclusions

Comparing standard C-AFM with the novel technique of Scalpel C-AFM, we can see the qualitative difference between the two measurements that can be credited to switching from artefact-dominant imaging to series-resistance mode of C-AFM. This switch is enabled by substantial increase in the contact force and subsequent decrease of the tip-sample contact resistance.

Prior to this work, a drop in the contact resistivity of selective contacts upon high-temperature annealing was almost exclusively attributed to the degradation of the interfacial SiO_x. However, scalpel C-AFM revealed the presence of charge-carrier transport channels in the partially crystallized selective (p) layer. Moreover, the density of these channels is not related to the interfacial SiO_x layer properties or its existence, but only to the degree of crystallinity of the doped selective layer as was shown by performing measurements on the samples without any SiO_x layer.

We propose that the local current transport through the selective contact structure is facilitated via channels extending from the Si wafer interface that are formed by chains of crystalline grains. The over-all current transported through the full selective contact is therefore a convolution of two effects – transport through the interfacial SiO_x layer and conductive channels formed in the SiC_x(p) layer. This theory is supported by HRTEM and Raman spectroscopy measurements as well as results of the scalpel C-AFM experiments. Conductive channels were visualized in 3D using C-AFM tomography for the first time, underlining the importance of the crystallinity of the doped selective layer in the local transport of charge-carriers in selective contact structures.

Chapter 4

C-AFM Tomography - Lessons Learned

As we seen in the previous chapter, utilizing C-AFM tomography can help us to gain unique information from the sample volume, making it a very useful tool to map the charge transport throughout the complicated multi-layered structures of the modern photovoltaic devices, among other applications. However, it is a technique demanding equally on the equipment and an operator. In terms of equipment, high contact forces add an additional condition on the choice of the tips, requiring conductive and sturdy ones at the same time. This strongly limits the choice to basically only highly doped full-diamond or diamond-coated tips. Manufacturers like, for example, Belgian IMEC or British Adama offer this kind of tips in several variations, although the standard full-diamond tips with the tip curve radius of several tens of nanometres are the work horse of the C-AFM tomography. As for an operator, they must fortify themselves with patience to withstand many unsuccessful tries, since the whole series of Scalpel C-AFM scans can be ruined by a single mess-up. To limit these troubles to the minimum, we will offer a short to-do list for C-AFM tomography at the end of this chapter. However, we are not aiming to create a definitive C-AFM tomography guide. A reader interested in additional aspects of this fascinating technique can find them in the ever-increasing number of relevant papers [120], [123].

4.1 Setpoint vs Contact Force

During the contact measurement, which, as the general rule, is the best candidate for obtaining any reasonable electrical data, the constant force is maintained through maintaining constant cantilever deflection. Deflection is corrected by applying bias to the piezo element to achieve pre-set value of so-called Contact Setpoint parameter. Deflection of the cantilever (Setpoint value) is directly detected by the optical lever and photodiode and is described as an arbitrary number in volts by most of the AFM softwares. While the deflection of the cantilever can be in theory directly translated into the contact force by an easy formula, one must be aware of the strict limitations and conditions of such a step. Many AFM manufacturers include a feature of automatic recalculation of the arbitrary setpoint number into a force in Newton (nN or µN mostly), unfortunately, this figure is often as arbitrary as the setpoint number and more confusing most of the time.

The formula used to calculate the force from the deflection setpoint is, as we already stated, simple:

$$F = -kx \tag{4.1}$$

where **F** stands for the contact force, **k** is the spring constant of the cantilever and **x** is the cantilever deflection, directly obtainable from the photodetector.

With contact resistance changing drastically with even small changes in the contact force at certain ranges, even small fluctuations in force can be very impactful on the current measurement. Therefore, it is imperative for the value of **F** to be calculated and kept as accurately as possible. Unfortunately, there are several more or less hidden problems in the above-mentioned formula coming mostly from the technological limitations of AFM. Many users presume the microscope is “taking care” of these difficulties and while the effects of these complications can be easily mitigated using software recalculation in case of topography measurement, the influence on the current signal is much harder to fix this way, i.e., ex post.

4.1.1 Spring constant inconsistences

While we will mostly discuss the problems of the cantilever deflection detection, spring constant of the cantilever is not to be ignored either. A manufacturer-stated spring constant of the cantilevers is an average value over the batch of the tips. Paired with high

setpoint values, the errors caused by the spring constant deviation can be significant. Under extreme conditions, however, and removing material with the tip during the SSRM measurements for example can be considered extreme, the spring constant of the cantilever can change during the measurement, by deformation caused by collision with the sample, destruction of the metal coating or by the tip's adaptation to measurement conditions like humidity and temperature. Negative impact of these phenomena can be, to some degree, mitigated by performing a calibration procedure with every tip used.

Spring constant calibration requires a vast analytical knowledge of the tip shape and size, its hydrodynamics, resonance frequency and many other parameters. But we hesitantly can, for the sake of simplicity, accept the fact, that it is theoretically possible to derive a correct value of the spring constant for each individual AFM tip (although it is much more difficult than most of the AFM manufacturers make it out to be). After all, most of the microscopes on the market state to have this feature readily available.

4.1.2 Setpoint drift

The other element of the equation (4.1), the cantilever deflection, is being directly measured by the photodiode. Unfortunately, keeping it constant does not always translate into constant setpoint (and therefore the contact force). The reason for this lies in various creeps that occur during the measurement. When the laser position changes due to the thermal expansion of the reflective metallic coating, for example, controller of the microscope interprets this change as a change in setpoint and adjusts the piezo accordingly. In topography measurement, similar processes may lead to, for example, an artefact manifesting as an apparent slope of the measured surface in the direction of slow axis. Such a slope is very simple to compensate for in any processing software. However, these small changes in contact force can lead, in certain ranges, to significant changes in measured current, where the software post-processing is not desirable.

Apart from the suggested thermal expansion of the reflective coating, many other small things probably play role in the mentioned creep, such as piezo drift, thermal expansion of the whole cantilever (changing the length of the arm), changes caused by fluctuations in humidity etc. These effects can be hardly noticeable and inconsequential in most of the AFM applications, but it is always advisable to keep their existence in mind.

It is worth mentioning that microscope close-loop feedback is supposed to mitigate

the creep that we are discussing here, but its abilities to do so are and always will be limited by the computational power and speed of the controller.

The main reason for this detailed scrutiny of the spontaneous setpoint changes is the strong dependence of the material removal rate on the setpoint value. The fact that we can never fully control measurement setpoint for most of the commercially available microscopes means that we must, at least for now, accept the inevitable variance in C-AFM tomography results.

4.2 Material removal rate

As insinuated above, removal rate strongly depends on several parameters. These can be broadly divided into two groups, effects of the material properties and the tip/microscope-related influences. The parameter expected to play the biggest role is the material stiffness and density, simply put: "how hard is the material". It is no surprise that one can easily remove tens of nanometres of soft and yielding substrate, like perovskite thin films for example, using the same force that would hardly make a mark on the crystalline silicon wafer. Apart from the stiffness, experiments suggest that sample topography also plays a role in the material removal rate.

While the mechanical properties are usually homogeneous throughout the area of the measurement, we have observed uneven removal rates within individual scalpel C-AFM scans almost without exception across all our measurements. To explain these local changes, we turn to the other group of effects, the tip/microscope ones. As mentioned above, measurement creep may move the tip slowly up or down relative to the sample while nominally maintaining constant setpoint. Usually this is compensated in-real-time by the microscope software, but that is not relevant in relation with material removal, since it directly changes the removal rate during the scan.

Although it is not difficult to remove large volumes for materials using a very high contact force, the heart of the matter with Scalpel C-AFM lies in ability to reliably and repeatably remove layers of material of controlled thickness (or rather thinness). For this reason, the contact force during the measurement is often kept at the very minimum of material-removing regime. Umberto Celano, the founding father of Scalpel C-AFM, describes switching between so called "sliding" and "ploughing and sliding" regimes at a very finely defined threshold, a contact forced labelled as $\mathbf{F}_{TH}$ [116]. For optimal results,

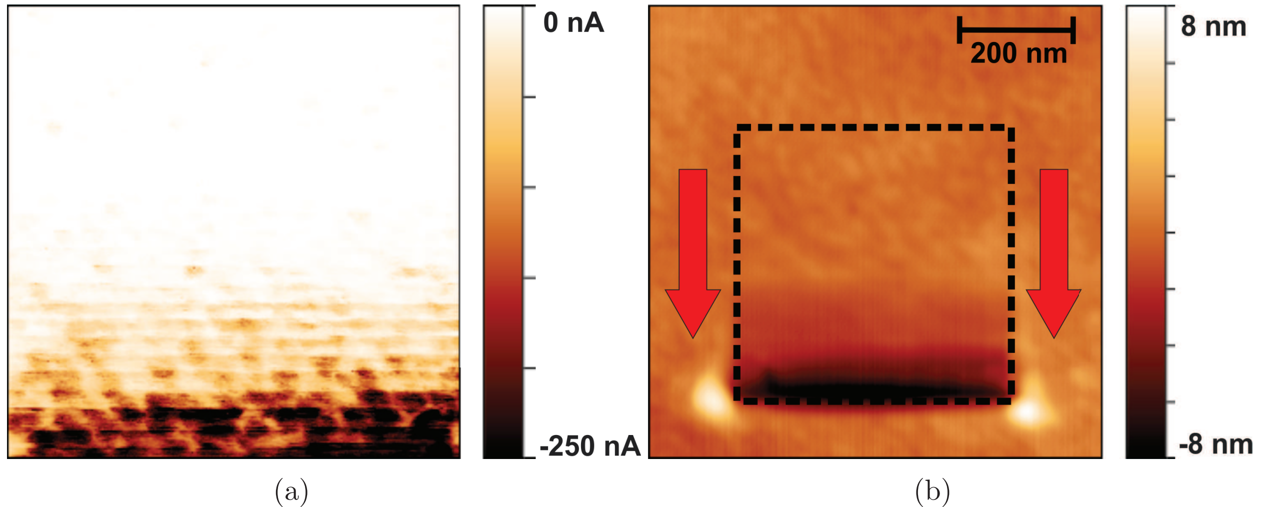

(a) (b)

Figure 4.1: *Demonstration of process of finding the threshold force between "sliding" and "ploughing and sliding" regime. Setpoint of the first pass was gradually increased with detected current increasing accordingly, as depicted in (a). Second pass in normal force regime (b) shows the material removal rate rapidly increasing towards the bottom of the scan*

one must strive to keep the contact force only slightly above the F_{TH} throughout the scan. Considering the previously mentioned inherit instabilities in contact force settings, this can be a challenging task. Another factor that comes to play is sample topography – we have observed switching between the two described regimes in the course of the single scan due to the relatively large skew of the sample surface for example. In other cases, tip remained in the sliding regime on the flat silicon wafer for relatively high contact forces until it suddenly breached the surface and began to etch the material with a quickly increasing rate. We tentatively ascribe this kind of behaviour to sudden increase in contact pressure due to the changes in the contact area induced by the inhomogeneous sample geometry – it has been proven that small changes in the mechanical contact can induce significant variations in the contact force [80].

4.3 Single-pass vs Two-pass configuration

While the uniform removal of the material might be the technically most difficult part of the C-AFM tomography, it is certainly not the most discussed one. While some of the recommended parameter's values differ from author to author, more controversial topic is the data collecting process. Some operators collect the data during the material removal scan, others advise to perform two consecutive measurements, one with high lateral force to remove sufficient amount of material (so-called "etching step") and a second one to collect the data. While pros and cons can be found for both approaches,

we believe that this decision is not only a matter of taste, but ultimately depends on the measured material, experiment conditions and desired outcome.

The the two-pass method eliminates a problem with concurrent material deposition on the sides for the tip that can affect the data collection in one or both scan directions, but it also loses the added advantage of high contact force that decreases the effective tip-sample resistance. Additional complications for this approach arise in case of measurements on silicon samples, where the misplaced crystalline silicon creates layer of amorphous oxide-rich material on top of the Scalpel C-AFM trench, completely masking all the conductive signal for any consecutive measurements apart from another round of high-force Scalpel C-AFM that allows the tip to penetrate and remove the isolating layer. This behaviour was both experimentally observed in our lab and reported by other authors [120], [136]. On the other hand, when the material under investigation does not exhibit this hindering behaviour and the measurement is performed in controlled atmosphere that can in itself decrease the parasitic tip-sample resistance, two-pass method offers more straight-forward data interpretation, since it omits a complicated discussion on influence of the simultaneous material removal on the data collection ability of the tip during the measurement [122].

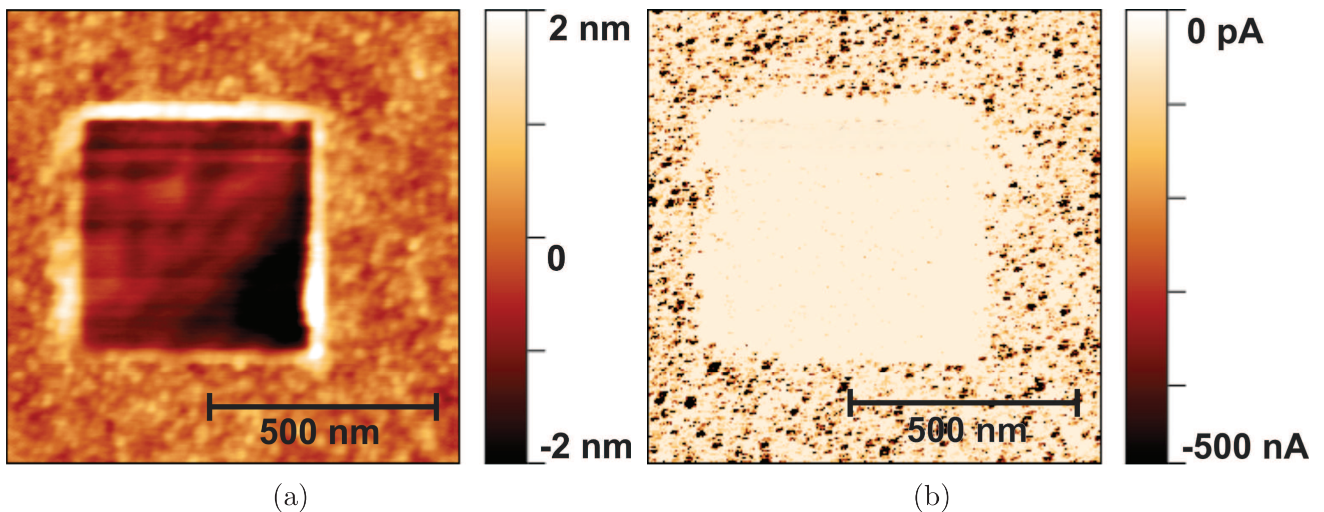

(a) (b)

Figure 4.2: *Standart C-AFM after single Scalpel AFM scan reveal (a) uneven removal rate, most probably caused by non-flat surface of the sample at the position of the dig and (b) loss of the surface current signal that can be credited to the re-deposition of amorphous silicon at the dig site.*

4.4 What's important to do before the scalpel C-AFM measurement:

- make sure the tip is conductive, preferably non-coated, with high-enough **k**
- mount the tip and make sure the laser is well located in a stable position close to the tip's measuring end – symmetrical laser position is even more important for scalpel C-AFM measurement, as we aim to achieve stable and homogeneous material removal across the whole scan area
- cleaning the previously used tip by few scans on the stiff hard sample (e.g. Si wafer) can improve the quality of the result (or destroy the tip irrefutably), polarizing tip bias from -10 V to 10 V and back few times in a quick succession was reported to help with the tip cleaning, although it can apparently also lead to a quick tip destruction – it should therefore be only used as a last resort
- make sure the sample is well levelled – to ensure this, quickly scan an area larger than the one you will be scratching away without any "live" software levelling. The area should be flat preferably in both the fast and slow axis direction (small skew within 1-2 nm is usually fine). The pre-scan over the area can also serve as a quick clean-up of the digging site as well as preliminary current measurement, if necessary.
- engage the scan with desired parameters (size, # of lines etc.) with a small setpoint that doesn't remove the sample (e.g. for the shortest IMEC full-diamond tips and silicon sample a setpoint of 0,3 V is sufficient to maintain a good contact)
- set the scan to start from the top and increase the setpoint to the desired value at the last possible line to avoid double-scanning of the top-most lines (e.g. for the shortest IMEC full-diamond tips on poly-silicon sample a goal setpoint value should be above 1 V).
- when performing a series of scalpel C-AFM scans on the same place, avoid using "scan in one direction only" function. While the scans taken during the both-directional measurement are often unusable in one of the directions (probably due to the uneven deposition of removed material on the tip), this method allows for gradual material removal across the whole scanned area whereas "scan in one direction" feature leads to the creation of the distinctive diagonal trench making all the further scans after the first one useless (the tip does not disengage at the end of the scan and moves back to the starting position with high contact force still applied,

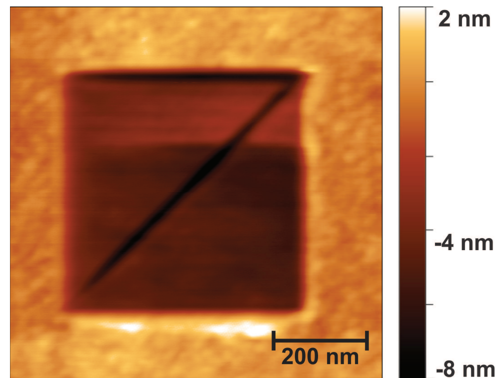

Figure 4.3: *Typical diagonal trench appearing after using "scan in one direction" feature with ICON AFM. This artefacts is formed by the movement of still engaged tip from the bottom of one scan to the beginning of the next one*

see Figure 4.3). This can be also avoided by lowering the setpoint after each scan to the non-removal force, starting the measurement from the top and increasing the setpoint again.

- when performing a series of scalpel C-AFM scans on the same place, uniform material removal can be hurdled by the redeposition of the material on the edges of the scratched area. For cleaner results, one can slowly decrease the scratched area size with each subsequent scan. This however requires baby-sitting the measurement and lowering the setpoint after each scan to the non-removal force, decreasing the scan size, starting the measurement from the top and increasing the setpoint again.

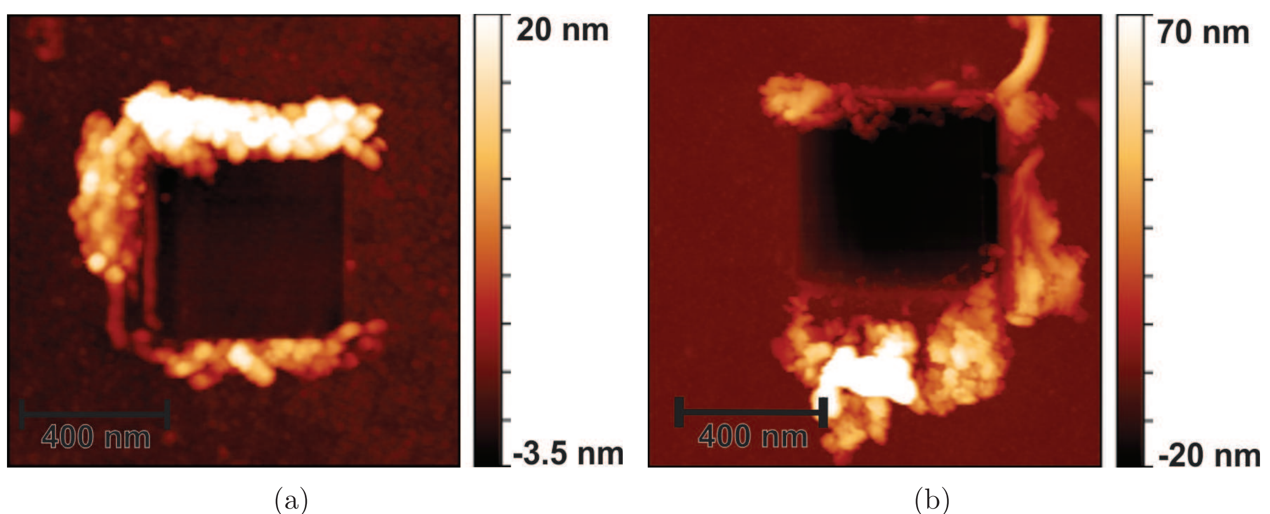

Figure 4.4: *Visualisation of two different cases of material re-deposition from two separate Scalpel C-AFM experiments. As we can see, with the depth of the dig increasing from (a) 3,5 nm to (b) 20 nm the amount of re-deposited silicon increases accordingly, making it easier for the misplaced material to mess up the following experiments.*

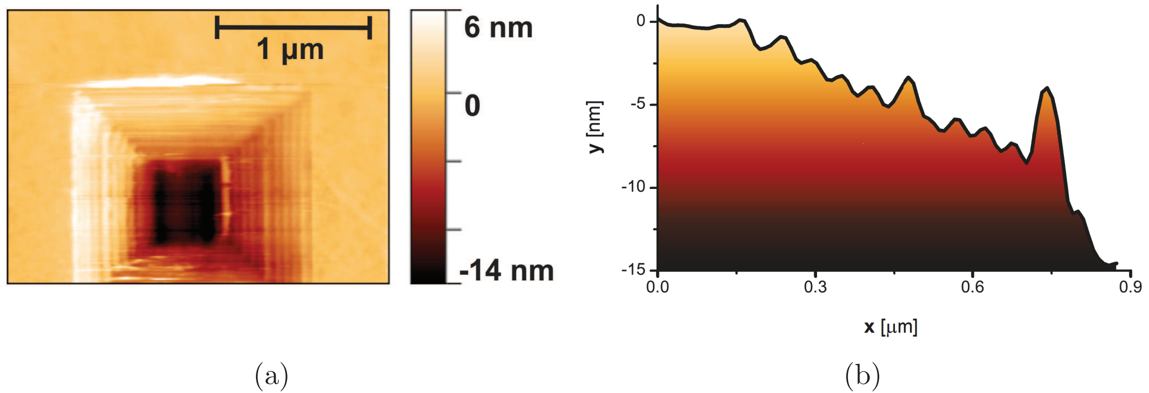

(a) (b)

Figure 4.5: *Demonstration of the possible progression of the C-AFM Tomography experiment, using gradual decrease of the scan size for subsequent Scalpel C-AFM. This standard topography measurement shows (a) final shape of the 12 subsequent scans and (b) the height profile of the resulting dig.*

- material removing scan does not have to be slow or detailed. While other authors recommend higher line-count when performing scalpel C-AFM [123], 256 lines for a 500 nm - 1 µm scan size is sufficient for (poly)crystalline Si samples. Faster scans are generally more convenient since the material deposition on the tip is extremely difficult to predict and the tip's conductivity can change at any point during any measurement. We have found that the "quantity over quality" approach seems to lead to the overall best yield of usable results in case of scalpel C-AFM and C-AFM tomography. However, we do not rule out that the settings for this technique can be perfected to the point where the usable vs unusable results ratio is sufficient to slow down the scan speed and increase the line number in order to achieve higher-quality results.

- Since the removal rate of the measurement differs strongly based not only on the local mechanical properties of the sample but also the tip stiffness and over-all shape, the only way to fine-tune the removal rate for each individual measurement is to perform a test run with the general settings and adjusting the setpoint, measurement speed and number of lines accordingly to achieve the desired material removal-rate. It is however important to understand that, from our experience, the removal rate is not completely homogeneous and may change from scan to scan based for example on the material deposition on the tip.

- after the experiment is done, it is advisable to perform a large (e.g. 4x larger) overview scan of the excavated area. This scan will not only show you achieved depth of the C-AFM tomography picture (and therefore the average material removal rate per scan), but one can also use it to assess the amount of debris deposited on the tip for example.

- Since the scalpel C-AFM scan is based on a contact AFM measurement, asymetrical mechanical properties of the cantilever can play a significant tole. From our experience, the scanning angle does not influence the quality of scalpel C-AFM in any significant way. However, scanning angle of 90° is probably still preferable, since the tip manifests more symmetrical behaviour in torsion while switching from trace to retrace direction that when bending along its longitudinal axis.

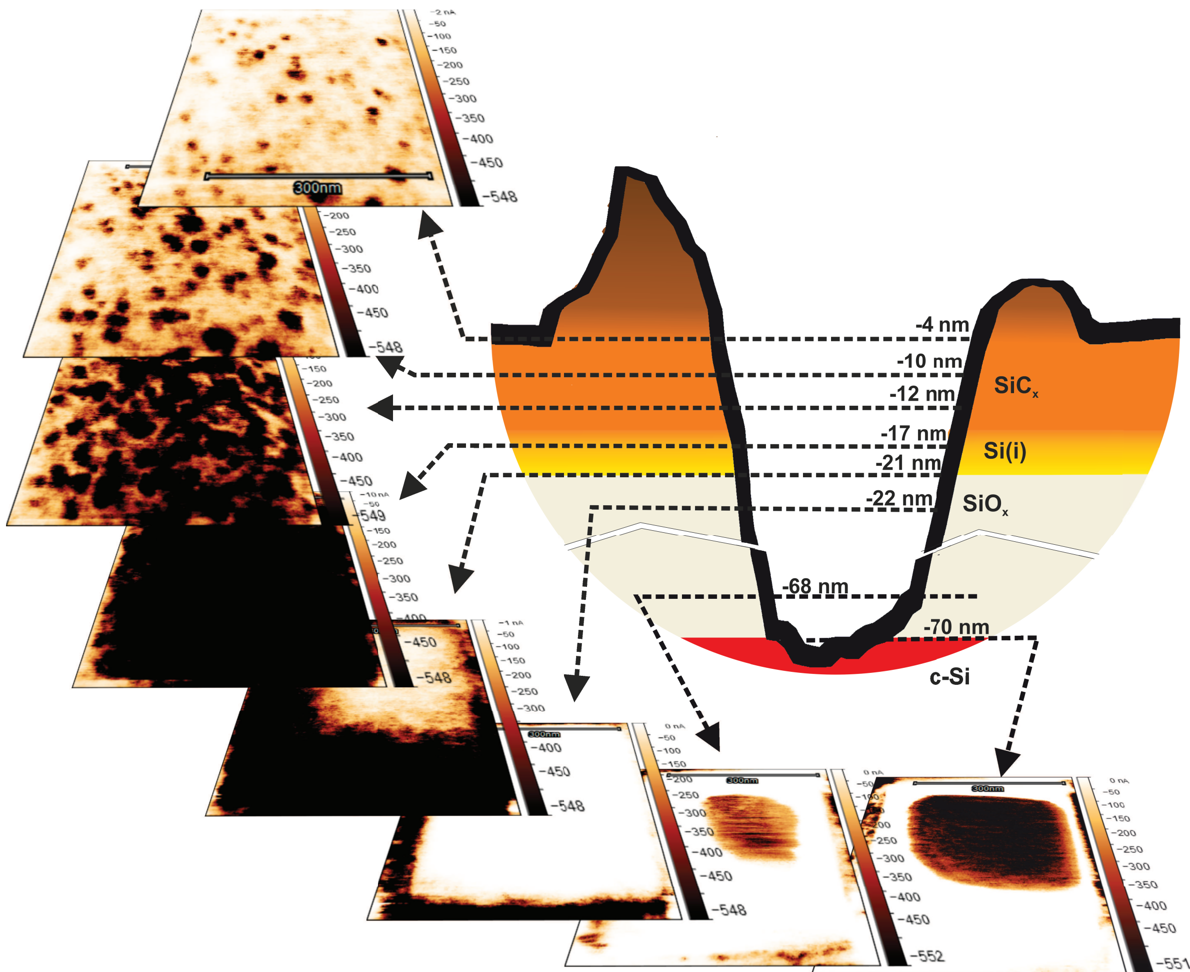

Figure 4.6: *Final example of the C-AFM Tomography not published before - While the basic architecture of the sample is very similar to that presented in chapter 3, the interfacial SiO_x layer in this sample is replaced with thick (> 40 nm) thermal SiO_x. This is also very apparent from the individual Scalpel C-AFM slices obtained from depth from ∼20 to ∼70 nm that show extremelly low current signal of practically isolating oxide in contrast to conductive channels above and homogeneous high-current signal from doped Si wafer at the bottom of the sample.*

Chapter 5

Conclusions and Outlook

In the first chapter, I have defined following goals for my dissertation thesis:

To demonstrate the viability of existing SPM techniques for solar cells characterization

The viability of variousSPM techniques was proven not only by the concise study of different methods presented in Chapter 1, but especially by the Chapter 2, that offered a large number of mostly published (see the list of publications) or presented current-detecting AFM experiments performed on the photovoltaic materials and solar cells.

To increase traceability, repeatability and reproducibility of electrical SPM techniques

While it might seem that my work offers more problems then solutions in regard to current-detecting AFM, the only way to make electrical SPM techniques better is to study them and try to fully understand them. I tried to dutifully address and examine some of the biggest shortcomings of these methods. My findings regarding the nature of tip-sample contact presented in Chapter 2 and Chapter 4 bring us closer to further understanding of the current flow through the complicated system of C-AFM and also directly led to the Scalpel C-AFM and C-AFM Tomography experiments being pioneered on the silicon solar cells in our lab.

To develop a new solar cell characterization method based on SPM techniques

Presented Scalpel C-AFM and C-AFM Tomography was, at the time when I carried out the first experiments in our lab, a cutting-edge new technique, never used on the solar cell before. This has changed since, but the results presented here in Chapter 3 and Chapter 4 represent, to my knowledge, the only research of its kind on Si-based solar

cells. Implementing this technique for various number and kinds of samples might unlock new possibilities in mapping the charge carrier transport etc. Additionally, Chapter 4 has been written to serve as a brief manual or check lisk for a possible AFM operator in need of Scalpel C-AFM of C-AFM Tomography measurement. To this end, it will be hopefully used in our laboratory in the future.

Outlook

Current-detecting AFM techniques are continuously perfected, mostly due to the pressure on the microscope manufacturers to sell new machines with new modes interesting for researchers and industry alike. Hopefully one day in the future all the findings and data from tip-sample contact behaviour and sample geometry effects could be utilized to introduce a real-time software compensation of said artifacts. This way, standard low-force C-AFM could offer as reliable results as the SSRM technique even for casual operators in industry. To achieve this ambitious goal, we plan to continue with our experiments in this field, already working on new experiments involving carefully designed geometrical samples and tips of different shapes and materials.

Scalpel C-AFM is quickly gaining a spotlight on the current-detecting AFM stage. More and more groups are trying to utilize this technique in their research of solar cells of various kinds. Deciphering all its sensitive parameters and achieving high repeatability and reproducibility should be the highest priority for the community right now.

Since the growing abundance of the solar cells is inevitable in the future, so is the need to characterize them. This thesis proves that the AFM and particularly the current-detecting kind is an important and useful tool for solar cell characterization right now and it will become even more significant in the future, given the time and care it deserves. To fully realize their potential, current-detecting AFM techniques still have a long way to go. Hopefully, with this thesis I can contribute to this challenging yet necessary task. As I write these lines, horrible events on our doorsteps show us once again the inevitability of the great shift toward the renewable energy sources and solar power is ready for the task, if we are. The motivation to use, build and study solar cells was never more pressing and more present than nowadays.

Seznam literatury související s dizertační prací

články (s impaktem)

- **M. Hývl**, G. Nogay, P. Loper, F.-J. Haug, Q. Jeangros, A. Fejfar, C. Ballif, and M. Ledinský, "Nanoscale study of the hole-selective passivating contacts with high thermal budget using c-afm tomography", en, *ACS Applied Materials Interfaces*, vol. 13, no. 8, pp. 9994–10 000, Mar. 3, 2021, ISSN: 1944-8244, 1944-8252. DOI: 10.1021/acsami.0c21282.

- M. Müller*, **M. Hývl***, M. Kratzer, C. Teichert, S. Misra, M. Foldyna, L. Yu, P. Roca i Cabarrocas, *et al.*, "Investigating inhomogeneous electronic properties of radial junction solar cells using correlative microscopy", *Japanese Journal of Applied Physics*, vol. 54, no. 8S1, 08KA08, Aug. 1, 2015, ISSN: 0021-4922, 1347-4065. DOI: 10.7567/JJAP.54.08KA08.*

  **First two authors contributed equally to this work*

- A. Fejfar, **M. Hývl**, A. Vetushka, P. Pikna, Z. Hájková, M. Ledinský, J. Kočka, P. Klapetek, *et al.*, "Correlative microscopy of radial junction nanowire solar cells using nanoindent position markers", *Solar Energy Materials and Solar Cells*, EMRS 2014 Spring Meeting – Advanced materials and characterization techniques for solar cells II, vol. 135, pp. 106–112, Apr. 1, 2015, ISSN: 0927-0248. DOI: 10.1016/j.solmat.2014.10.027.

- G. Köppel, V. Preidel, S. Mangold, E. Rudigier-Voigt, **M. Hývl**, A. Fejfar, B. Rech, and C. Becker, "Nanoimprint-textured Glass Superstrates for Light Trapping in Crystalline Silicon thin-film Solar Cells", en, *Energy Procedia*, vol. 84, pp. 118–126, Dec. 2015, ISSN: 18766102. DOI: 10.1016/j.egypro.2015.12.304. [Online]. Available: http://linkinghub.elsevier.com/retrieve/pii/S1876610215029690 (visited on 03/21/2017).

- J. K. Rath, C. Prastani, D. E. Nanu, M. Nanu, R. E. I. Schropp, A. Vetushka, **M. Hývl**, and A. Fejfar, "Fabrication of SnS quantum dots for solar-cell applications: Issues of capping and doping", en, *physica status solidi (b)*, vol. 251, no. 7, 2014, ISSN: 1521-3951. DOI: 10.1002/pssb.201350377. [Online]. Available: https://onlinelibrary.wiley.com/doi/abs/10.1002/pssb.201350377 (visited on 03/15/2022).

- A. Fejfar, **M. Hývl**, M. Ledinský, A. Vetushka, J. Stuchlík, J. Kočka, S. Misra, B. O'Donnell, *et al.*, "Microscopic measurements of variations in local (photo)electronic properties in nanostructured solar cells", en, *Solar Energy Materials and Solar Cells*, Thin-film Photovoltaic Solar Cells, vol. 119, pp. 228–234, Dec. 2013, ISSN: 0927-0248. DOI: `10.1016/j.solmat.2013.07.042`. [Online]. Available: `https://www.sciencedirect.com/science/article/pii/S0927024813003887` (visited on 03/15/2022).

Konference

- **M. Hývl**, G. Nogay, P. Loper, F.-J. Haug, Q. Jeangros, A. Fejfar, Ch. Ballif, and M. Ledinský, *Mapping the Transport Paths in Silicon Passivating Contacts with Conductive AFM Tomography*, English, oral presentation, E-MRS Spring Meeting 2021, online, June 2021.

- **M. Hývl**, G. Nogay, P. Loper, A. Ingenito, M. Ledinský, Ch. Ballif, and A. Fejfar, *Nanoscale Study of the Hole-selective Passivating Contacts for High-Efficiency Silicon Solar Cells Using C-AFM Tomography*, English, oral presentation & poster*, ICANS28, Palaiseau, France, August 2019.

  **Awarded the Best Poster Award*

- **M. Hývl**, M. Ledinský, and A. Fejfar, *Contact Force in C-AFM – Toward the Quantitative Results in Low-Force Regime*, English, oral presentation, SPM Workshop 2019, Lednice, Czech republic, March 2019.

- **M. Hývl**, M. Müller, M. Foldyna, P. R. i Cabarrocas, and A. Fejfar, *Application of Microscopy Methods for Characterization of Silicon Nanostructures*, English, oral presentation, ICN-T 2018, Brno, Czech republic, July 2018.

- **M. Hývl**, M. Müller, S. Misra, M. Foldyna, P. R. i Cabarrocas, and A. Fejfar, *Investigation of shunt propagation in radial junction solar cells with C-AFM*, English, oral presentation, SPM Workshop 2017, Lednice, Czech republic, March 2017.

- **M. Hývl**, M. Müller, M. Foldyna, P. R. i Cabarrocas, and A. Fejfar, *Application of Microscopy Methods for Characterization of Silicon Nanostructures*, English, oral presentation*, ACEEES forum 2017, Tenerife, Spain, December 2017.

  **Awarded the Best Presentation Award*

- **M. Hývl**, M. Müller, A. Vetuško, A. Fejfar, S. Misra, and P. R. i Cabarrocas, *Correlative microscopy on radial junction solar cells based on silicon nanowires*, English, Poster, Microscopy 2016, CSMS, Lednice, Czech republic, March 2016.

- **M. Hývl**, M. Müller, A. Vetuško, M. Ledinský, S. Misra, M. Foldyna, L. Yu, P. R. i Cabarrocas, *et al.*, *Correlative Microscopy on Radial Junction Solar Cells Based on Silicon Nanowires*, English, oral presentation, ACEEES forum 2015, Ka'anapali, Hawaii, USA, May 2015.

seznam literatury nesouvisející s dizertační prací

články (s impaktem)

- **M. Hývl**, M. Müller, T.-H. Stuchlíková, J. Stuchlík, M. Šilhavík, J. Kočka, A. Fejfar, and J. Červenka, "Nucleation and growth of metal-catalyzed silicon nanowires under plasma", en, *Nanotechnology*, vol. 31, no. 22, p. 225 601, Mar. 2020, publisher: IOP Publishing, ISSN: 0957-4484. DOI: `10.1088/1361-6528/ab76ef`.

- J. Stránská-Matějová, A. Hospodková, T. Košutová, T. Hubáček, **M. Hývl**, and V. Holy, "V-pits formation in InGaN/GaN: Influence of threading dislocations and indium content", *Journal of Physics D: Applied Physics*, 2022. [Online]. Available: `http://iopscience.iop.org/article/10.1088/1361-6463/ac5c1a`.

- A. Hospodková, T. Hubáček, J. Oswald, J. Pangrác, K. Kuldová, **M. Hývl**, F. Dominec, G. Ledoux, *et al.*, "InGaN/GaN Structures: Effect of the Quantum Well Number on the Cathodoluminescent Properties", en, *physica status solidi (b)*, vol. 255, no. 5, p. 1 700 464, 2018, _eprint: https://onlinelibrary.wiley.com/doi/pdf/10.1002/pssb ISSN: 1521-3951. DOI: `10.1002/pssb.201700464`. [Online]. Available: `https://onlinelibrary.wiley.com/doi/abs/10.1002/pssb.201700464` (visited on 03/15/2022).

články (s review)

- T. Martínek, J. Kudělka, M. Navrátil, V. Křesálek, A. Fejfar, **M. Hývl**, and J. Sobota, “Nanoscale characterization of ultra-thin tungsten films deposited by radio-frequency magnetron sputtering”, in *2015 IEEE 15th International Conference on Nanotechnology (IEEE-NANO)*, Jul. 2015, pp. 510–513. DOI: 10.1109/NANO.2015.7388651.

Bibliography

[1] H. Ziar, P. Manganiello, O. Isabella, and M. Zeman, "Photovoltatronics: Intelligent pv-based devices for energy and information applications", en, *Energy Environmental Science*, vol. 14, no. 1, pp. 106–126, 2021, publisher: Royal Society of Chemistry. DOI: 10.1039/D0EE02491K.

[2] C. Kost, *Study: Levelized cost of electricity - renewable energy technologies - fraunhofer ise*, en, [Online; accessed 2021-12-16]. [Online]. Available: https://www.ise.fraunhofer.de/en/publications/studies/cost-of-electricity.html.

[3] A. H. M. Smets, K. Jäger, O. Isabella, R. v. Swaaij, and M. Zeman, *Solar energy: the physics and engineering of photovoltaic conversion, technologies and systems*, eng. Cambridge, England: UIT Cambridge, 2016, ISBN: 978-1-906860-32-5.

[4] K. L. Chopra, P. D. Paulson, and V. Dutta, "Thin-film solar cells: An overview", en, *Progress in Photovoltaics: Research and Applications*, vol. 12, no. 2-3, pp. 69–92, 2004, _eprint: https://onlinelibrary.wiley.com/doi/pdf/10.1002/pip.541, ISSN: 1099-159X. DOI: 10.1002/pip.541. [Online]. Available: https://onlinelibrary.wiley.com/doi/abs/10.1002/pip.541 (visited on 03/08/2022).

[5] A. Romeo and E. Artegiani, "CdTe-Based Thin Film Solar Cells: Past, Present and Future", en, *Energies*, vol. 14, no. 6, p. 1684, Jan. 2021, Number: 6 Publisher: Multidisciplinary Digital Publishing Institute, ISSN: 1996-1073. DOI: 10.3390/en14061684. [Online]. Available: https://www.mdpi.com/1996-1073/14/6/1684 (visited on 03/11/2022).

[6] G. Regmi, A. Ashok, P. Chawla, P. Semalti, S. Velumani, S. N. Sharma, and H. Castaneda, "Perspectives of chalcopyrite-based CIGSe thin-film solar cell: A review", en, *Journal of Materials Science: Materials in Electronics*, vol. 31, no. 10, pp. 7286–7314, May 2020, ISSN: 1573-482X. DOI: 10.1007/s10854-020-03338-2. [Online]. Available: https://doi.org/10.1007/s10854-020-03338-2 (visited on 03/11/2022).

[7] E. T. Efaz, M. M. Rhaman, S. A. Imam, K. L. Bashar, F. Kabir, M. E. Mourtaza, S. N. Sakib, and F. A. Mozahid, "A review of primary technologies of thin-film solar cells", en, *Engineering Research Express*, vol. 3, no. 3, p. 032 001, Sep. 2021, Publisher: IOP Publishing, ISSN: 2631-8695. DOI: 10.1088/2631-8695/ac2353. [Online]. Available: https://doi.org/10.1088/2631-8695/ac2353 (visited on 03/11/2022).

[8] L. Hirst, "Ever thinner high-efficiency cells", en, *Nature Energy*, vol. 4, no. 9, pp. 726–727, Sep. 2019, Number: 9 Publisher: Nature Publishing Group, ISSN: 2058-7546. DOI: 10.1038/s41560-019-0444-9. [Online]. Available: https://www.nature.com/articles/s41560-019-0444-9 (visited on 03/11/2022).

[9] J. F. Geisz, R. M. France, K. L. Schulte, M. A. Steiner, A. G. Norman, H. L. Guthrey, M. R. Young, T. Song, and T. Moriarty, "Six-junction III–V solar cells with 47.1% conversion efficiency under 143 Suns concentration", en, *Nature Energy*, vol. 5, no. 4, pp. 326–335, Apr. 2020, Number: 4 Publisher: Nature Publishing Group, ISSN: 2058-7546. DOI: 10.1038/s41560-020-0598-5. [Online]. Available: https://www.nature.com/articles/s41560-020-0598-5 (visited on 03/11/2022).

[10] R. Wang, T. Huang, J. Xue, J. Tong, K. Zhu, and Y. Yang, "Prospects for metal halide perovskite-based tandem solar cells", en, *Nature Photonics*, vol. 15, no. 6, pp. 411–425, Jun. 2021, Number: 6 Publisher: Nature Publishing Group, ISSN: 1749-4893. DOI: 10.1038/s41566-021-00809-8. [Online]. Available: https://www.nature.com/articles/s41566-021-00809-8 (visited on 03/11/2022).

[11] S. Samanta and D. Das, "Low-temperature synthesis of conducting boron-doped nanocrystalline silicon oxide thin films as the window layer of solar cells", en, *Current Applied Physics*, vol. 23, pp. 42–51, Mar. 2021, ISSN: 1567-1739. DOI: 10.1016/j.cap.2020.12.009. [Online]. Available: https://www.sciencedirect.com/science/article/pii/S156717392100002X (visited on 02/15/2022).

[12] K. Lee, H.-D. Um, D. Choi, J. Park, N. Kim, H. Kim, and K. Seo, "The development of transparent photovoltaics", en, *Cell Reports Physical Science*, vol. 1, no. 8, p. 100 143, Aug. 2020, ISSN: 26663864. DOI: 10.1016/j.xcrp.2020.100143. [Online]. Available: https://linkinghub.elsevier.com/retrieve/pii/S2666386420301478 (visited on 03/08/2022).

[13] J. Ramanujam, D. M. Bishop, T. K. Todorov, O. Gunawan, J. Rath, R. Nekovei, E. Artegiani, and A. Romeo, "Flexible cigs, cdte and a-si:h based thin film solar cells: A review", en, *Progress in Materials Science*, vol. 110, p. 100 619, May 2020, ISSN: 00796425. DOI: 10.1016/j.pmatsci.2019.100619. [Online]. Available: ht

tps://linkinghub.elsevier.com/retrieve/pii/S007964251930101X (visited on 03/08/2022).

[14] M. Fraczek, K. Gorski, and L. Wolaniuk, "Possibilities of Powering Military Equipment Based on Renewable Energy Sources", en, *Applied Sciences*, vol. 12, no. 2, p. 843, Jan. 2022, Number: 2 Publisher: Multidisciplinary Digital Publishing Institute, ISSN: 2076-3417. DOI: 10.3390/app12020843. [Online]. Available: https://www.mdpi.com/2076-3417/12/2/843 (visited on 03/08/2022).

[15] A. Aslam, U. Mehmood, M. H. Arshad, A. Ishfaq, J. Zaheer, A. Ul Haq Khan, and M. Sufyan, "Dye-sensitized solar cells (DSSCs) as a potential photovoltaic technology for the self-powered internet of things (IoTs) applications", en, *Solar Energy*, vol. 207, pp. 874–892, Sep. 2020, ISSN: 0038-092X. DOI: 10.1016/j.solener.2020.07.029. [Online]. Available: https://www.sciencedirect.com/science/article/pii/S0038092X20307611 (visited on 03/08/2022).

[16] G. Saianand, P. Sonar, G. J. Wilson, A.-I. Gopalan, V. A. L. Roy, G. E. Unni, K. Mamun Reza, B. Bahrami, K. Venkatramanan, and Q. Qiao, "Current advancements on charge selective contact interfacial layers and electrodes in flexible hybrid perovskite photovoltaics", en, *Journal of Energy Chemistry*, vol. 54, pp. 151–173, Mar. 2021, ISSN: 2095-4956. DOI: 10.1016/j.jechem.2020.05.050. [Online]. Available: https://www.sciencedirect.com/science/article/pii/S2095495620303867 (visited on 03/08/2022).

[17] M. Müller, M. Hývl, M. Kratzer, C. Teichert, S. Misra, M. Foldyna, L. Yu, P. Roca i Cabarrocas, T. Itoh, Z. Hájková, A. Vetushka, M. Ledinský, J. Kočka, and A. Fejfar, "Investigating inhomogeneous electronic properties of radial junction solar cells using correlative microscopy", *Japanese Journal of Applied Physics*, vol. 54, no. 8S1, 08KA08, Aug. 1, 2015, ISSN: 0021-4922, 1347-4065. DOI: 10.7567/JJAP.54.08KA08.

[18] Müller, Martin, "Thin film silicon for solar cells", English, Doctoral Thesis, Czech Technical University in Prague, Prague, 2018. [Online]. Available: https://www.fjfi.cvut.cz/cz/studium/doktorske-studium/archiv-doktorskych-praci/729-m-ller-martin (visited on 03/21/2022).

[19] G. Nogay, *Full-area passivating contacts with high and low thermal budgets : Solutions for high efficiency c-si solar cells*, eng, Lausanne, 2018.

[20] B. M. Kayes, H. A. Atwater, and N. S. Lewis, "Comparison of the device physics principles of planar and radial p-n junction nanorod solar cells", *Journal of Applied Physics*, vol. 97, no. 11, p. 114 302, May 2005, ISSN: 0021-8979. DOI: 10.1063/1.1

901835. [Online]. Available: http://aip.scitation.org/doi/abs/10.1063/1.1901835 (visited on 06/15/2017).

[21] L. Jun-Shuai, Z. Xia, Y. Xin, C. Xiong, L. Liang, C. Jian-Gong, H. Yong-Qing, and R. Xiao-Min, "Fabrication and electrical properties of axial and radial GaAs nanowire pn junction diode arrays", en, *Chinese Physics B*, vol. 23, no. 12, p. 128 503, Dec. 2014, ISSN: 1674-1056. DOI: 10.1088/1674-1056/23/12/128503. [Online]. Available: http://iopscience.iop.org/1674-1056/23/12/128503 (visited on 01/16/2015).

[22] T. Stelzner, M. Pietsch, G. Andrä, F. Falk, E. Ose, and S. Christiansen, "Silicon nanowire-based solar cells", en, *Nanotechnology*, vol. 19, no. 29, p. 295 203, 2008, ISSN: 0957-4484. DOI: 10.1088/0957-4484/19/29/295203. [Online]. Available: http://stacks.iop.org/0957-4484/19/i=29/a=295203 (visited on 01/15/2016).

[23] L. Tsakalakos, J. Balch, J. Fronheiser, B. A. Korevaar, O. Sulima, and J. Rand, "Silicon nanowire solar cells", *Applied Physics Letters*, vol. 91, no. 23, p. 233 117, Dec. 2007, ISSN: 0003-6951. DOI: 10.1063/1.2821113. [Online]. Available: http://aip.scitation.org/doi/10.1063/1.2821113 (visited on 06/15/2017).

[24] J. Alvarez, C. Marchat, A. Morisset, L. Dai, J.-P. Kleider, R. Cabal, and P. Roca i Cabarrocas, "Electrical scanning probe microscopy approaches to investigate solar cell junctions and devices", en, M. Razeghi, J. S. Lewis, G. A. Khodaparast, and P. Khalili, Eds., [Online; accessed 2020-11-03], Quantum Sensing, Nano Electronics, and Photonics XVII, San Francisco, United States: SPIE, Jan. 31, 2020, p. 32, ISBN: 978-1-5106-3339-1. DOI: 10.1117/12.2540422. [Online]. Available: https://www.spiedigitallibrary.org/conference-proceedings-of-spie/11288/2540422/Electrical-scanning-probe-microscopy-approaches-to-investigate-solar-cell-junctions/10.1117/12.2540422.full.

[25] M. S. Leite, M. Abashin, H. J. Lezec, A. Gianfrancesco, A. A. Talin, and N. B. Zhitenev, "Nanoscale imaging of photocurrent and efficiency in cdte solar cells", *ACS Nano*, vol. 8, no. 11, pp. 11 883–11 890, Nov. 25, 2014, ISSN: 1936-0851. DOI: 10.1021/nn5052585.

[26] K. Atamanuk, J. Luria, and B. D. Huey, "Direct afm-based nanoscale mapping and tomography of open-circuit voltages for photovoltaics", en, *Beilstein Journal of Nanotechnology*, vol. 9, no. 1, pp. 1802–1808, Jun. 14, 2018, publisher: Beilstein-Institut, ISSN: 2190-4286. DOI: 10.3762/bjnano.9.171.

[27] M. Padilla, B. Michl, B. Thaidigsmann, W. Warta, and M. Schubert, "Short-circuit current density mapping for solar cells", en, *Solar Energy Materials and Solar Cells*,

vol. 120, pp. 282–288, Jan. 2014, ISSN: 09270248. DOI: 10.1016/j.solmat.2013.09.019.

[28] M. S. Leite, M. Abashin, H. J. Lezec, A. G. Gianfrancesco, A. A. Talin, and N. B. Zhitenev, "Mapping the local photoelectronic properties of polycrystalline solar cells through high resolution laser-beam-induced current microscopy", *IEEE Journal of Photovoltaics*, vol. 4, no. 1, pp. 311–316, Jan. 2014, ISSN: 2156-3381, 2156-3403. DOI: 10.1109/JPHOTOV.2013.2284860.

[29] A. Fejfar, A. Vetushka, V. Kalusová, O. Čertík, M. Ledinský, B. Rezek, J. Stuchlík, and J. Kočka, "Relation of nanoscale and macroscopic properties of mixed-phase silicon thin films", en, *physica status solidi (a)*, vol. 207, no. 3, pp. 582–586, 2010, ISSN: 1862-6319. DOI: 10.1002/pssa.200982907.

[30] G. Binnig, C. F. Quate, and C. Gerber, "Atomic force microscope", *Physical Review Letters*, vol. 56, no. 9, pp. 930–933, Mar. 3, 1986. DOI: 10.1103/PhysRevLett.56.930.

[31] J. Jo, S.-I. Na, S.-S. Kim, T.-W. Lee, Y. Chung, S.-J. Kang, D. Vak, and D.-Y. Kim, "Three-dimensional bulk heterojunction morphology for achieving high internal quantum efficiency in polymer solar cells", en, *Advanced Functional Materials*, vol. 19, no. 15, pp. 2398–2406, Aug. 10, 2009, ISSN: 1616-3028. DOI: 10.1002/adfm.200900183.

[32] Y. Nasuno, M. Kondo, and A. Matsuda, "Effects of substrate surface morphology on microcrystalline silicon solar cells", *Japanese Journal of Applied Physics*, vol. 40, no. 4A, p. L303, 2001.

[33] X. Zhang, X. Zheng, G. Wang, and Y. Zhao, "Initial growth of intrinsic microcrystalline silicon thin film: Dependence on pre-hydrogen glow discharge and substrate surface morphology", *Applied Surface Science*, vol. 257, no. 7, pp. 3014–3019, Jan. 15, 2011, ISSN: 0169-4332. DOI: 10.1016/j.apsusc.2010.10.109.

[34] S. Zhang, L. Ye, W. Zhao, B. Yang, Q. Wang, and J. Hou, "Realizing over 10optimization", en, *Science China Chemistry*, vol. 58, no. 2, pp. 248–256, Jan. 8, 2015, ISSN: 1674-7291, 1869-1870. DOI: 10.1007/s11426-014-5273-x.

[35] B. Shi, B. Liu, J. Luo, Y. Li, C. Zheng, X. Yao, L. Fan, J. Liang, Y. Ding, C. Wei, D. Zhang, Y. Zhao, and X. Zhang, "Enhanced light absorption of thin perovskite solar cells using textured substrates", *Solar Energy Materials and Solar Cells*, vol. 168, pp. 214–220, Aug. 2017, ISSN: 0927-0248. DOI: 10.1016/j.solmat.2017.04.038.

[36] "Electrical Measurement Techniques in Atomic Force Microscopy", vol. 35, ISSN: 1040-8436, 1547-6561.

[37] F. Hui, C. Wen, S. Chen, E. Koren, R. Dechter, D. Lewis, and M. Lanza, "Emerging Scanning Probe–Based Setups for Advanced Nanoelectronic Research", en, *Advanced Functional Materials*, vol. 30, no. 18, 2020, ISSN: 1616-3028. DOI: `10.1002/adfm.201902776`. [Online]. Available: `https://onlinelibrary.wiley.com/doi/abs/10.1002/adfm.201902776` (visited on 03/17/2022).

[38] C. Ballif, H. R. Moutinho, and M. M. Al-Jassim, "Cross-sectional electrostatic force microscopy of thin-film solar cells", *Journal of Applied Physics*, vol. 89, no. 2, pp. 1418–1424, Jan. 15, 2001, publisher: American Institute of Physics, ISSN: 0021-8979. DOI: `10.1063/1.1329669`.

[39] P. Narchi, J. Alvarez, P. Chrétien, G. Picardi, R. Cariou, M. Foldyna, P. Prod'homme, J.-P. Kleider, and P. R. Cabarrocas, "Cross-sectional investigations on epitaxial silicon solar cells by kelvin and conducting probe atomic force microscopy: Effect of illumination", En, *Nanoscale Research Letters*, vol. 11, no. 1, p. 55, Feb. 1, 2016, ISSN: 1556-276X. DOI: `10.1186/s11671-016-1268-1`.

[40] H. Hoppe, T. Glatzel, M. Niggemann, A. Hinsch, M. C. Lux-Steiner, and N. S. Sariciftci, "Kelvin probe force microscopy study on conjugated polymer/fullerene bulk heterojunction organic solar cells", *Nano Letters*, vol. 5, no. 2, pp. 269–274, Feb. 1, 2005, ISSN: 1530-6984. DOI: `10.1021/nl048176c`.

[41] T. Meoded, R. Shikler, N. Fried, and Y. Rosenwaks, "Direct measurement of minority carriers diffusion length using kelvin probe force microscopy", *Applied Physics Letters*, vol. 75, no. 16, pp. 2435–2437, Oct. 18, 1999, ISSN: 00036951. DOI: `doi:10.1063/1.125039`.

[42] S. Sadewasser, T. Glatzel, S. Schuler, S. Nishiwaki, R. Kaigawa, and M. C. Lux-Steiner, "Kelvin probe force microscopy for the nano scale characterization of chalcopyrite solar cell materials and devices", *Thin Solid Films*, vol. 431–432, pp. 257–261, May 1, 2003, ISSN: 0040-6090. DOI: `10.1016/S0040-6090(03)00267-0`.

[43] P. Narchi, V. Neplokh, V. Piazza, T. Bearda, F. Bayle, M. Foldyna, C. Toccafondi, P. Prod'homme, M. Tchernycheva, and P. Roca i Cabarrocas, "Surface potential investigation on interdigitated back contact solar cells by scanning electron microscopy and kelvin probe force microscopy: Effect of electrical bias", *Solar Energy Materials and Solar Cells*, vol. 161, pp. 263–269, Mar. 2017, ISSN: 0927-0248. DOI: `10.1016/j.solmat.2016.12.009`.

[44] en, ser. NanoScience and Technology. Springer International Publishing, DOI: 10.1007/978-3-030-15612-1, ISBN: 978-3-030-15611-4.

[45] K. Maknys, A. G. Ulyashin, H. Stiebig, A. Y. Kuznetsov, and B. G. Svensson, "Analysis of ito thin layers and interfaces in heterojunction solar cells structures by afm, scm and ssrm methods", *Thin Solid Films*, EMSR 2005 - Proceedings of Symposium F on Thin Film and Nanostructured Materials for Photovoltaics, vol. 511, pp. 98–102, Jul. 26, 2006, ISSN: 0040-6090. DOI: 10.1016/j.tsf.2005.12.006.

[46] In, *Capacitance Spectroscopy of Semiconductors*, ISBN: 978-1-315-15013-0.

[47] C. S. Jiang, J. Moseley, C. Xiao, S. Harvey, S. Farrell, E. Colegrove, W. K. Metzger, and M. M. Al-Jassim, "Imaging hole-density inhomogeneity in arsenic-doped cdte thin films by scanning capacitance microscopy", en, *Solar Energy Materials and Solar Cells*, vol. 209, p. 110 468, Jun. 1, 2020, ISSN: 0927-0248. DOI: 10.1016/j.solmat.2020.110468.

[48] *Crystal Research and Technology*, no. 6, ISSN: 1521-4079. DOI: 10.1002/crat.201700019.

[49] M. L. O'Malley, G. L. Timp, S. V. Moccio, J. P. Garno, and R. N. Kleiman, "Quantification of scanning capacitance microscopy imaging of the *pn* junction through electrical simulation", en, *Applied Physics Letters*, vol. 74, no. 2, pp. 272–274, Jan. 11, 1999, ISSN: 0003-6951, 1077-3118. DOI: 10.1063/1.123278.

[50] C. C. Williams, "Two-dimensional dopant profiling by scanning capacitance microscopy", en, *Annual Review of Materials Science*, vol. 29, no. 1, pp. 471–504, Aug. 1999, ISSN: 0084-6600. DOI: 10.1146/annurev.matsci.29.1.471.

[51] M. P. Murrell, M. E. Welland, S. J. O'Shea, T. M. H. Wong, J. R. Barnes, A. W. McKinnon, M. Heyns, and S. Verhaverbeke, "Spatially resolved electrical measurements of sio2 gate oxides using atomic force microscopy", *Applied Physics Letters*, vol. 62, no. 7, pp. 786–788, Feb. 15, 1993, publisher: American Institute of Physics, ISSN: 0003-6951. DOI: 10.1063/1.108579.

[52] C. Li, S. Minne, B. Pittenger, A. Mednick, M. Guide, and T.-Q. Nguyen, "Simultaneous electrical and mechanical property mapping at the nanoscale with peakforce tuna", *Bruker Application Note 132*, 2011, 00007. [Online]. Available: http://www.bruker-axs.com/application_notes_afm.html.

[53] D. C. Coffey, O. G. Reid, D. B. Rodovsky, G. P. Bartholomew, and D. S. Ginger, "Mapping local photocurrents in polymer/fullerene solar cells with photoconductive atomic force microscopy", *Nano Letters*, vol. 7, no. 3, pp. 738–744, Mar. 1, 2007, ISSN: 1530-6984. DOI: 10.1021/nl062989e.

[54] M. Ledinský, A. Fejfar, A. Vetushka, J. Stuchlík, B. Rezek, and J. Kočka, "Local photoconductivity of microcrystalline silicon thin films measured by conductive atomic force microscopy", en, *physica status solidi (RRL) - Rapid Research Letters*, vol. 5, no. 10-11, pp. 373–375, Nov. 2011, ISSN: 18626254. DOI: 10.1002/pssr.201105413.

[55] S. Hong, S. Tong, W. I. Park, Y. Hiranaga, Y. Cho, and A. Roelofs, "Charge gradient microscopy", en, *Proceedings of the National Academy of Sciences*, vol. 111, no. 18, pp. 6566–6569, May 6, 2014, ISSN: 0027-8424, 1091-6490. DOI: 10.1073/pnas.1324178111.

[56] W. Frammelsberger, G. Benstetter, J. Kiely, and R. Stamp, "C-afm-based thickness determination of thin and ultra-thin sio 2 films by use of different conductive-coated probe tips", en, *Applied Surface Science*, vol. 253, no. 7, pp. 3615–3626, Jan. 2007, ISSN: 01694332. DOI: 10.1016/j.apsusc.2006.07.070.

[57] J. Alvarez, I. Ngo, M.-E. Gueunier-Farret, J.-P. Kleider, L. Yu, P. R. Cabarrocas, S. Perraud, E. Rouvière, C. Celle, C. Mouchet, and J.-P. Simonato, "Conductive-probe atomic force microscopy characterization of silicon nanowire", en, *Nanoscale Research Letters*, vol. 6, no. 1, p. 110, Jan. 31, 2011, PMID: 21711623, ISSN: 1556-276X. DOI: 10.1186/1556-276X-6-110.

[58] H.-N. Lin, H.-L. Lin, S.-S. Wang, L.-S. Yu, G.-Y. Perng, S.-A. Chen, and S.-H. Chen, "Nanoscale charge transport in an electroluminescent polymer investigated by conducting atomic force microscopy", *Applied Physics Letters*, vol. 81, no. 14, pp. 2572–2574, Sep. 30, 2002, ISSN: 0003-6951, 1077-3118. DOI: 10.1063/1.1509464.

[59] X. Zhou, S. A. Dayeh, D. Aplin, D. Wang, and E. T. Yu, "Direct observation of ballistic and drift carrier transport regimes in inas nanowires", *Applied Physics Letters*, vol. 89, no. 5, p. 053 113, Jul. 31, 2006, ISSN: 0003-6951, 1077-3118. DOI: 10.1063/1.2236589.

[60] H. Zhang, E. J. Miller, and E. T. Yu, "Analysis of leakage current mechanisms in schottky contacts to GaN and $Al_{0.25}Ga_{0.75}N$/GaN grown by molecular-beam epitaxy", *Journal of Applied Physics*, vol. 99, no. 2, p. 023 703, Jan. 15, 2006, ISSN: 0021-8979, 1089-7550. DOI: 10.1063/1.2159547.

[61] T. G. Ruskell, R. K. Workman, D. Chen, D. Sarid, S. Dahl, and S. Gilbert, "High resolution fowler-nordheim field emission maps of thin silicon oxide layers", *Applied Physics Letters*, vol. 68, no. 1, pp. 93–95, Jan. 1, 1996, ISSN: 0003-6951, 1077-3118. DOI: 10.1063/1.116782.

[62] M. Rumler, M. Rommel, J. Erlekampf, M. Azizi, T. Geiger, A. J. Bauer, E. Meißner, and L. Frey, "Characterization of grain boundaries in multicrystalline silicon with high lateral resolution using conductive atomic force microscopy", *Journal of Applied Physics*, vol. 112, no. 3, p. 034 909, Aug. 1, 2012, ISSN: 0021-8979. DOI: 10.1063/1.4746742.

[63] Y. Kutes, Y. Zhou, J. L. Bosse, J. Steffes, N. P. Padture, and B. D. Huey, "Mapping the Photoresponse of CH3NH3PbI3 Hybrid Perovskite Thin Films at the Nanoscale", *Nano Letters*, vol. 16, no. 6, pp. 3434–3441, Jun. 2016, ISSN: 1530-6984. DOI: 10.1021/acs.nanolett.5b04157. [Online]. Available: http://dx.doi.org/10.1021/acs.nanolett.5b04157 (visited on 06/13/2016).

[64] H. Masuda, M. Takeuchi, and T. Takahashi, "Local photocurrent detection on InAs wires by conductive AFM", en, *Ultramicroscopy*, Proceedings of the Sixth International Conference on Scanning Probe Microscopy, Sensors and Nanostructures, vol. 105, no. 1, pp. 137–142, Nov. 2005, ISSN: 0304-3991. DOI: 10.1016/j.ultramic.2005.06.029. [Online]. Available: http://www.sciencedirect.com/science/article/pii/S0304399105001324 (visited on 10/07/2020).

[65] P. De Wolf, "Cross-sectional nano-spreading resistance profiling", en, *Journal of Vacuum Science Technology B: Microelectronics and Nanometer Structures*, vol. 16, no. 1, p. 355, Jan. 1998, ISSN: 0734211X. DOI: 10.1116/1.589810.

[66] P. De Wolf, M. Geva, T. Hantschel, W. Vandervorst, and R. B. Bylsma, "Two-dimensional carrier profiling of inp structures using scanning spreading resistance microscopy", *Applied Physics Letters*, vol. 73, no. 15, pp. 2155–2157, Oct. 12, 1998, ISSN: 0003-6951. DOI: 10.1063/1.122408.

[67] D. Alvarez, "Scanning spreading resistance microscopy for the characterization of advanced silicon devices (gescande spreidingsweerstand microscopie voor de karakterisatie van geavanceerde silicium componenten)", 2007, [Online; accessed 2017-06-15]. [Online]. Available: https://lirias.kuleuven.be/bitstream/123456789/335851/1/PhD_SSRM_Alvarez_v1+7.pdf.

[68] J. K. Prüßing, T. Böckendorf, G. Hamdana, E. Peiner, and H. Bracht, "Defect distribution in boron doped silicon nanostructures characterized by means of scanning spreading resistance microscopy", *Journal of Applied Physics*, vol. 127, no. 5, p. 055 703, Feb. 4, 2020, publisher: American Institute of Physics, ISSN: 0021-8979. DOI: 10.1063/1.5134558.

[69] F. Gołek, P. Mazur, Z. Ryszka, and S. Zuber, "Afm image artifacts", en, *Applied Surface Science*, Selected Papers from the 6th International Workshop on Surface

Physics “Functional Materials”, vol. 304, pp. 11–19, Jun. 15, 2014, ISSN: 0169-4332. DOI: 10.1016/j.apsusc.2014.01.149.

[70] S. N. Magonov and M.-H. Whangbo, *Surface Analysis with STM and AFM: Experimental and Theoretical Aspects of Image Analysis*, en. John Wiley Sons, Sep. 26, 2008, ISBN: 978-3-527-61510-0.

[71] A. Fejfar, M. Hývl, A. Vetushka, P. Pikna, Z. Hájková, M. Ledinský, J. Kočka, P. Klapetek, A. Marek, A. Mašková, J. Vyskočil, J. Merkel, C. Becker, T. Itoh, S. Misra, M. Foldyna, L. Yu, and P. Roca i Cabarrocas, “Correlative microscopy of radial junction nanowire solar cells using nanoindent position markers”, *Solar Energy Materials and Solar Cells*, EMRS 2014 Spring Meeting – Advanced materials and characterization techniques for solar cells II, vol. 135, pp. 106–112, Apr. 1, 2015, ISSN: 0927-0248. DOI: 10.1016/j.solmat.2014.10.027.

[72] M. Hývl, M. Müller, T.-H. Stuchlíková, J. Stuchlík, M. Šilhavík, J. Kočka, A. Fejfar, and J. Červenka, “Nucleation and growth of metal-catalyzed silicon nanowires under plasma”, en, *Nanotechnology*, vol. 31, no. 22, p. 225 601, Mar. 2020, publisher: IOP Publishing, ISSN: 0957-4484. DOI: 10.1088/1361-6528/ab76ef.

[73] M. Hývl, G. Nogay, P. Loper, F.-J. Haug, Q. Jeangros, A. Fejfar, C. Ballif, and M. Ledinský, “Nanoscale study of the hole-selective passivating contacts with high thermal budget using c-afm tomography”, en, *ACS Applied Materials Interfaces*, vol. 13, no. 8, pp. 9994–10 000, Mar. 3, 2021, ISSN: 1944-8244, 1944-8252. DOI: 10.1021/acsami.0c21282.

[74] T. Hantschel, C. Demeulemeester, P. Eyben, V. Schulz, O. Richard, H. Bender, and W. Vandervorst, “Conductive diamond tips with sub-nanometer electrical resolution for characterization of nanoelectronics device structures”, en, *physica status solidi (a)*, vol. 206, no. 9, pp. 2077–2081, 2009, ISSN: 1862-6319. DOI: 10.1002/pssa.200982212.

[75] U. Celano, T. Hantschel, G. Giammaria, R. C. Chintala, T. Conard, H. Bender, and W. Vandervorst, “Evaluation of the electrical contact area in contact-mode scanning probe microscopy”, *Journal of Applied Physics*, vol. 117, no. 21, p. 214 305, Jun. 7, 2015, ISSN: 0021-8979, 1089-7550. DOI: 10.1063/1.4921878.

[76] S. A. Sumaiya, A. Martini, and M. Z. Baykara, “Improving the reliability of conductive atomic force microscopy-based electrical contact resistance measurements”, en, *Nano Express*, vol. 1, no. 3, p. 030 023, Nov. 2020, publisher: IOP Publishing, ISSN: 2632-959X. DOI: 10.1088/2632-959X/abcae0.

[77] L. Jiang, J. Weber, F. M. Puglisi, P. Pavan, L. Larcher, W. Frammelsberger, G. Benstetter, and M. Lanza, "Understanding current instabilities in conductive atomic force microscopy", *Materials*, vol. 12, no. 3, Feb. 1, 2019, PMID: 30717254 PMCID: PMC6384822, ISSN: 1996-1944. DOI: 10.3390/ma12030459. [Online]. Available: https://www.ncbi.nlm.nih.gov/pmc/articles/PMC6384822/.

[78] M. Lanza, M. Porti, M. Nafría, X. Aymerich, E. Whittaker, and B. Hamilton, "Note: Electrical resolution during conductive atomic force microscopy measurements under different environmental conditions and contact forces", *Review of Scientific Instruments*, vol. 81, no. 10, p. 106 110, Oct. 1, 2010, publisher: American Institute of Physics, ISSN: 0034-6748. DOI: 10.1063/1.3491956.

[79] M. Rommel, J. D. Jambreck, M. Lemberger, A. J. Bauer, L. Frey, K. Murakami, C. Richter, and P. Weinzierl, "Influence of parasitic capacitances on conductive afm i-v measurements and approaches for its reduction", *Journal of Vacuum Science Technology B*, vol. 31, no. 1, 01A108, Jan. 1, 2013, ISSN: 2166-2746, 2166-2754. DOI: 10.1116/1.4768679.

[80] P. Klapetek, A. Campbell, and V. Bursikova, "Fast mechanical model for probe-sample elastic deformation estimation in scanning probe microscopy", *Ultramicroscopy*, vol. 201, Mar. 1, 2019. DOI: 10.1016/j.ultramic.2019.03.010.

[81] P Eyben, S Denis, T Clarysse, and W Vandervorst, "Progress towards a physical contact model for scanning spreading resistance microscopy", *Materials Science and Engineering: B*, E-MRS 2002 Symposium E: Advanced Characterisation of Semiconductors, vol. 102, no. 1–3, pp. 132–137, Sep. 15, 2003, ISSN: 0921-5107. DOI: 10.1016/S0921-5107(03)00019-9.

[82] I. Beinik, "Electrical characterization of semiconductor nanostructures by conductive probe based atomic force microscopy", English, [Online; accessed 2015-10-05], Ph.D. dissertation, Mar. 2011. [Online]. Available: http://www.unileoben.ac.at/images/stories/Bibliothek/edoc/AC08511205n01vt.pdf.

[83] R. O'Hayre, G. Feng, W. D. Nix, and F. B. Prinz, "Quantitative impedance measurement using atomic force microscopy", en, *Journal of Applied Physics*, vol. 96, no. 6, pp. 3540–3549, Sep. 15, 2004, ISSN: 0021-8979, 1089-7550. DOI: 10.1063/1.1778217.

[84] D.-Z. Guo, S.-M. Hou, G.-M. Zhang, and Z.-Q. Xue, "Conductance fluctuation and degeneracy in nanocontact between a conductive AFM tip and a granular surface under small-load conditions", en, *Applied Surface Science*, vol. 252, no. 14, pp. 5149–5157, May 2006, ISSN: 01694332. DOI: 10.1016/j.apsusc.2005.07.058.

[Online]. Available: http://linkinghub.elsevier.com/retrieve/pii/S0169433205010408 (visited on 05/31/2018).

[85] F. Houzé, R. Meyer, O. Schneegans, and L. Boyer, "Imaging the local electrical properties of metal surfaces by atomic force microscopy with conducting probes", en, *Applied Physics Letters*, vol. 69, no. 13, pp. 1975–1977, Sep. 23, 1996, ISSN: 0003-6951, 1077-3118. DOI: 10.1063/1.117179.

[86] *Current at the nanoscale*, en-US, [Online; accessed 2018-06-06]. [Online]. Available: https://www.worldscientific.com/worldscibooks/10.1142/8371.

[87] S. V. Kalinin and A. Gruverman, *Scanning Probe Microscopy: Electrical and Electromechanical Phenomena at the Nanoscale*, en. Springer Science Business Media, Apr. 3, 2007, Google-Books-ID: Ua8fxzc2kTwC, ISBN: 978-0-387-28668-6.

[88] T. K. Ghanem, E. D. Williams, and M. S. Fuhrer, "Characterization of the electrical contact between a conductive atomic force microscope cantilever and a carbon nanotube", *Journal of Applied Physics*, vol. 110, no. 5, p. 054 305, 2011.

[89] D. S. Grierson, E. E. Flater, and R. W. Carpick, "Accounting for the jkr–dmt transition in adhesion and friction measurements with atomic force microscopy", *Journal of Adhesion Science and Technology*, vol. 19, no. 3-5, pp. 291–311, Jan. 1, 2005, publisher: Taylor Francis eprint: https://doi.org/10.1163/1568561054352685, ISSN: 0169-4243. DOI: 10.1163/1568561054352685.

[90] A. Schulze, A. S. Verhulst, A. Nazir, T. Hantschel, P. Eyben, and W. Vandervorst, "A comprehensive model for the electrical nanocontact on germanium for scanning spreading resistance microscopy applications", *Journal of Applied Physics*, vol. 113, no. 11, p. 114 310, Mar. 21, 2013, ISSN: 0021-8979, 1089-7550. DOI: 10.1063/1.4795141.

[91] A. Schulze, R. Cao, P. Eyben, T. Hantschel, and W. Vandervorst, "Outwitting the series resistance in scanning spreading resistance microscopy", *Ultramicroscopy*, vol. 161, pp. 59–65, Feb. 2016, ISSN: 0304-3991. DOI: 10.1016/j.ultramic.2015.10.029.

[92] L. S. C. Pingree, M. C. Hersam, M. M. Kern, B. J. Scott, and T. J. Marks, "Spatially-resolved electroluminescence of operating organic light-emitting diodes using conductive atomic force microscopy", *Applied Physics Letters*, vol. 85, no. 2, pp. 344–346, Jul. 12, 2004, ISSN: 0003-6951, 1077-3118. DOI: 10.1063/1.1765206.

[93] T. Kirchartz, A. Helbig, W. Reetz, M. Reuter, J. H. Werner, and U. Rau, "Reciprocity between electroluminescence and quantum efficiency used for the characterization of silicon solar cells", en, *Progress in Photovoltaics: Research and Applications*, vol. 17, no. 6, pp. 394–402, Sep. 1, 2009, ISSN: 1099-159X. DOI: 10.1002/pip.895.

[94] U. Rau, "Reciprocity relation between photovoltaic quantum efficiency and electroluminescent emission of solar cells", *Physical Review B*, vol. 76, no. 8, p. 085 303, Aug. 2, 2007. DOI: 10.1103/PhysRevB.76.085303.

[95] M. Chiesa, L. Bürgi, J.-S. Kim, R. Shikler, R. H. Friend, and H. Sirringhaus, "Correlation between surface photovoltage and blend morphology in polyfluorene-based photodiodes", *Nano Letters*, vol. 5, no. 4, pp. 559–563, Apr. 1, 2005, publisher: American Chemical Society, ISSN: 1530-6984. DOI: 10.1021/nl047929s.

[96] E. J. Spadafora, R. Demadrille, B. Ratier, and B. Grévin, "Imaging the carrier photogeneration in nanoscale phase segregated organic heterojunctions by kelvin probe force microscopy", *Nano Letters*, vol. 10, no. 9, pp. 3337–3342, Sep. 8, 2010, ISSN: 1530-6984. DOI: 10.1021/nl101001d.

[97] F. Feldmann, G. Nogay, P. Löper, D. L. Young, B. G. Lee, P. Stradins, M. Hermle, and S. W. Glunz, "Charge carrier transport mechanisms of passivating contacts studied by temperature-dependent j-v measurements", en, *Solar Energy Materials and Solar Cells*, vol. 178, pp. 15–19, May 2018, ISSN: 09270248. DOI: 10.1016/j.solmat.2018.01.008.

[98] J. Luria, Y. Kutes, A. Moore, L. Zhang, E. A. Stach, and B. D. Huey, "Charge transport in cdte solar cells revealed by conductive tomographic atomic force microscopy", en, *Nature Energy*, vol. 1, no. 11, pp. 1–6, Sep. 26, 2016, number: 11 publisher: Nature Publishing Group, ISSN: 2058-7546. DOI: 10.1038/nenergy.2016.150.

[99] M. Al-Ghzaiwat, M. Foldyna, T. Fuyuki, W. Chen, E. V. Johnson, J. Meot, and P. Roca i Cabarrocas, "Large area radial junction silicon nanowire solar mini-modules", en, *Scientific Reports*, vol. 8, no. 1, p. 1651, Jan. 26, 2018, ISSN: 2045-2322. DOI: 10.1038/s41598-018-20126-5.

[100] J. G. Fossum, F. A. Lindholm, and M. A. Shibib, "The importance of surface recombination and energy-bandgap arrowing in p-n-junction silicon solar cells", *IEEE Transactions on Electron Devices*, vol. 26, no. 9, pp. 1294–1298, Sep. 1979, event: IEEE Transactions on Electron Devices, ISSN: 1557-9646. DOI: 10.1109/T-ED.1979.19596.

[101] J. Zhao, A. Wang, and M. A. Green, "24·5% efficiency silicon pert cells on mcz substrates and 24·7% efficiency perl cells on fz substrates", en, *Progress in Photovoltaics: Research and Applications*, vol. 7, no. 6, pp. 471–474, 1999, ISSN: 1099-159X. DOI: 10.1002/(SICI)1099-159X(199911/12)7:6{\textless}471::AID-PIP298{\textgreater}3.0.CO;2-7.

[102] F. Haase, C. Hollemann, S. Schäfer, A. Merkle, M. Rienäcker, J. Krügener, R. Brendel, and R. Peibst, "Laser contact openings for local poly-si-metal contacts enabling 26.1%-efficient polo-ibc solar cells", en, *Solar Energy Materials and Solar Cells*, vol. 186, pp. 184–193, Nov. 1, 2018, ISSN: 0927-0248. DOI: 10.1016/j.solmat.2018.06.020.

[103] S. W. Glunz and F. Feldmann, "Sio2 surface passivation layers – a key technology for silicon solar cells", en, *Solar Energy Materials and Solar Cells*, vol. 185, pp. 260–269, Oct. 2018, ISSN: 09270248. DOI: 10.1016/j.solmat.2018.04.029.

[104] Y. Chen, D. Chen, C. Liu, Z. Wang, Y. Zou, Y. He, Y. Wang, L. Yuan, J. Gong, W. Lin, X. Zhang, Y. Yang, H. Shen, Z. Feng, P. P. Altermatt, and P. J. Verlinden, "Mass production of industrial tunnel oxide passivated contacts (i-topcon) silicon solar cells with average efficiency over 23% and modules over 345 w", en, *Progress in Photovoltaics: Research and Applications*, vol. 27, no. 10, pp. 827–834, 2019, $_eprint : https : //onlinelibrary.wiley.com/doi/pdf/10.1002/pip.3180$, ISSN: 1099-159X. DOI: 10.1002/pip.3180.

[105] JinkoSolar, "Large-area n-type topcon monocrystalline silicon solar cell reaches record high efficiency of 24.2%", 2019, [Online; accessed 2019-07-23]. [Online]. Available: https://www.jinkosolar.com/press_detail_1772.html.

[106] J. Chen, *The development of n-type topcon cell and module in jolywood*, 9th International Conference on Crystalline Silicon Photovoltaics, 2019.

[107] G. Nogay, J. Stuckelberger, P. Wyss, Q. Jeangros, C. Allebé, X. Niquille, F. Debrot, M. Despeisse, F.-J. Haug, P. Löper, and C. Ballif, "Silicon-rich silicon carbide hole-selective rear contacts for crystalline-silicon-based solar cells", *ACS Applied Materials Interfaces*, vol. 8, no. 51, pp. 35 660–35 667, Dec. 28, 2016, ISSN: 1944-8244. DOI: 10.1021/acsami.6b12714.

[108] G. Nogay, J. Stuckelberger, P. Wyss, E. Rucavado, C. Allebé, T. Koida, M. Morales-Masis, M. Despeisse, F.-J. Haug, P. Löper, and C. Ballif, "Interplay of annealing temperature and doping in hole selective rear contacts based on silicon-rich silicon-carbide thin films", en, *Solar Energy Materials and Solar Cells*, Proceedings of the 7th international conference on Crystalline Silicon Photovoltaics, vol. 173, pp. 18–24, Dec. 1, 2017, ISSN: 0927-0248. DOI: 10.1016/j.solmat.2017.06.039.

[109] G. Nogay, A. Ingenito, E. Rucavado, Q. Jeangros, J. Stuckelberger, P. Wyss, M. Morales-Masis, F. Haug, P. Löper, and C. Ballif, "Crystalline silicon solar cells with coannealed electron- and hole-selective sicxpassivating contacts", *IEEE Journal of Photovoltaics*, vol. 8, no. 6, pp. 1478–1485, Nov. 2018, ISSN: 2156-3381. DOI: 10.1109/JPHOTOV.2018.2866189.

[110] I. Post, P. Ashburn, and G. Wolstenholme, "Polysilicon emitters for bipolar transistors: A review and re-evaluation of theory and experiment", *IEEE Transactions on Electron Devices*, vol. 39, no. 7, pp. 1717–1731, Jul. 1992, ISSN: 1557-9646. DOI: 10.1109/16.141239.

[111] T. F. Wietler, D. Tetzlaff, J. Krügener, M. Rienäcker, F. Haase, Y. Larionova, R. Brendel, and R. Peibst, "Pinhole density and contact resistivity of carrier selective junctions with polycrystalline silicon on oxide", *Applied Physics Letters*, vol. 110, no. 25, p. 253 902, Jun. 19, 2017, ISSN: 0003-6951. DOI: 10.1063/1.4986924.

[112] F. Feldmann, G. Nogay, J.-I. Polzin, B. Steinhauser, A. Richter, A. Fell, C. Schmiga, M. Hermle, and S. W. Glunz, "A study on the charge carrier transport of passivating contacts", *IEEE Journal of Photovoltaics*, vol. 8, no. 6, pp. 1503–1509, Nov. 2018, event: IEEE Journal of Photovoltaics, ISSN: 2156-3403. DOI: 10.1109/JPHOTOV.2018.2870735.

[113] N. Folchert, M. Rienäcker, A. A. Yeo, B. Min, R. Peibst, and R. Brendel, "Temperature-dependent contact resistance of carrier selective poly-Si on oxide junctions", en, *Solar Energy Materials and Solar Cells*, vol. 185, pp. 425–430, Oct. 1, 2018, ISSN: 0927-0248. DOI: 10.1016/j.solmat.2018.05.046.

[114] S. Richter, Y. Larionova, S. Großer, M. Menzel, H. Schulte-Huxel, R. Peibst, R. Brendel, and C. Hagendorf, "Evaluation of localized vertical current formation in carrier selective passivation layers of silicon solar cells by conductive afm", *AIP Conference Proceedings*, vol. 2147, no. 1, p. 040 017, Aug. 27, 2019, publisher: American Institute of Physics, ISSN: 0094-243X. DOI: 10.1063/1.5123844.

[115] A. S. Kale, W. Nemeth, S. U. Nanayakkara, H. Guthrey, M. Page, M. Al-Jassim, S. Agarwal, and P. Stradins, "Tunneling or pinholes: Understanding the transport mechanisms in siox based passivated contacts for high-efficiency silicon solar cells", ISSN: 0160-8371, 2018 IEEE 7th World Conference on Photovoltaic Energy Conversion (WCPEC) (A Joint Conference of 45th IEEE PVSC, 28th PVSEC 34th EU PVSEC), Jun. 2018, pp. 3473–3476. DOI: 10.1109/PVSC.2018.8547211.

[116] U. Celano, F.-C. Hsia, D. Vanhaeren, K. Paredis, T. E. M. Nordling, J. G. Buijnsters, T. Hantschel, and W. Vandervorst, "Mesoscopic physical removal of material

using sliding nano-diamond contacts", En, *Scientific Reports*, vol. 8, no. 1, p. 2994, Feb. 14, 2018, ISSN: 2045-2322. DOI: 10.1038/s41598-018-21171-w.

[117] U. Celano, *Metrology and Physical Mechanisms in New Generation Ionic Devices*, en, ser. Springer Theses. Cham: Springer International Publishing, 2016, DOI: 10.1007/978-3-319-39531-9, ISBN: 978-3-319-39530-2. [Online]. Available: http://link.springer.com/10.1007/978-3-319-39531-9.

[118] Asuha, T. Kobayashi, O. Maida, M. Inoue, M. Takahashi, Y. Todokoro, and H. Kobayashi, "Ultrathin silicon dioxide layers with a low leakage current density formed by chemical oxidation of si", *Applied Physics Letters*, vol. 81, no. 18, pp. 3410–3412, Oct. 22, 2002, ISSN: 0003-6951. DOI: 10.1063/1.1517723.

[119] H. Kobayashi Asuha, O. Maida, M. Takahashi, and H. Iwasa, "Nitric acid oxidation of Si to form ultrathin silicon dioxide layers with a low leakage current density", *Journal of Applied Physics*, vol. 94, no. 11, pp. 7328–7335, Nov. 10, 2003, ISSN: 0021-8979. DOI: 10.1063/1.1621720.

[120] S. Chen, L. Jiang, M. Buckwell, X. Jing, Y. Ji, E. Grustan-Gutierrez, F. Hui, Y. Shi, M. Rommel, A. Paskaleva, G. Benstetter, W. H. Ng, A. Mehonic, A. J. Kenyon, and M. Lanza, "On the limits of scalpel afm for the 3d electrical characterization of nanomaterials", en, *Advanced Functional Materials*, vol. 28, no. 52, p. 1 802 266, 2018, ISSN: 1616-3028. DOI: 10.1002/adfm.201802266.

[121] U. Celano, L. Goux, A. Belmonte, K. Opsomer, A. Franquet, A. Schulze, C. Detavernier, O. Richard, H. Bender, M. Jurczak, and W. Vandervorst, *Three-dimensional observation of the conductive filament in nanoscaled resistive memory devices*, EN, DOI: 10.1021/nl500049g, Apr. 10, 2014. [Online]. Available: https://pubs.acs.org/doi/full/10.1021/nl500049g.

[122] J. Song, Y. Zhou, N. P. Padture, and B. D. Huey, "Anomalous 3d nanoscale photoconduction in hybrid perovskite semiconductors revealed by tomographic atomic force microscopy", en, *Nature Communications*, vol. 11, no. 1, p. 3308, Jul. 3, 2020, number: 1 publisher: Nature Publishing Group, ISSN: 2041-1723. DOI: 10.1038/s41467-020-17012-y.

[123] M. Buckwell, W. H. Ng, S. Hudziak, A. Mehonic, M. Lanza, and A. J. Kenyon, "Improving the consistency of nanoscale etching for atomic force microscopy tomography applications", English, *Frontiers in Materials*, vol. 6, 2019, publisher: Frontiers, ISSN: 2296-8016. DOI: 10.3389/fmats.2019.00203. [Online]. Available: https://www.frontiersin.org/articles/10.3389/fmats.2019.00203/full.

[124] D. Nečas and P. Klapetek, "Gwyddion: An open-source software for spm data analysis", en, *Central European Journal of Physics*, vol. 10, no. 1, pp. 181–188, Nov. 16, 2011, ISSN: 1895-1082, 1644-3608. DOI: 10.2478/s11534-011-0096-2.

[125] K. Lancaster, S. Großer, F. Feldmann, V. Naumann, and C. Hagendorf, "Study of pinhole conductivity at passivated carrier-selected contacts of silicon solar cells", *Energy Procedia*, Proceedings of the 6th International Conference on Crystalline Silicon Photovoltaics (SiliconPV 2016), vol. 92, pp. 116–121, Aug. 1, 2016, ISSN: 1876-6102. DOI: 10.1016/j.egypro.2016.07.040.

[126] A. Morisset, R. Cabal, B. Grange, C. Marchat, J. Alvarez, M.-E. Gueunier-Farret, S. Dubois, and J.-P. Kleider, "Highly passivating and blister-free hole selective poly-silicon based contact for large area crystalline silicon solar cells", en, *Solar Energy Materials and Solar Cells*, vol. 200, p. 109 912, Sep. 2019, ISSN: 09270248. DOI: 10.1016/j.solmat.2019.109912.

[127] M. Ledinský, A. Vetushka, J. Stuchlík, T. Mates, A. Fejfar, J. Kočka, and J. Štěpánek, "Crystallinity of the mixed phase silicon thin films by raman spectroscopy", en, *Journal of Non-Crystalline Solids*, Amorphous and Nanocrystalline Semiconductors, vol. 354, no. 19, pp. 2253–2257, May 1, 2008, ISSN: 0022-3093. DOI: 10.1016/j.jnoncrysol.2007.09.073.

[128] C. Smit, R. A. C. M. M. van Swaaij, H. Donker, A. M. H. N. Petit, W. M. M. Kessels, and M. C. M. van de Sanden, "Determining the material structure of microcrystalline silicon from raman spectra", en, *Journal of Applied Physics*, vol. 94, no. 5, pp. 3582–3588, Sep. 2003, ISSN: 0021-8979, 1089-7550. DOI: 10.1063/1.1596364.

[129] J.-I. Polzin, F. Feldmann, B. Steinhauser, M. Hermle, and S. W. Glunz, "Study on the interfacial oxide in passivating contacts", *AIP Conference Proceedings*, vol. 2147, no. 1, p. 040 016, Aug. 27, 2019, publisher: American Institute of Physics, ISSN: 0094-243X. DOI: 10.1063/1.5123843.

[130] J. W. Slotboom and H. C. de Graaff, "Measurements of bandgap narrowing in si bipolar transistors", en, *Solid-State Electronics*, vol. 19, no. 10, pp. 857–862, Oct. 1, 1976, ISSN: 0038-1101. DOI: 10.1016/0038-1101(76)90043-5.

[131] F.-J. Haug, A. Ingenito, F. Meyer, S. Libraro, N. Bolis, J. J. D. Leon, C. Allebé, and C. Ballif, "Contributions to the contact resistivity in fired tunnel-oxide passivating contacts for crystalline silicon solar cells", *IEEE Journal of Photovoltaics*, vol. 9, no. 6, pp. 1548–1553, Nov. 2019, event: IEEE Journal of Photovoltaics, ISSN: 2156-3403. DOI: 10.1109/JPHOTOV.2019.2939880.

[132] A. S. Kale, W. Nemeth, H. Guthrey, E. Kennedy, A. G. Norman, M. Page, M. Al-Jassim, D. L. Young, S. Agarwal, and P. Stradins, "Understanding the charge transport mechanisms through ultrathin sio $_x$ layers in passivated contacts for high-efficiency silicon solar cells", en, *Applied Physics Letters*, vol. 114, no. 8, p. 083 902, Feb. 25, 2019, ISSN: 0003-6951, 1077-3118. DOI: 10.1063/1.5081832.

[133] H. Guthrey, C. Lima Salles, A. S. Kale, W. Nemeth, M. Page, S. Agarwal, D. L. Young, M. Al-Jassim, and P. Stradins, "Effect of surface texture on pinhole formation in sio $_x$ -based passivated contacts for high-performance silicon solar cells", en, *ACS Applied Materials Interfaces*, vol. 12, no. 50, pp. 55 737–55 745, Dec. 16, 2020, ISSN: 1944-8244, 1944-8252. DOI: 10.1021/acsami.0c12795.

[134] Z. Zhang, Y. Zeng, C.-S. Jiang, Y. Huang, M. Liao, H. Tong, M. Al-Jassim, P. Gao, C. Shou, X. Zhou, B. Yan, and J. Ye, "Carrier transport through the ultrathin silicon-oxide layer in tunnel oxide passivated contact (topcon) c-si solar cells", *Solar Energy Materials and Solar Cells*, vol. 187, pp. 113–122, Dec. 1, 2018, ISSN: 0927-0248. DOI: 10.1016/j.solmat.2018.07.025.

[135] F. Demtchelis, C. F. Pirri, and E. Tresso, "Degree of crystallinity and electrical transport properties of microcrystalline silicon-carbon alloys", *Philosophical Magazine B*, vol. 67, no. 3, pp. 331–346, Mar. 1, 1993, publisher: Taylor Francis $_e$*print : https : //doi.org/*10.1080/13642819308220136, ISSN: 1364-2812. DOI: 10.1080/13642819308220136.

[136] R. Coq Germanicus, P. Leclère, Y. Guhel, B. Boudart, A. D. Touboul, P. Descamps, E. Hug, and P. Eyben, "On the effects of a pressure induced amorphous silicon layer on consecutive spreading resistance microscopy scans of doped silicon", en, *Journal of Applied Physics*, vol. 117, no. 24, p. 244 306, Jun. 28, 2015, ISSN: 0021-8979, 1089-7550. DOI: 10.1063/1.4923052.